

# NOTE TO USERS

This reproduction is the best copy available.

**UMI**<sup>®</sup>



**Non-collocated Control of Vibration of a Three-DOF  
Structure Using the Electromagnetic Vibration  
Absorber**

Yin He

November, 2007

A thesis submitted in partial fulfillment of

the requirements for MScEng degree

in

Control Engineering

Faculty of Engineering

Lakehead University

Thunder Bay, Ontario, Canada



Library and  
Archives Canada

Published Heritage  
Branch

395 Wellington Street  
Ottawa ON K1A 0N4  
Canada

Bibliothèque et  
Archives Canada

Direction du  
Patrimoine de l'édition

395, rue Wellington  
Ottawa ON K1A 0N4  
Canada

*Your file* *Votre référence*  
*ISBN: 978-0-494-42158-1*  
*Our file* *Notre référence*  
*ISBN: 978-0-494-42158-1*

**NOTICE:**

The author has granted a non-exclusive license allowing Library and Archives Canada to reproduce, publish, archive, preserve, conserve, communicate to the public by telecommunication or on the Internet, loan, distribute and sell theses worldwide, for commercial or non-commercial purposes, in microform, paper, electronic and/or any other formats.

The author retains copyright ownership and moral rights in this thesis. Neither the thesis nor substantial extracts from it may be printed or otherwise reproduced without the author's permission.

**AVIS:**

L'auteur a accordé une licence non exclusive permettant à la Bibliothèque et Archives Canada de reproduire, publier, archiver, sauvegarder, conserver, transmettre au public par télécommunication ou par l'Internet, prêter, distribuer et vendre des thèses partout dans le monde, à des fins commerciales ou autres, sur support microforme, papier, électronique et/ou autres formats.

L'auteur conserve la propriété du droit d'auteur et des droits moraux qui protègent cette thèse. Ni la thèse ni des extraits substantiels de celle-ci ne doivent être imprimés ou autrement reproduits sans son autorisation.

---

In compliance with the Canadian Privacy Act some supporting forms may have been removed from this thesis.

While these forms may be included in the document page count, their removal does not represent any loss of content from the thesis.

Conformément à la loi canadienne sur la protection de la vie privée, quelques formulaires secondaires ont été enlevés de cette thèse.

Bien que ces formulaires aient inclus dans la pagination, il n'y aura aucun contenu manquant.

  
**Canada**

## Abstract

Vibration control is very important in many areas including machine operation and daily life. Semi-active vibration control integrates a tuning control scheme with a tunable vibration absorber for suppression of vibration due to a harmonic excitation with a variable excitation frequency.

The electromagnetic vibration absorber (EMVA) is a semi-active vibration device whose stiffness can be tuned on-line. In this study, the EMVA is used for non-collocated vibration control. The study consists of two parts. In the first part, the characterization of the EMVA is revisited using a commercial FE package, Comsol Multiphysics. Various single physics models are built including the electromagnetic coil, the electromagnetic coil with a core, and a permanent magnet (PM) placed between a pair of PMs. These models are used to study the magnetic density in the gap of the electromagnet. A coupling model that involves magnetism and structural mechanics is built. This model is used to study the factors that affect the magnetic stiffness.

In the second part, the EMVA is implemented to suppress vibration of a structure that can be modeled as a three-degree-of-freedom system. The non-collocated control theory is reviewed. The EMVA is modified to allow both manual adjustment and on-line tuning. Three different control methods, FFT-based method, FFT-based plus fine tuning method, and RMS-based method, are developed. The experimental results using the three methods are compared.

## Acknowledgements

I would like to express my sincere gratitude to my supervisor Dr. Kefu Liu for his patient guidance during the course of this study. He has provided me with many encouragements and good ideas. My thesis would not have been possible without his supervision.

I would like to thank my co-supervisor Dr. Dan Zhang.

I wish to thank Mr. K. Bhatia for his assistance in building the experimental apparatus.

I would like to express a note of thanks to all my colleagues at Lakehead University for their helps.

I thank my wife, Min Huang, and my son, Qinchi (Charlie) He, for their exceptional patience and for all the emotional support during the course of this endeavour. My parents have been extremely supportive to my decision of pursuing the study.

# Table of Contents

<b>Certificate of Examination.....</b>	<b>ii</b>
<b>Abstract.....</b>	<b>iii</b>
<b>Acknowledgements.....</b>	<b>iv</b>
<b>Table of Contents.....</b>	<b>v</b>
<b>List of Tables.....</b>	<b>viii</b>
<b>List of Figures.....</b>	<b>ix</b>
<b>Notation.....</b>	<b>xiii</b>
<b>Acronyms.....</b>	<b>xv</b>
<b>Chapter 1</b>	
<b>Introduction.....</b>	<b>1</b>
1.1 An Overview of Vibration Control.....	1
1.2 Review of the Previous Study on Non-collocated Control and the EMVA.....	3
1.3 Objectives of the Thesis Research .....	4
1.4 Outline of the Thesis.....	4
<b>Chapter 2</b>	
<b>Tunable Electromagnetic Vibration Absorber (EMVA).....</b>	<b>5</b>
2.1 The Original Design of the EMVA.....	5
2.2 The Modified EMVA.....	6
2.3 Characterization of the EMVA .....	8
2.4 The Approximate Analytical Method .....	9
2.4.1 Interaction between the Electromagnet and the PM .....	10
2.4.2 Interaction between the Core and the PM.....	17
2.5 Comsol Multiphysics Simulation.....	19
2.5.1 Simulation of the Electromagnetic Coil.....	20
2.5.2 Simulation of the Coil with a Core .....	25
2.5.3 Simulation of the PM.....	27
2.5.4 Determination of the Interacting Force between the Core and the PM ..	29

2.5.5	Determination of the Interacting Force Using a Simplified Model .....	32
2.5.6	Simulation of the Interaction of the PM, the Electromagnet, and the Beam .....	35
2.6	Comparison of the Two Techniques .....	41
 <b>Chapter 3</b>		
<b>Analytic Study on Non-collocated Vibration Control .....</b>		<b>43</b>
3.1	Introduction.....	43
3.2	Vibration Absorber .....	43
3.3	Non-collocated Adaptive-passive Vibration Control of a 3-DOF System.....	45
3.4	Undamped 3-DOF System.....	50
3.5	Frequency Response of the Primary System and the System with the Vibration Absorber .....	52
 <b>Chapter 4</b>		
<b>Experimental Studies.....</b>		<b>58</b>
4.1	Description of the Experimental Setup .....	58
4.2	Identification of the Parameters of the Primary System .....	61
4.3	Vibration Suppression Using Manual Adjustment .....	64
4.4	The EMVA Calibration.....	67
4.5	The EMVA Performance when Attached to the Primary System .....	69
4.6	The EMVA Calibration.....	71
4.7	Experimental Results .....	76
4.7.1	Simulink Model for FFT-based Tuning Method .....	76
4.7.2	Testing Scenario One.....	80
4.7.3	Testing Scenario Two .....	87
 <b>Chapter 5</b>		
<b>Conclusions and Future Work.....</b>		<b>96</b>
5.1	Conclusions.....	96



5.2 Future Work.....	97
<b>Reference .....</b>	<b>98</b>
<b>Appendix A.....</b>	<b>102</b>
<b>Appendix B.....</b>	<b>106</b>
<b>Appendix C.....</b>	<b>110</b>
<b>Appendix D.....</b>	<b>122</b>

## List of Tables

2.1	EMVA system parameters.....	7
2.2	Electromagnetic coil parameters in Comsol.....	20
2.3	Force and displacement.....	31
2.4	Magnetic force and displacement.....	34
3.1	System parameters.....	53
4.1	Initial simplexes vs. the optimal results.....	63

## List of Figures

2.1	The EMVA.....	6
2.2	The modified EMVA .....	7
2.3	Stiffness of the EMVA.....	8
2.4	Simplified electromagnetic coils and core.....	10
2.5	Circular current loop [26] .....	10
2.6	Axial magnetic flux density from the electromagnet, along the centerline of the gap: dash-dot, magnetic flux density from the right cylindrical coils; dot line, magnetic flux density from the left cylindrical coils; solid line, total magnetic flux density [26] .....	12
2.7	Magnetic flux density from the electromagnet, along the centerline of the gap, (a) $I = -0.5$ A, (b) $I = -1.0$ A, (c) $I = -1.5$ A, (d) $I = -2.0$ A. Dot line, experimental; solid line, calculated [26].....	13
2.8	The radial magnetic flux density of the electromagnet when $I = -1.5$ A. ....	14
2.9	The axial magnetic flux density of the electromagnet when $I = -1.5$ A.....	15
2.10	Force and the displacement of the PM with the origin at the gap center: (a) $I = -2.0$ A, (b) $I = -1.5$ A, (c) $I = -1.0$ A, (d) $I = -0.5$ A.....	16
2.11	A PM block .....	17
2.12	Magnetic flux density along the centerline of the PM with the origin located at the center of the pole face. ....	18
2.13	Force between the PM and the core.....	19
2.14	Comsol model for the electromagnet coil.....	21
2.15	Arrow plot of the current density in the electromagnet coil. ....	23
2.16	Arrow plot of the magnetic flux density of the coil.....	23
2.17	The axial magnetic flux density from the electromagnet along the centerline of the gap. (a) $I = -0.5$ A; (b) $I = -1.0$ A; (c) $I = -1.5$ A; (d) $I = -2.0$ A.....	24
2.18	Model of the electromagnetic coil with the core. ....	25
2.19	Arrow plot of the magnetic flux density of the coil with the core.....	26
2.20	The axial magnetic flux density of the electromagnet with the core. The origin is at the gap center. (a) $I = -0.5$ A; (b) $I = -1.0$ A; (c) $I = -1.5$ A; (d) $I = -2.0$ A.....	27
2.21	PM model.....	28
2.22	Arrow plot of the magnetic flux density of the PM.....	28
2.23	Magnetic flux density along the centerline of the PM with the origin located at the center of the pole face. ....	29
2.24	The PM placed in the gap of the core. ....	30
2.25	Force acting on the PM vs. its position.....	31
2.26	A pair of magnetic cylinders.....	32
2.27	Magnetic flux density of the simplified model. The origin is at the gap center. (a) $45 \times 10^3$ A/m ( $I = -0.5$ A); (b) $95 \times 10^3$ A/m ( $I = -1.0$ A); (c) $140 \times 10^3$ A/m ( $I = -1.5$ A); (d) $185 \times 10^3$ A/m ( $I = -2.0$ A). ....	33
2.28	The simplified model with the PM.....	33
2.29	Force acting on the PM vs. its position: (a) $I = -2.0$ A; (b) $I = -1.5$ A; (c) $I = -1.0$ A; (d) $I = -0.5$ A.....	35

2.30	The 2-D coupling model.....	36
2.31	Magnetic flux density of the coupling model: (a) $45 \times 10^3$ A/m ( $I = -0.5$ A); (b) $95 \times 10^3$ A/m ( $I = -1.0$ A); (c) $140 \times 10^3$ A/m ( $I = -1.5$ A); (d) $185 \times 10^3$ A/m ( $I = -2.0$ A).....	38
2.32	Arrow plot of the magnetic density for Case One.....	38
2.33	Force vs. displacement (thick beam): (a) $-185 \times 10^3$ A/m; (b) $-45 \times 10^3$ A/m; (c) $45 \times 10^3$ A/m; (d) $185 \times 10^3$ A/m.....	39
2.34	Force vs. displacement (thin beam): (a) $-185 \times 10^3$ A/m; (b) $-45 \times 10^3$ A/m; (c) $45 \times 10^3$ A/m; (d) $185 \times 10^3$ A/m.....	40
2.35	$\Delta k$ vs. displacement: (a) $-185 \times 10^3$ A/m; (b) $-45 \times 10^3$ A/m; (c) $45 \times 10^3$ A/m; (d) $185 \times 10^3$ A/m.....	41
3.1	A primary system (a) and system with a vibration absorber (b).....	44
3.2	The 3-DOF primary system (a) and the system with a vibration absorber (b).....	46
3.3	(a) $k_a = 0$ ; (b) $k_a = \infty$ .....	51
3.4	Frequency response of the entire system: solid line, $k_a = \infty$ ; dashed line, $k_a = 0$ .....	52
3.5	Frequency response of the primary system.....	54
3.6	Frequency Response and lower bound of the optimum tuning: solid line, Primary system response; lower bound response, when $f_{s1} = f$ (dotted line), $f_{s2} = f$ (dashdot line), and $f_{s3} = f$ (dashed line).....	55
3.7	Optimal stiffness for three natural frequencies of the primary system: dashed line, $ f_1 - f_{s1} $ ; solid line, $ f_2 - f_{s2} $ ; dotted line, $ f_3 - f_{s3} $ .....	56
3.8	$ G_{11}(j\omega) $ of the primary system and of the entire system as $f_{s1} = f_1$ (dotted line), $f_{s1} = f_1$ (dashdot line), and $f_{s1} = f_1$ (dashed line).....	57
4.1	Experiment system.....	58
4.2	Photograph of the experiment model.....	59
4.3	CAD drawing of the entire System.....	60
4.4	FFT spectrum of the response of mass $m_1$ of the primary system to an impact.....	61
4.5	Photograph of the modified EMVA.....	65
4.6	FFT spectrum of an impact response of mass $m_1$ when the EMVA is tuned such that $f_{s2} = f_2$ .....	66
4.7	FFT spectrum of an impact response of mass $m_1$ when the EMVA is tuned such that $f_{s3} = f_3$ .....	66
4.8	Absorber frequency versus the coil current with current loading and current unloading when $f_a$ was preset to be 16.569 Hz manually.....	68
4.9	Absorber frequency versus the coil current with current loading and current unloading when $f_a$ was preset to be 29.256 Hz manually.....	69
4.10	Magnitude of the steady-state acceleration signal versus the excitation frequency when the system is excited by a sinusoidal force and $f_{a2}$ is manually tuned to be $f_{a2} = 16.569$ Hz: dashed line, $I = -2.3$ A; solid line, $I = 0$ ; dotted line, $I = 2.3$ A.....	70

4.11	Magnitude of the steady-state acceleration signal versus the excitation frequency when the system is excited by a sinusoidal force and $f_{a3}$ is manually tuned to be $f_{a2} = 29.256$ Hz: dashed line, $I = -2.3$ A ; solid line, $I = 0$ ; dotted line, $I = 2.3$ A .....	71
4.12	Relationship between the current and the natural frequency of the absorber when $f_a = 16.569$ Hz.....	73
4.13	Relationship between the current and the natural frequency of the absorber when $f_a = 29.256$ Hz.....	73
4.14	The best-fit curve of the second natural frequency of the subsystem and the current of the electromagnet .....	75
4.15	The best-fit curve of the third natural frequency of the subsystem and the current of the electromagnet .....	76
4.16	Simulink model for the FFT-based tuning.....	77
4.17	Simulink model for the FFT-based plus fine tuning method.....	79
4.18	Simulink model for the RMS-based tuning method.....	80
4.19	Experimental results using the FFT-based method when the absorber was manually preset at $f_{a2} = 16.569$ Hz: (a) response of mass $m_1$ without control, (b) response of mass $m_1$ with control, (c) the frequencies: solid line, excitation frequency; dashed line, estimated frequency, (d) the EMVA current. ....	82
4.20	Experimental results using the FFT-based plus fine tuning with a small threshold when the absorber was manually preset at $f_{a2} = 16.569$ Hz: (a) response of mass $m_1$ without control, (b) response of mass $m_1$ with control, (c) the frequencies: solid line, excitation frequency; dashed line, estimated frequency, (d) the EMVA current. ....	83
4.21	Experimental results using the FFT-based plus fine tuning with a proper threshold when the absorber was manually preset at $f_{a2} = 16.569$ Hz: (a) response of mass $m_1$ without control, (b) response of mass $m_1$ with control, (c) the frequencies: solid line, excitation frequency; dashed line, estimated frequency, (d) the EMVA current. ....	84
4.22	Experimental results using the FFT-based plus fine tuning with a larger proper threshold when the absorber was manually preset at $f_{a2} = 16.569$ Hz: (a) response of mass $m_1$ without control, (b) response of mass $m_1$ with control, (c) the frequencies: solid line, excitation frequency; dashed line, estimated frequency, (d) the EMVA current. Proper threshold. ....	86
4.23	Experimental results using the RMS-based method when the absorber was manually preset at $f_{a2} = 16.569$ Hz: (a) response of mass $m_1$ without control, (b) response of mass $m_1$ with control, (c) the excitation frequency, (d) the EMVA current. ....	87
4.24	Experimental results using the FFT-based method when the absorber was manually preset at $f_{a3} = 29.256$ Hz: (a) response of mass $m_1$ without control,	

	(b) response of mass $m_1$ with control, (c) the frequencies: solid line, excitation frequency; dashed line, estimated frequency, (d) the EMVA current. ....	89
4.25	Experimental results using the FFT-based plus fine tuning with a small threshold when the absorber was manually preset at $f_{a3} = 29.256$ Hz: (a) response of mass $m_1$ without control, (b) response of mass $m_1$ with control, (c) the frequencies: solid line, excitation frequency; dashed line, estimated frequency, (d) the EMVA current. ....	90
4.26	Experimental results using the FFT-based plus fine tuning with a proper threshold when the absorber was manually preset at $f_{a3} = 29.256$ Hz: (a) response of mass $m_1$ without control, (b) response of mass $m_1$ with control, (c) the frequencies: solid line, excitation frequency; dashed line, estimated frequency, (d) the EMVA current. ....	92
4.27	Experimental results using the FFT-based plus fine tuning with a large threshold when the absorber was manually preset at $f_{a3} = 29.256$ Hz: (a) response of mass $m_1$ without control, (b) response of mass $m_1$ with control, (c) the frequencies: solid line, excitation frequency; dashed line, estimated frequency, (d) the EMVA current. ....	93
4.28	Experimental results using the RMS-based method when the absorber was manually preset at $f_{a3} = 29.256$ Hz: (a) response of mass $m_1$ without control, (b) response of mass $m_1$ with control, (c) the excitation frequency, (d) the EMVA current. ....	95
A.1	Simple coupling model .....	116

## Notation

Symbol	Description
$m_a$	Absorber mass
$R_1$	Inner radius of the electromagnetic coils
$R_2$	External radius of the electromagnetic coils
$L$	Circumference of the electromagnet
$N$	Turns of the coils
$\delta$	The gap space between two pole faces of the electromagnet
$l$	Length of permanent magnet
$w$	Width of permanent magnet
$h$	Thickness of permanent magnet
$\mu_0$	Permeability of free space
$r_1$	Inner radius of the electromagnetic coils (Comsol model)
$r_2$	External radius of the electromagnetic coils (Comsol model)
$R$	Radius of the torus center line (Comsol model)
$J_0$	External current density (Comsol model)
$r$	Medium radius of the electromagnetic coil (Comsol model)
$S$	Arc length of the opening of the torus (Comsol model)
$I$	Current in the coil
$M$	Magnetization
$\Delta k$	Localized stiffness
$m, m_1, m_2, m_3$	Masses of the primary system
$m_a$	Absorber mass
$k, k_1, k_2, k_3$	Stiffnesses of the primary system
$c, c_1, c_2, c_3$	Damping values of the primary system
$c_a$	Damping value of the vibration absorber
$f(t)$	External force
$F_0$	Magnitude of the external force
$\omega$	Excitation frequency

Symbol	Description
$x, x_1, x_2, x_3$	Positions of the masses of the primary system
$x_a$	Positions of the absorber mass
$\dot{x}, \dot{x}_1, \dot{x}_2, \dot{x}_3$	Velocities of the primary system masses
$\dot{x}_a$	Velocity of the absorber mass
$\ddot{x}, \ddot{x}_1, \ddot{x}_2, \ddot{x}_3$	Accelerations of the primary system masses
$\ddot{x}_a$	Acceleration of the absorber mass
$X, X_1, X_2, X_3$	Steady-state response
$X_a$	Steady-state response of the absorber mass
$F(s)$	Force magnitude vector
$G_{11}(s)$	Transfer function between $F(s)$ and $X_1(s)$
$D(s)$	Determinant of determinant of $A$ , or the characteristic equation (CE) of the system
$N_1(s)$	Determinant of the subsystem
$f_i (i = 1, 2, 3)$	Natural frequencies of the primary system
$f_{si} (i = 1, 2, 3)$	Natural frequencies of the subsystem
$f$	Natural frequency of the absorber
$K$	Stiffness matrix
$M$	Mass matrix
$J(k_1, k_2, k_3)$	Cost (Objective) function



## Acronyms

MR	Magneto-Rheological
ER	Electro-Rheological
EMVA	Electromagnetic Vibration Absorber
PM	Permanent Magnet
DOF	Degree Of Freedom
SISO	Single-Input-Single-Output
DAQ	Date Acquisition
FFT	Fast Fourier Transform
RMS (rms)	Root-Mean-Squares
DAC	Digital to Analog Channel
ADC	Analog to Digital Channel
ALE	Arbitrary Lagrangian-Eulerian

# Chapter 1

## Introduction

Vibration is periodic or non-periodic motion. Occasionally vibration is desirable, such as musical instruments or hydraulic hammers. But more often, vibration is undesirable. It wastes energy and creates unwanted sound. The vibrations of engines, instruments, buildings, or any mechanical devices in operation are usually unwanted. For example, electronic components used in airplanes, automobiles, machines, and so on may fail because of vibration, shock, and/or sustained vibration input. If the vibration does not affect the proper operation of a machine, it can be neglected. But as the vibration becomes severe to damage the system, vibration suppression is necessary. In order to suppress the vibration, various methods are used. In the following section, these issues are identified through an overview of structural vibration control.

### 1.1 An Overview of Vibration Control

In general vibration suppression can be achieved by design, isolation, or control. In the design stage, all attempts are made to minimize the possibility of inducing vibration. For example, if a system experiences resonance, changing the natural frequency of the system can fix the problem. If vibration is caused by a centrifugal force due to an imbalance mass, eliminating the imbalance mass can solve the problem. But this is not an easy work. Practically before a system is made, knowing the natural frequency and the imbalance mass without testing is not possible.

The second way to deal with vibration is to isolate the source of vibration from the system of interest or to isolate the system from the source of vibration. This can be done by using highly damped materials as dampers to change the stiffness and damping between the source of vibration and the device that is to be protected from the vibrations. Changing the damping of a damper decreases the amplitude of the vibration [1], but at the same time the achievable attenuation is reduced [2]. The function of the damper actually dissipates vibration energy over a range of frequencies [3]-[4]. By changing the damper

to an optimal value, the damper is used to decrease the vibration. In [5], a bridge-friendly control strategy is developed to reduce the vibration of a bridge through changing the damping value of the vehicle. In [6], electro-rheological (ER) and magneto-rheological (MR) materials are also used as variable dampers.

The methods of vibration control can be classified as passive, active, and hybrid. The passive control involves the use of reactive or resistive devices that either load the transmission path of the disturbing vibration or absorb vibratory energy. Invented in 1909 by Den Hartog, vibration absorbers are a passive vibration control device which has been widely used in machinery, aviation, construction, structures [6]-[8] and sound radiation reduction [9]. For example, vibration absorbers with viscous damping have been used on Taipei Financial Center [10], and the London Millennium Footbridge [11]. Active control also loads the transmission path but achieves this loading through the use of actuators that generally require external energy, such as piezoelectric actuators to reduce the vibration of a thin circular aluminum plate [12]. Hybrid control integrates a passive approach with an active control approach. The hybrid control is intended to reduce the amount of external power necessary to achieve control. The hybrid approach is also referred to as adaptive-passive control, or semi-active control. The semi-active control systems are widely used in the field of vibration control, since they combine the advantages of both passive and active control systems. On one hand, they keep the reliability of the passive systems even in the event of power loss; on the other hand, they maintain the versatility and adaptability of active systems without a great amount of power consumption.

Generally, the mechanical properties of the semi-active systems, such as the stiffness and/or the damping value, can be tuned based on the feedback from the measured response and /or the excitation. Firstly, damping value adjusting methods are described. In [13], by increasing the voltage source on the piezoelectric material, the damping value of a beam is enhanced to control the vibration of the beam. In [14]-[15], a variable stiffness absorber was developed by varying the length of a cantilever beam. In [16], a semi-active hydropneumatic spring and damper system with variable damping coefficient and stiffness was designed. The stiffness is varied by changing gas volumes and the damping value is varied by controlling the fluid passing through a valve (semi-active damper). A resetting semi-active stiffness damper was developed by releasing the

vibration energy in appropriate time instant through switching a valve open and close in this damping system [17]. In [18], by changing the electric field to ER, the damping value was changed such that ER dampers were used for truss vibration suppression. In [19]-[20], typical MR dampers were studied. Damping value is controlled by electromagnet. In [21]-[22], semi-active friction dampers were studied. Secondly, stiffness adjusting is reviewed. In [22], a plane rhombus spring assembly with a single absorber mass was developed. The stiffness of the spring assembly is adjusted as the shape of the rhombus is changed by applying an electromechanical actuator. In [23]-[24], the stiffness of the absorber is adjusted by changing the number of active spring coils used to perform control. This same absorber was used in collocated and non-collocated control, respectively. In [25]-[26], an electromagnetic vibration absorber (EMVA) was developed for vibration suppression.

## **1.2 Review of the Previous Study on Non-collocated Control and the EMVA**

In many applications of vibration control, the sensor (at the point of interest for control) is collocated with the vibration control actuator. It is called the collocated control. For some applications it is not possible to collocate the vibration control actuator at the location of interest, and the control becomes non-collocated. Non-collocated control is more complicated than collocated control [20]. Most previous researches on the non-collocated vibration were active control. In [27], an  $H_\infty$  controlled was used to reduce the effects of solar array vibrations on telescope pointing jitter for the Hubble Space Telescope. In [28], a controller designed with the structured singular value approach was applied for a large space structure which has closely spaced, lightly damped modes. In [29], a time delay in the feedback loop to compensate for the phase difference between the actuator and sensor was introduced. This time delay reduces the non-collocated vibration control problem to the collocated case. In [30], a neural network based on forward dynamics and decentralized control was used to attenuate vibrations. In [31], an  $H_\infty$  controller was developed to manipulate an active actuator in suppressing the

vibration of a truss structure. In [24], adaptive-passive approach for solving the non-collocated vibration control problem was studied.

In [25]-[26], an EMVA, which has advantages of rapid reaction and motionless adjustment, was applied on a one degree of freedom (1-DOF) system. It is a collocated control. By varying the current to the electromagnet, the absorber stiffness can be on-line adjusted such that it can suppress a system excited by a harmonic force with a variable frequency.

### **1.3 Objectives of the Thesis Research**

The main objective of the thesis is to apply the EMVA to the non-collocated control. The study aims to:

1. modify the EMVA such that it is suitable for the non-collocated control;
2. characterize the EMVA using a Comsol Multiphysics simulation;
3. develop and test the control strategies.

### **1.4 Outline of the Thesis**

Chapter 2 characterizes the EMVA through an analytic computation and Comsol Multiphysics simulation. The chapter describes the results obtained by the analytic computation method and compares them with those from Comsol Multiphysics simulation. Chapter 3 presents the theory of the non-collocated control. In this chapter, the model is analyzed and tuning law is established. Chapter 4 applies the modified EMVA to the non-collocated control of vibration of a 3-DOF structure. Three control methods are tested. Chapter 5 presents the conclusions and suggests the future work.

## **Chapter 2**

### **Tunable Electromagnetic Vibration Absorber (EMVA)**

In order to apply the EMVA in vibration control, it is necessary to understand its characteristics. In this chapter, a commercial package Comsol Multiphysics is used to characterize the EMVA. The intention is to compare the results from Comsol with those from the approximate analytical method developed in [25].

#### **2.1 The Original Design of the EMVA**

Tunable electromagnetic vibration absorber (EMVA) is a semi-active vibration absorber. A CAD drawing of the EMVA developed in [25] is shown in Figure 2.1. It consists of a clamped-clamped beam, a permanent magnet (PM) that is embedded in the middle of the beam, and an electromagnet. The PM-beam assembly is placed between the poles of the electromagnet. The PM plays a dual role: acting as an absorber mass and forming a variable spring by interacting with the electromagnet through varying the direct current (DC) of the electromagnet.

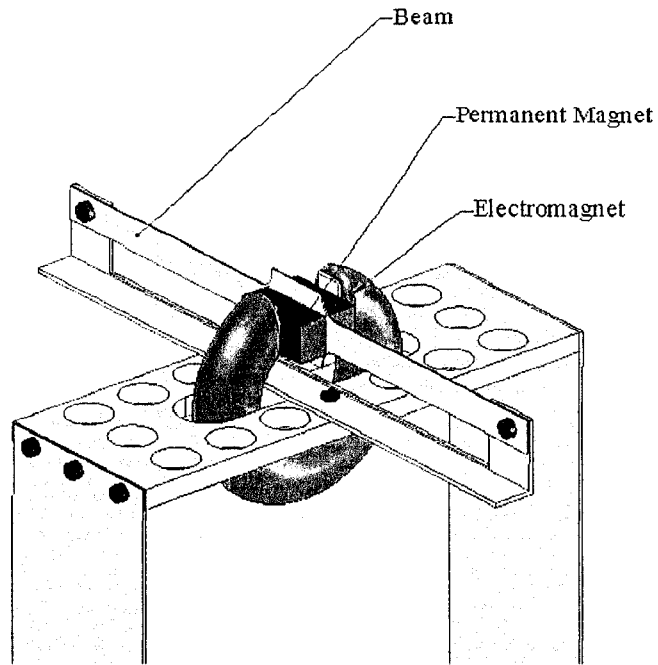


Figure 2.1 The EMVA

## 2.2 The Modified EMVA

As shown in Chapter 3, non-collocated control demands the EMVA to have a large adjustment. To meet this requirement, the EMVA was modified. Figure 2.2 shows the modified EMVA. The major change was made to the way of supporting the absorber beam by adding two movable beam holders and two tensioners. Through changing the positions of the beam holders the beam length can be varied. By adjusting the tensioners, the beam tension can be varied. Both ways alter the absorber stiffness. Table 2.1 shows the parameters of the EMVA. It should be noted that a majority of these parameters have the same values as in [25]-[26] exception of  $m_a$ ,  $\delta$  and  $h$ .

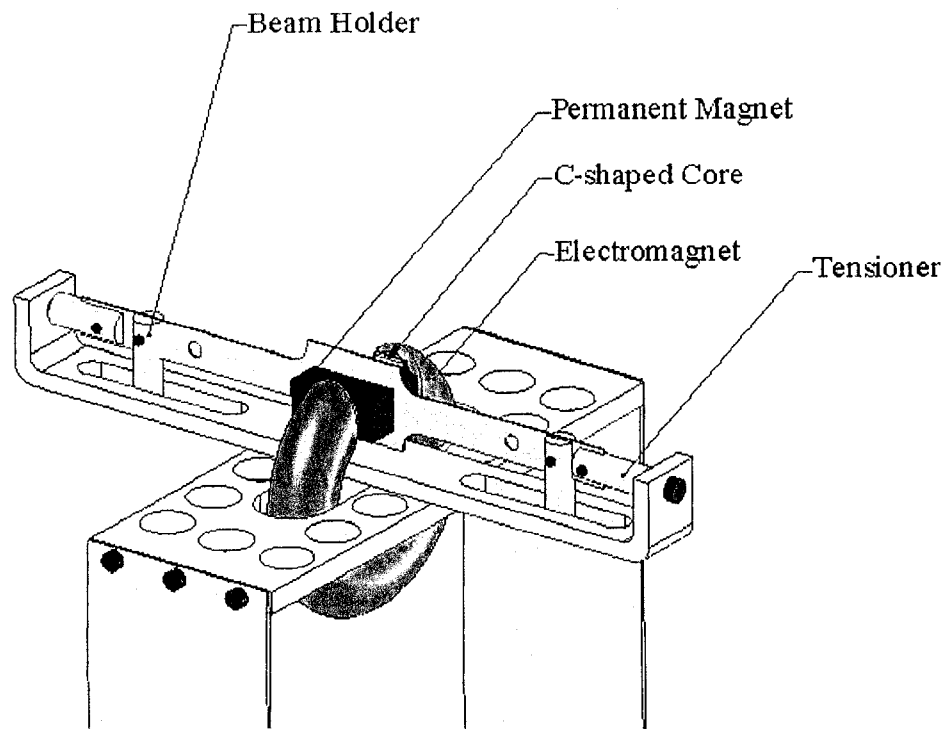


Figure 2.2 The modified EMVA

Table 2.1 EMVA system parameters

Symbol	Description	Quantity, Unit
$m_a$	Absorber mass	0.2515 kg
$R_1$	Inner radius of the electromagnetic coils	11.0 mm
$R_2$	External radius of the electromagnetic coils	20.0 mm
$L$	Circumference of the electromagnet	314.16 mm
$N$	Number of the coils	784
$\delta$	The gap between two pole faces of the electromagnet	43.0 mm
$l$	Length of PM	48.0 mm
$w$	Width of PM	22.0 mm
$h$	Thickness of PM	38.0 mm
$\mu_0$	Permeability of free space	$4\pi \times 10^{-7}$ H/m



### 2.3 Characterization of the EMVA

As shown in Figure 2.3, the stiffness of the EMVA is composed of three parts: constant spring  $k_{c1}$  created by the absorber beam, constant spring  $k_{c2}$  formed by the interaction between the PM and the core of the electromagnet, and variable spring  $k_v$  generated by the interaction between the PM and the electromagnet. The value  $k_{c1}$  is adjusted by the tension and length of the beam; the value  $k_{c2}$  is determined by the gap between the PM and the core of the electromagnet, and the value  $k_v$  varies with the current of the electromagnet.

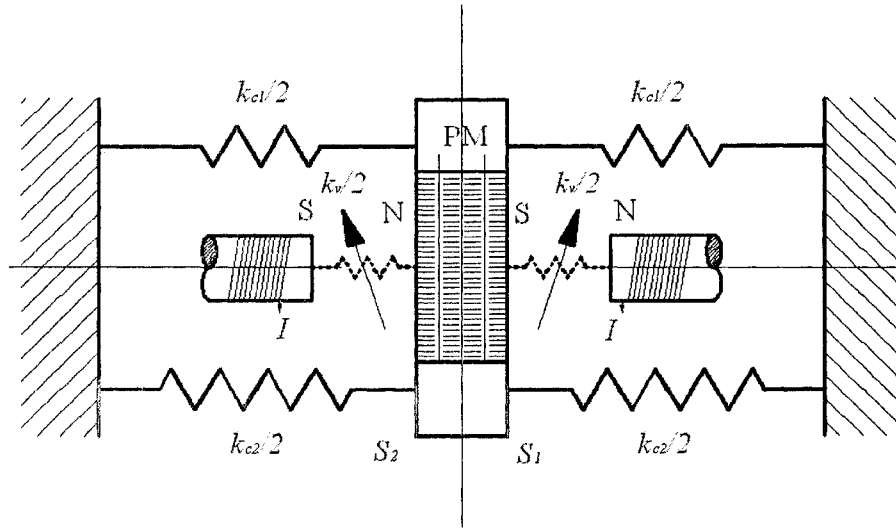


Figure 2.3 Stiffness of the EMVA

The total stiffness  $k_a$  of the absorber is the sum of these three parts

$$k_a = k_{c1} + k_{c2} + k_v \quad (1.1)$$

When the absorber mass  $m_a$  has a small displacement from its equilibrium position, the restoring force applied on mass  $m_a$  by the beam is proportional to this displacement. The larger the displacement is, the larger the force dragging the absorber mass  $m_a$  back to the equilibrium position. Therefore  $k_{c1}$  is considered linear over the range of the beam's displacement. As the displacement occurs, one pole of the PM is closer to one pole of the

electromagnet, the force attracting the PM away from the equilibrium position increases. As the result,  $k_{c2}$  is negative. The variable stiffness  $k_v$  varies from negative to positive as the current changes over its full range. To make sure that  $k_a$  is positive, it must be met that  $k_{c1} > |k_{c2}| + |k_{vmax}|$ . If this condition does not hold, the function of the absorber will be lost.

In [25]-[26], an approximate analytical method was used to characterize the EMVA. In the present study, the commercial package, Comsol Multiphysics, is used to conduct the characterization analysis. The results are compared with those from [25]-[26]. Comsol Multiphysics is a software package based on the finite element methods for the simulation of any physical process described by partial differential equations. It features the state-of-the-art solvers that can deal with complex problems, while its intuitive user interface is designed to provide ease of use and flexibility.

## 2.4 The Approximate Analytical Method

This section presents the results obtained by using the approximate analytical method developed in [25] and [26]. Owing to the fact that a majority of parameters have the same values as in [25]-[26], the certain results (see Figures 2.6, 2.7 and 2.9) remain the same as in [25]-[26]. The force acting on the PM caused by the electromagnet depends on the magnetic flux density of the electromagnet, the magnetic flux density of the PM, and the permeability of the electromagnetic core. To determine the magnetic stiffness between the electromagnet and the PM, the magnetic flux density of the electromagnet needs to be first evaluated. Due to the complicated shape of the EMVA, the following strategy was employed. The electromagnet, composed of coils which are wound around the C-shaped core, see Figure 2.2, is of a torus shape. Simplification is made by cutting the torus into two halves, straightening each of them to a hollow cylinder with an inner radius  $R_1$  and an outer radius  $R_2$ , and a length  $L/2$ , where  $R_1$ ,  $R_2$ , and  $L$  are the inner radius, the outer radius of the torus, and the perimeter of the center line of the torus, respectively, as shown in Figure 2.4.

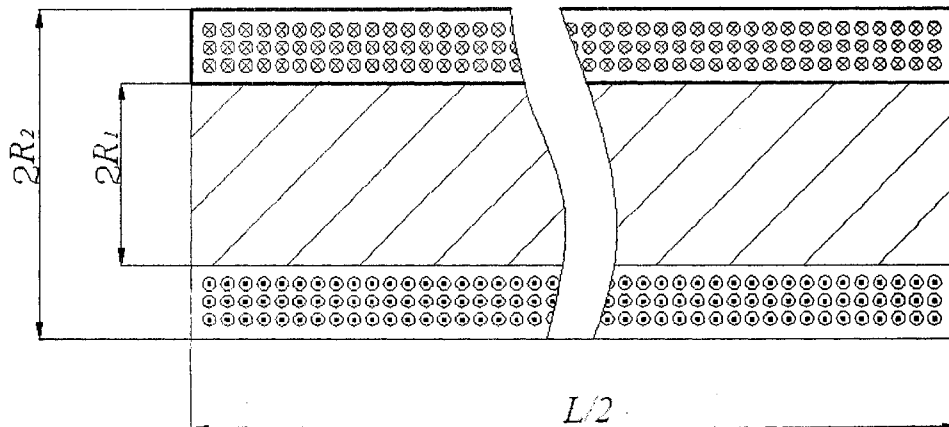


Figure 2.4 Simplified electromagnetic coils and core

### 2.4.1 Interaction between the Electromagnet and the PM

The flux density of such a hollow cylinder can be found by examining first the magnetic field from a circular current loop with a radius  $a$ , shown in Figure 2.5. Expanding on the Bio-Salvart law, which determines the magnetic field contribution of a current carrying element, the flux density  $B_r$  in the radial direction  $r$  and the flux density  $B_z$  in the axial direction  $z$  can be expressed as [32].

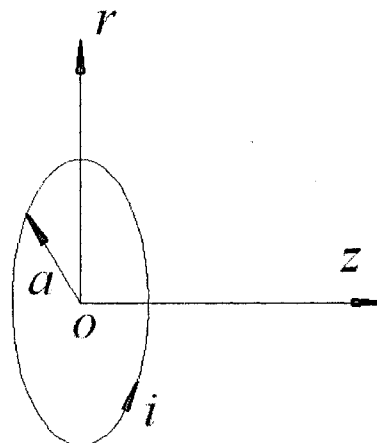


Figure 2.5 Circular current loop [26]

$$B_{lr} = \frac{\mu_0 i z}{2\pi r [(a+r)^2 + z^2]^{1/2}} \left[ E_2 \frac{a^2 + r^2 + z^2}{(a-r)^2 + z^2} - E_1 \right] \quad (1.2)$$

$$B_{lz} = \frac{\mu_0 i}{2\pi [(a+r)^2 + z^2]^{1/2}} \left[ E_2 \frac{a^2 + r^2 + z^2}{(a-r)^2 + z^2} + E_1 \right] \quad (1.3)$$

where  $E_1$  and  $E_2$  are the complete elliptic integrals of the first and second kind, respectively. They are of the forms:

$$E_1 = \int_0^{\pi/2} \left[ 1 - \frac{4ar}{[(a+r)^2 + z^2]} \sin^2 \theta \right]^{-1/2} d\theta \quad (1.4)$$

$$E_2 = \int_0^{\pi/2} \left[ 1 - \frac{4ar}{[(a+r)^2 + z^2]} \sin^2 \theta \right]^{1/2} d\theta \quad (1.5)$$

Using Equations (1.2) and (1.3) the magnetic flux density from a single current loop can be found. The total magnetic flux density of half of the whole torus can then be obtained by superposing contributions of individual coils. By integrating Equations (1.2) and (1.3) in both the radial and axial directions, the total contribution of the magnetic flux densities of the cylinder is found:

$$B_{sr} = \int_{R_1}^{R_2} \int_{0/2}^{L/2} B_r(a, r, z + \lambda) dz da \quad (2.6)$$

$$B_{sz} = \int_{R_1}^{R_2} \int_{0/2}^{L/2} B_z(a, r, z + \lambda) dz da \quad (2.7)$$

where  $B_{sr}$  and  $B_{sz}$  are the radial and axial magnetic flux density from one of the current carrying cylinders, respectively, with the origin located at the center of the end face. Note that in the equations above, the loop current should be substituted by

$$i = \frac{N I}{(R_1 - R_2)L} \quad (2.8)$$

where  $I$  is the coil current, and  $N$  is the number of the coils. The total magnetic flux densities  $B_r$  and  $B_z$  from the two poles of the current carrying coils are found by summing the densities from the right and the left cylinders. Figure 2.6 illustrates the axial magnetic flux density along the centerline of air gap, from the two poles of the electromagnet respectively when the current is  $I = -1.0$  A. The total flux density  $B_z$  is obtained by adding these two components point to point.

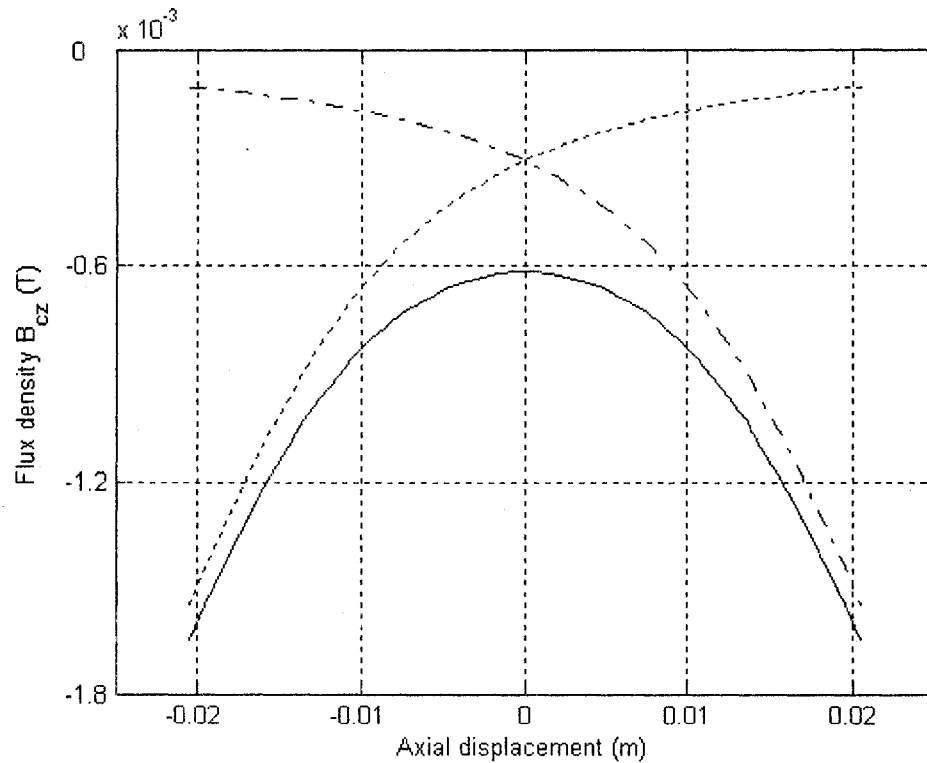


Figure 2.6 Axial magnetic flux density from the electromagnet, along the centerline of the gap: dash-dot, magnetic flux density from the right cylindrical coils; dot line, magnetic flux density from the left cylindrical coils; solid line, total magnetic flux density [26]

When the core is taken into consideration, the magnetic field between the gap space of two pole faces of the electromagnet is enhanced greatly. The effect is included by introducing an amplification number  $\mu_r$ , which is the relative permeability of the steel core. Further, for a certain coil, the flux available in the air gap is solely affected by the

term  $\mu_r/\gamma$  where the denominator  $\gamma$  is called the leakage factor, defined as the ratio of the total flux to the gap flux. Due to many factors, such as structure, materials, the term  $\mu_r/\gamma$  is often determined by experiment. In [25]-[26], a DC magnetometer (AlphaLab, Model: DCM) was used to measure the axial magnetic flux density at the points along the centerline of the gap of the electromagnet as it was loaded with four different amplitudes of DC current. The value  $\mu_r/\gamma$  was determined in the following way: a modified computed axial flux density was found by multiplying a trial value  $\mu_r/\gamma$  to the computed  $B_{cz}$ ; then the squared error between the measured axial flux density and the modified computed axial flux density was found; by varying the values of  $\mu_r/\gamma$  the squared error was minimized. It was found that the value of  $\mu_r/\gamma = 27.5$  results in the least discrepancy, more specifically, accuracy is at 94% within the displacement of  $[-0.015, 0.015]$ , where the origin is located at the center of the air gap. Figure 2.7 shows the magnetic flux density of the electromagnet with the core.

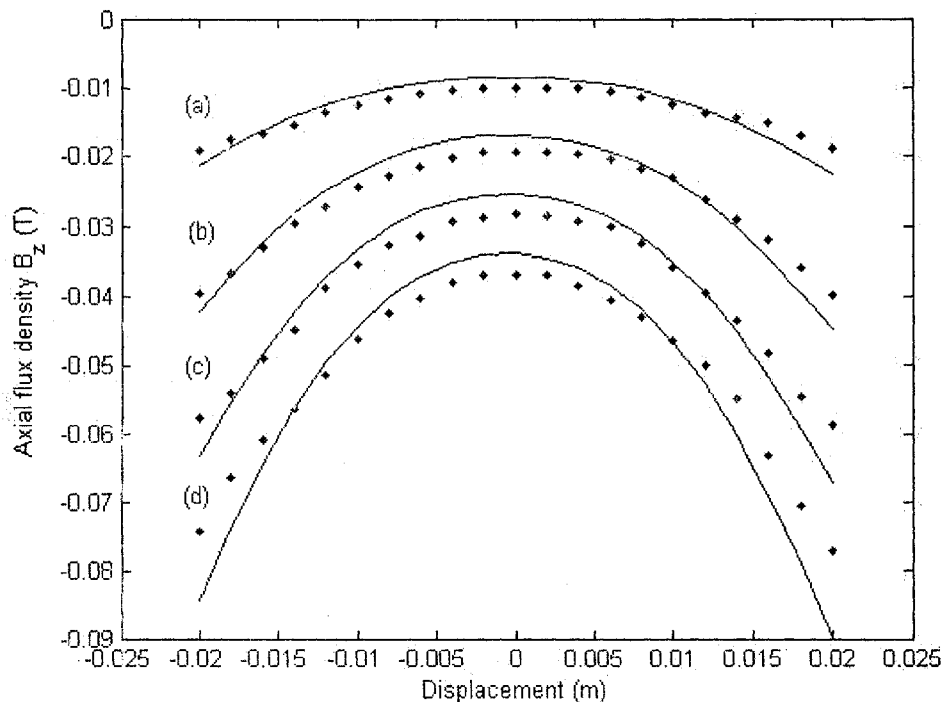


Figure 2.7 Magnetic flux density from the electromagnet, along the centerline of the gap, (a)  $I = -0.5$  A, (b)  $I = -1.0$  A, (c)  $I = -1.5$  A, (d)  $I = -2.0$  A. Dot line, experimental; solid line, calculated [26].

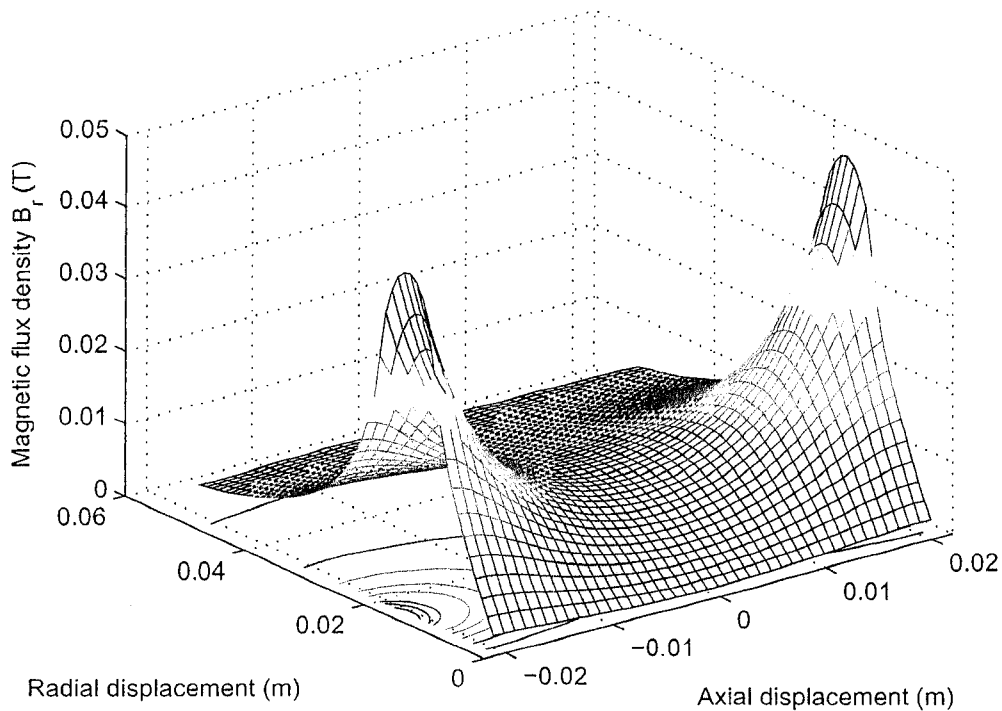


Figure 2.8 The radial magnetic flux density of the electromagnet when  $I = -1.5$  A.

Using the above described method, the radial and axial components of the magnetic field in the pole gap can be found. Figures 2.8 and 2.9 show the values when the electromagnet carries a current of  $I = -1.5$  A. From Figure 2.8, it can be seen that the peaks of the radial flux density  $B_r$  occur on the pole faces at a distance of 15 mm from the centerline of the axis of the cylinders, i.e., the mean radius of the coils; and it diminishes to zero along the centerline of the coils. By contrast, in terms of absolute value, the axial flux density  $B_z$  peaks along the centerline of the coils, reaching maximum on the pole faces and minimum in the middle of the air gap.

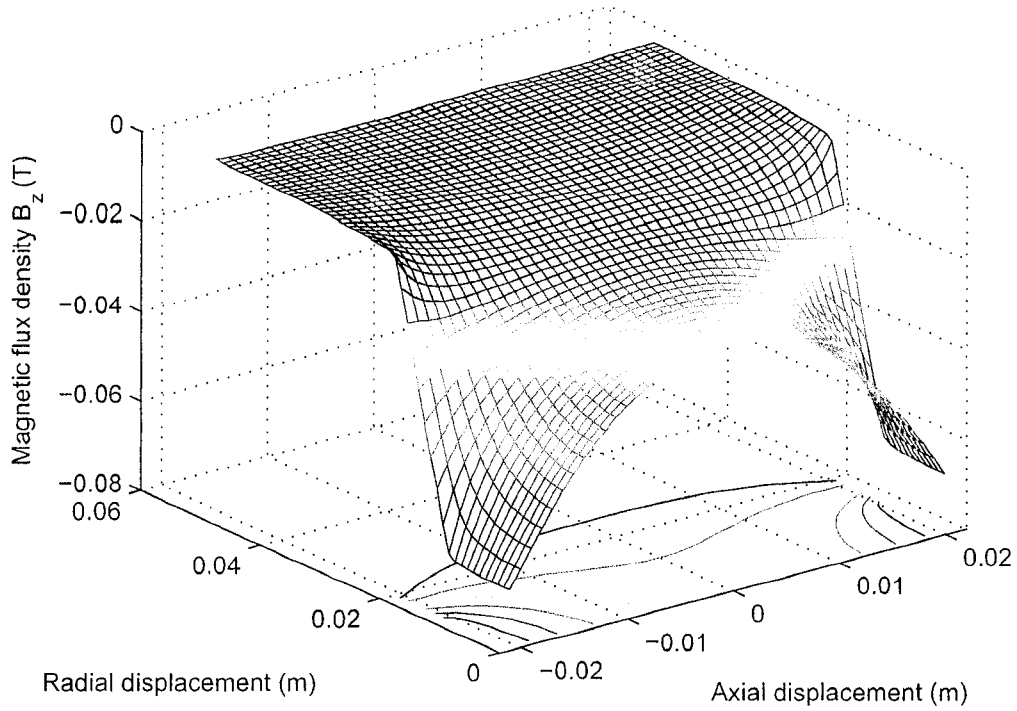


Figure 2.9 The axial magnetic flux density of the electromagnet when  $I = -1.5$  A.

With the flux density of the electromagnet available, the interaction force between the electromagnet and the PM is given by

$$F_z = -\partial W / \partial z \quad (2.9)$$

where  $W$  is the energy of interaction of the electromagnet and the PM. The energy  $W$  may be calculated as the integral of the pole density on pole surfaces  $S_1$  and  $S_2$  (refer to Figure 2.3) of the PM times the potential from the electromagnet. If  $\phi_1^{em}$  is the potential from the electromagnet at the pole face  $S_1$  and  $\phi_2^{em}$  that at the pole face  $S_2$ , then

$$W = \mu_0 \int_{S_1} M \phi_1^{em} dS + \mu_0 \int_{S_2} (-M) \phi_2^{em} dS \quad (2.10)$$

or



$$F_z = -\mu_0 \int_{S_1} M \frac{\partial \varphi_1^{em}}{\partial z} dS + \mu_0 \int_{S_2} M \frac{\partial \varphi_2^{em}}{\partial z} dS = M \left( \int_{S_1} B_{z1} dS - \int_{S_2} B_{z2} dS \right) \quad (2.11)$$

where  $B_{zi} = -\mu_0 \frac{\partial \varphi_i^{em}}{\partial z}$ ,  $i=1,2$ , is the electromagnetic flux density on the pole faces  $S_1$  and  $S_2$  of the PM, respectively.  $M$  is the magnetization of the PM. Equation (2.11) indicates that the force  $F_z$  is proportional to the difference between the total flux over the pole faces  $S_1$  and  $S_2$ . It should be noted that, due to the symmetry of distributions of the radial flux, no net interaction force exists in the radial direction. Figure 2.10 shows the plots of the electromagnetic force  $F_z$  versus the displacement of the PM for four different amplitudes of the coil currents. The slopes of force-displacement curves present the electromagnetic stiffness  $k_v$ .

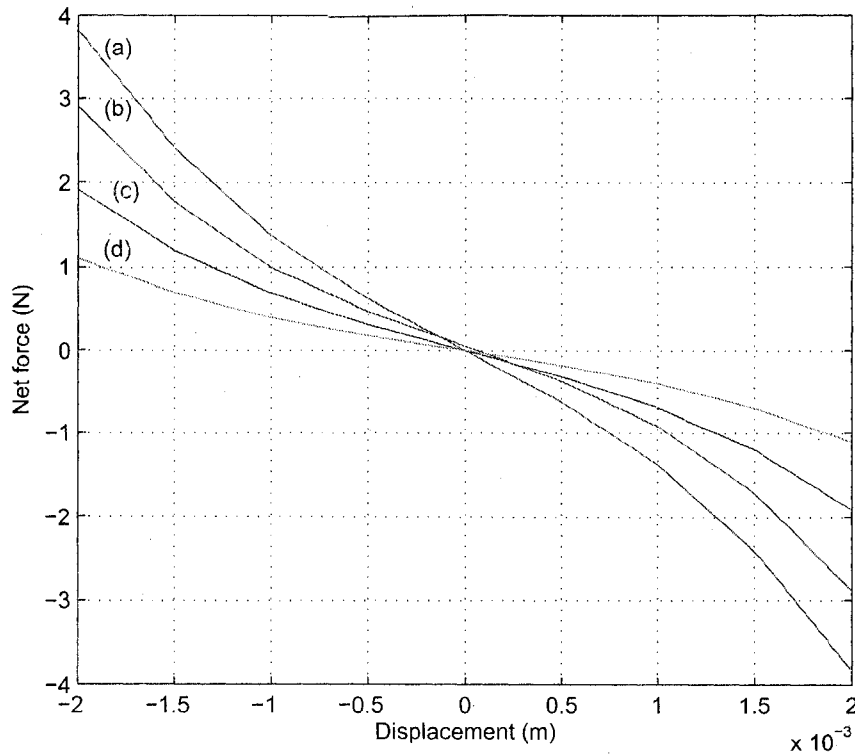


Figure 2.10 Force and the displacement of the PM with the origin at the gap center: (a)  $I = -2.0$  A, (b)  $I = -1.5$  A, (c)  $I = -1.0$  A, (d)  $I = -0.5$  A.

## 2.4.2 Interaction between the Core and the PM

The interaction between the PM and the core forms  $k_{c2}$ . The orthorhombic PM can be represented by two rectangles of surface pole density  $\sigma = \pm M$ , where  $M$  is the magnet strength or magnetization of the PM. Figure 2.11 shows an orthorhombic PM. The magnetic flux density on the central axis at a distance  $z$  from the PM can be calculated as [26]

$$B_{pm} = \frac{\mu_0 \sigma}{\pi} \left[ \sin^{-1} \frac{lw}{\sqrt{(l^2 + 4z^2)(w^2 + 4z^2)}} - \sin^{-1} \frac{lw}{\sqrt{[l^2 + 4(z+h)^2][w^2 + 4(z+h)^2]}} \right] \quad (2.12)$$

Figure 2.12 shows the magnetic flux density along the Z-axis, obtained by using Equation (2.12) with  $M = 395.8 \times 10^3$  A/m [25]-[26].

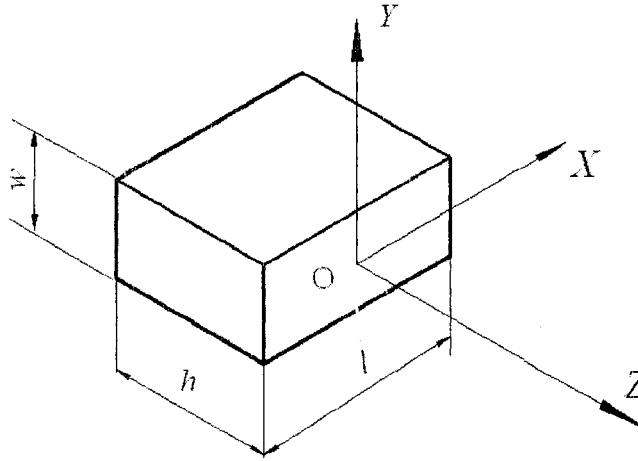


Figure 2.11 A PM block

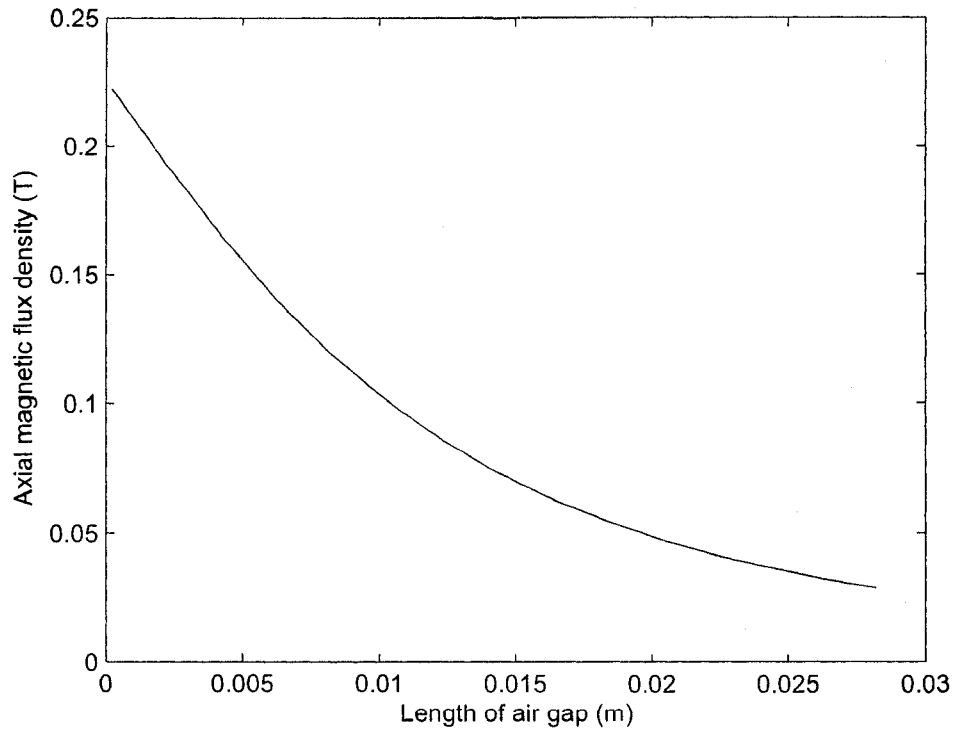


Figure 2.12 Magnetic flux density along the centerline of the PM with the origin located at the center of the pole face.

The force between the PM and the core of the electromagnet is expressed as

$$F = \alpha B_s^2 A \quad (2.13)$$

where  $\alpha$  is a constant to be determined,  $A$  is the area of the PM surface, and  $B_s$  is the flux density produced by the PM at the surface of the coil. Let  $F_1$  be the interaction force between the right end of the core and the PM and  $F_2$  that between the left end of the core and the PM (see Figure 2.3). When the PM is located in the exact middle of the air gap of the core,  $F_1 = -F_2$  such that the net force is zero. When the PM is moved to right,  $|F_1| > |F_2|$ , and vice versa. Using Equation (2.13) the net force acting on the PM is given by

$$F = F_1 - F_2 = \alpha A(B_{s1}^2 - B_{s2}^2) \quad (2.14)$$

where  $B_{s1}$  and  $B_{s2}$  are the flux densities at the right and left end of the core, respectively. Figure 2.13 shows the plot of the interaction force  $F$  as a function of displacement of the PM. Therefore, stiffness  $k_{c2}$  can be approximated as a constant value of -1236 N/m.

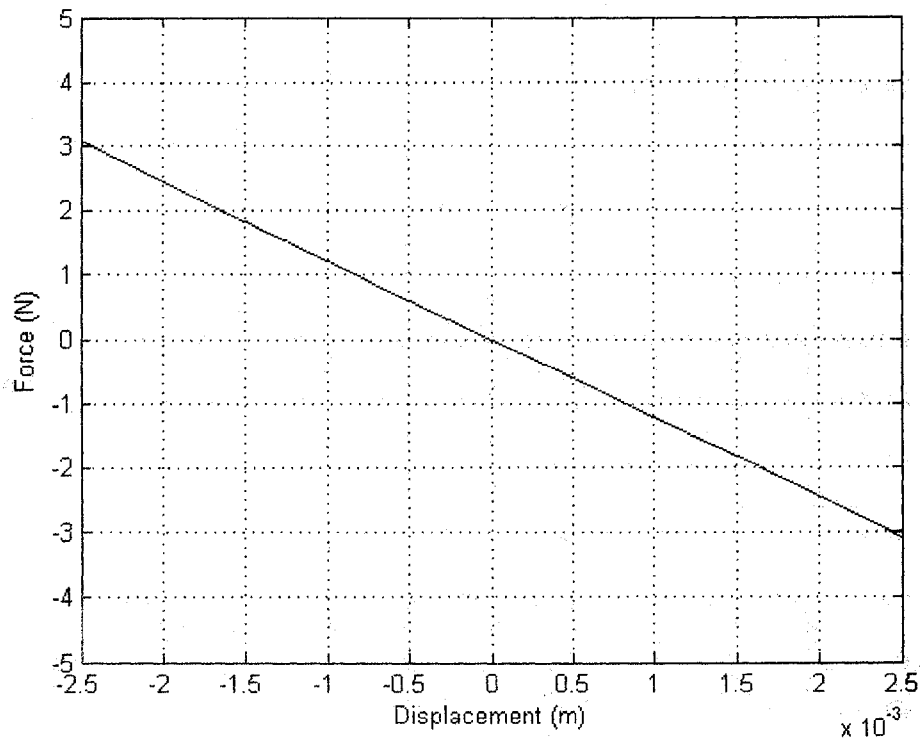


Figure 2.13 Force between the PM and the core.

## 2.5 Comsol Multiphysics Simulation

To model the EMVA accurately using an analytical method is an extremely complicated task. On the other hand, Comsol Multiphysics offers a possibility of solving the problem numerically. In this study, both the single physics and multiphysics functionalities of Comsol are explored for the purpose of the EMVA characterization.

## 2.5.1 Simulation of the Electromagnetic Coil

First the electromagnetic coil without a core is simulated. Attempt was made to model the coil using a series of the current loops. However, such a model demands a large memory and computational time. Thus the coil was simplified as a thin-shell hollow torus. Figure 2.14 shows a Comsol model for the electromagnetic coil. The model is built in AC/DC Module > Statics > Magnetostatics mode. The model meshing information is as follows. Number of degrees of freedom is 58131. Number of mesh points is 1356. Number of elements is 7395. Number of boundary elements is 1946. The torus carries a constant current flowing through it along the direction as shown in Figure 2.15. The parameters of the hollow torus are given in Table 2.2. It is noted that all the parameters are the same as those given in Table 2.1 except  $r_1$  and  $r_2$ . As the thin-shell hollow torus is used to simulate the electromagnetic coils, its inner and external radii are selected between the range of those of the electromagnetic coils.

Table 2.2 Electromagnetic coil parameters in Comsol

Symbol	Description	Quantity, Unit
$r_1$	Inner radius of the electromagnetic coils	12.0 mm
$r_2$	External radius of the electromagnetic coils	15.0 mm
$R$	Radius of the torus center line	50.0 mm
$J_0$	External current density	Equation (2.15), A/m <sup>2</sup>
$N$	Number of the coils	784
$r$	Medium radius of the electromagnetic coil	$(r_1 + r_2)/2$
$S$	Arc length of the opening of the torus	0.04445 mm
$I$	Current in the coil	0.5, 1.0, 1.5, 2.0 (A)

A current flows in the circular direction on the transverse cross section of the hollow tube. In the Comsol model, the current density needs to be specified. The current density that flows in the cross section of the torus is obtained by

$$J_0 = \frac{IN}{(2\pi R - S)(r_2 - r_1)} \quad (2.15)$$

where  $IN$  is the total current and  $(2\pi R - S)(r_2 - r_1)$  is the area in which the current flows through. In Comsol Multiphysics, the  $x$ ,  $y$  and  $z$  components of the current density need to be defined. They are given as the follows:

$$I_x = -\frac{J_0 xy}{r\sqrt{x^2 + z^2}}, \quad I_y = \frac{J_0(\sqrt{x^2 + z^2} - R)}{r}, \quad I_z = -\frac{J_0 zy}{r\sqrt{x^2 + z^2}}$$

The resultant of the three values represents the current density.

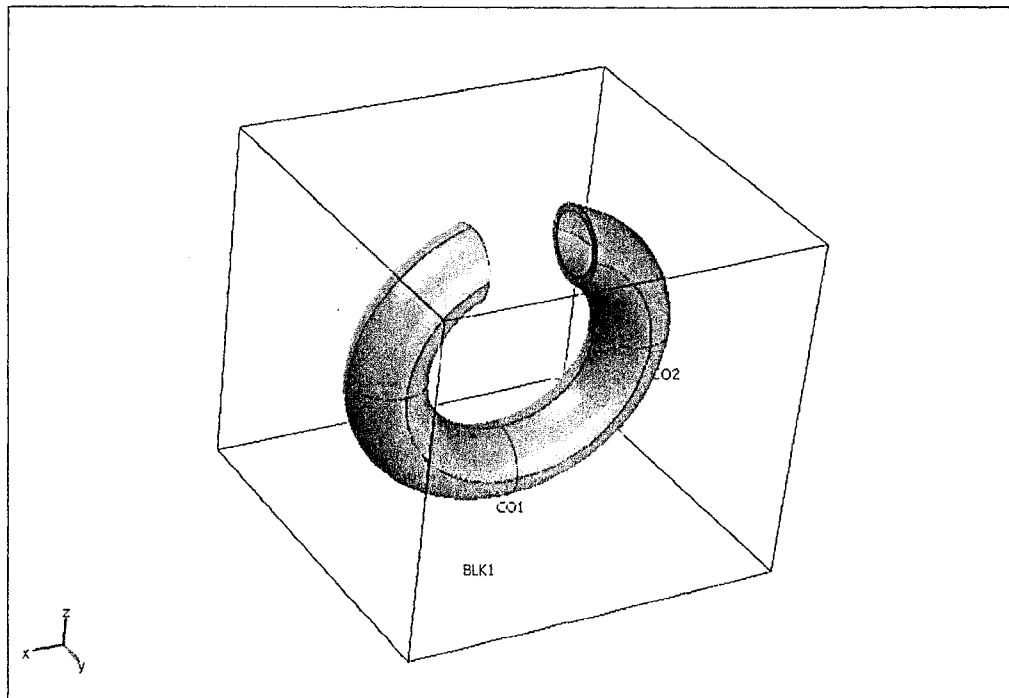


Figure 2.14 Comsol model for the electromagnet coil

Figure 2.15 shows an arrow plot of the current density of the electromagnetic coil. Figure 2.16 shows an arrow plot of the magnetic flux density. It is noted that the directions of the magnetic flux densities on surfaces A and B are not parallel to one

another. If the current density  $J_0$  determined using Equation (2.15) is used in the simulation, the magnitudes of the magnetic densities are quite different from those obtained using the approximate analytical method. In order to make the results from the Comsol model and those from the analytical model comparable,  $J_0$  is multiplied by an adjusting factor of 1.76 which was determined such that the magnetic density at the center of the opening from the Comsol model is as close as possible to that from the approximate analytical model. Figure 2.17 shows the magnetic flux densities in the  $x$ -direction on the center plane when the currents are of four different values  $I = -0.5$  A,  $I = -1.0$  A,  $I = -1.5$  A, and  $I = -2.0$  A, respectively. Multiplying Equation (2.15) by a factor of 1.76, the corresponding current densities are found to be  $J_0 = 1923.16 \times 10^3$  A/m<sup>2</sup>,  $2046.33 \times 10^3$  A/m<sup>2</sup>,  $3069.49 \times 10^3$  A/m<sup>2</sup>, and  $4092.65 \times 10^3$  A/m<sup>2</sup>, respectively. Under the condition of  $J_0 = 2046.33 \times 10^3$  A/m<sup>2</sup>, the magnetic flux density at the middle position is close to that of the analytic result as  $I = -1.0$  A. The magnetic flux density reaches the maximum at the position of two faces A and B, and the minimum at the middle position along the  $x$ -axis. The magnetic flux density corresponding to  $I = -1.0$  A is similar to that shown in Figure 2.6. It is noted that the magnetic flux density changes abruptly at two locations. The problem is possibly produced by using a single thin-shell torus to approximate the actual electromagnetic coil.

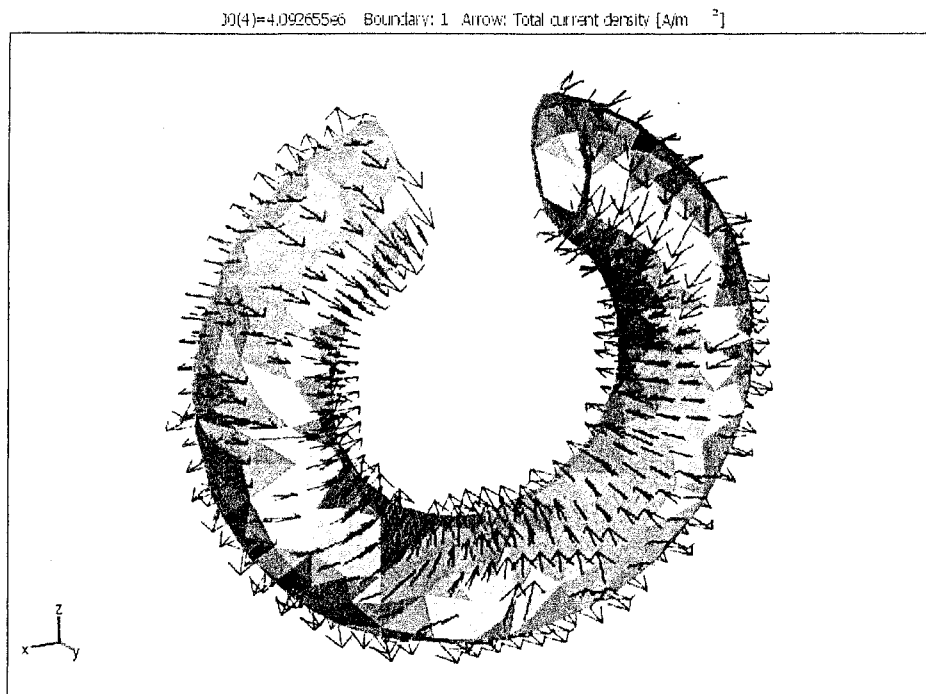


Figure 2.15 Arrow plot of the current density in the electromagnet coil.

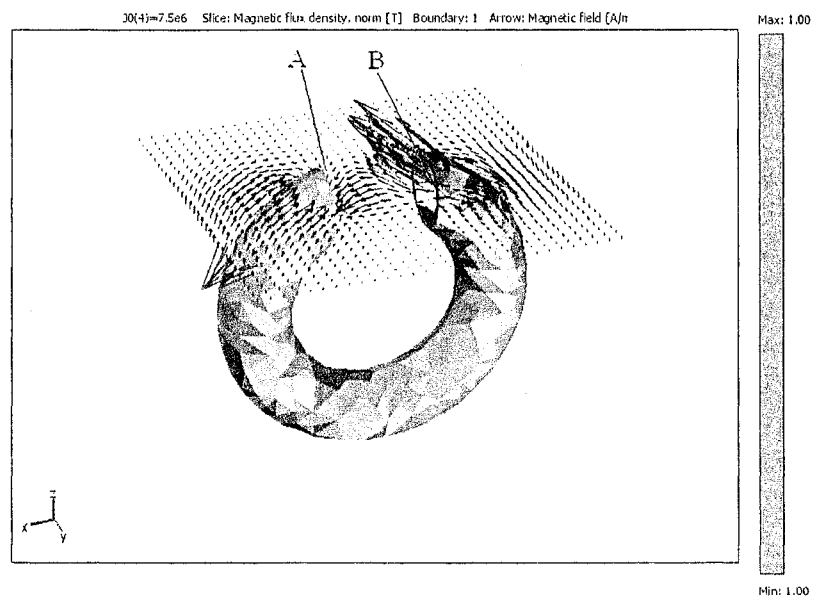


Figure 2.16 Arrow plot of the magnetic flux density of the coil



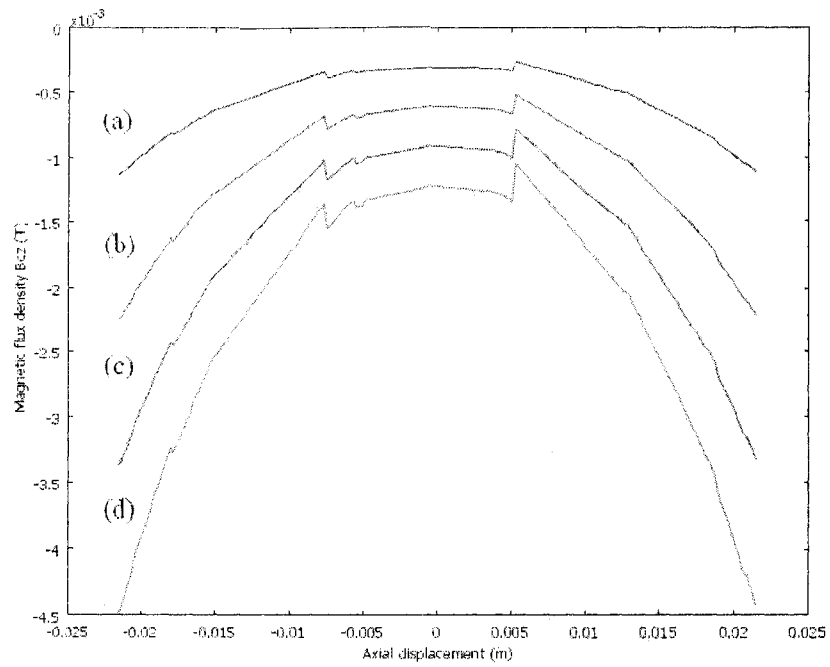


Figure 2.17 The axial magnetic flux density from the electromagnet along the centerline of the gap. (a)  $I = -0.5$  A; (b)  $I = -1.0$  A; (c)  $I = -1.5$  A; (d)  $I = -2.0$  A.

### 2.5.2 Simulation of the Coil with a Core

Figure 2.18 shows the model of the electromagnetic coil with a core in Comsol Multiphysics simulation. The model is built using AC/DC Module > Statics > Magnetostatics mode. Physical conditions of the hollow torus are the same as in Section 2.5.1. According to [33], the relative permeability of the core (iron) changes in a wide range, from 25 to  $200 \times 10^3$ . If the value of the relative permeability of the core increases, the magnetic flux density will also increase. It is found that when the relative permeability is 25 and current density  $J_0$  is multiplied by a factor of 3.5, the magnetic flux density curves are closest to those obtained in the analytic calculation given in Figure 2.7. As it was mentioned in Section 2.5.1, the model has only one torus which does not simulate the electromagnetic coils exactly. Thus some parameters have to be adjusted according to the analytic results.

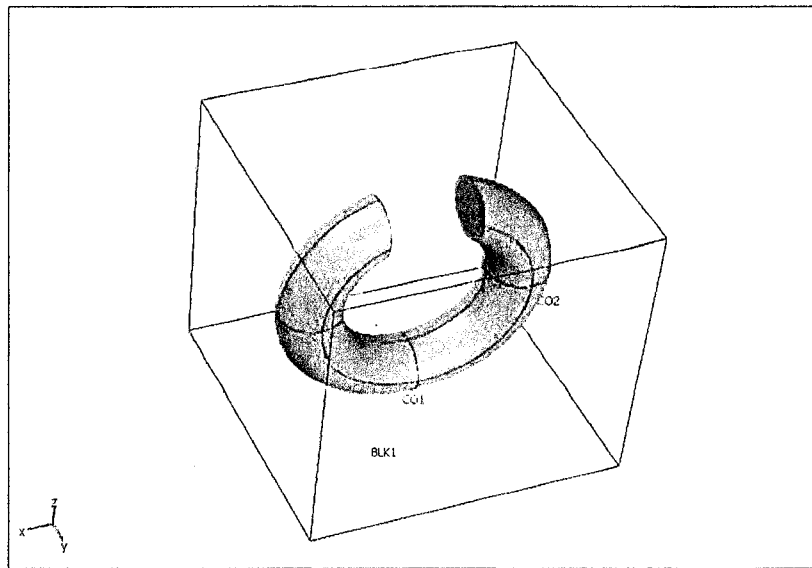


Figure 2.18 Model of the electromagnetic coil with the core.

Figure 2.19 shows an arrow plot of the coil with a core. The magnetic arrows radiate from surface A and converge on surface B. It is noted that with the core, the arrows of the magnetic density between the gap of the C-shape coil become nearly parallel to each other. Figure 2.20 shows the magnetic flux density along the  $x$ -axis in the centerline.

The magnetic flux density is increased greatly due to the effect of the core. The two abrupt change points in Figure 2.17 disappear. It may be due to the function of the core which “guides” the magnetic flux density in the circular direction of the coil.

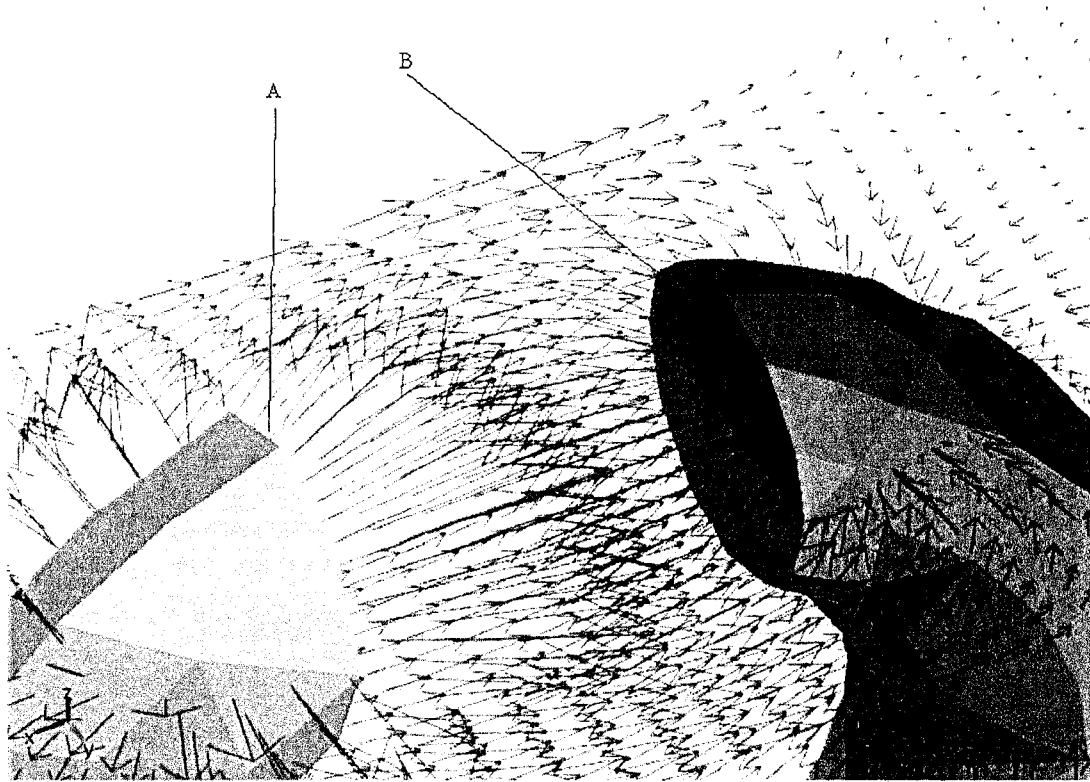


Figure 2.19 Arrow plot of the magnetic flux density of the coil with the core.

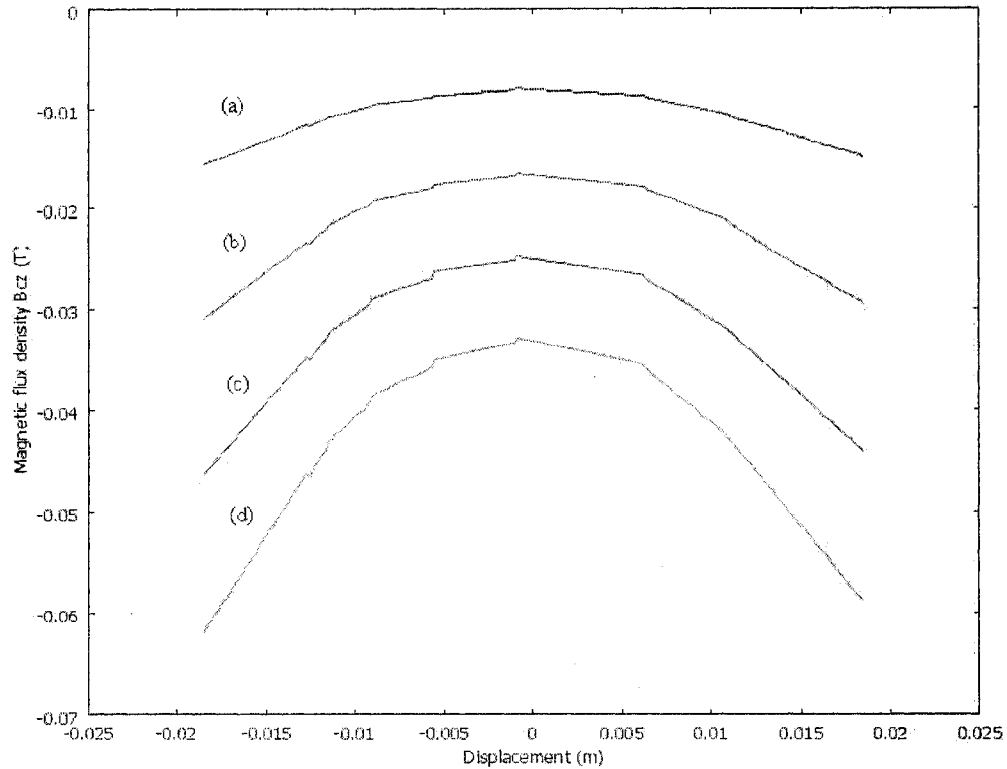


Figure 2.20 The axial magnetic flux density of the electromagnet with the core. The origin is at the gap center. (a)  $I = -0.5$  A; (b)  $I = -1.0$  A; (c)  $I = -1.5$  A; (d)  $I = -2.0$  A.

### 2.5.3 Simulation of the PM

The PM model built in Comsol Multiphysics is shown in Figure 2.21. The model is built using AC/DC Module>Statics>Magnetostatics mode, no current. The magnetization of the PM is  $395.8 \times 10^3$  A/m.

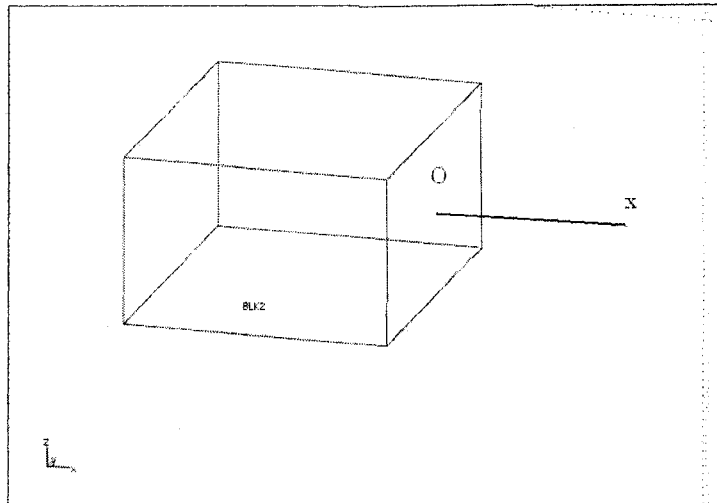


Figure 2.21 PM model

Figure 2.22 shows an arrow plot of the magnetic flux density field. Figure 2.23 shows the magnetic flux density of the PM, starting from the point “O” along the centerline ( $x$ -axis in Figure 2.21). The result is similar to that obtained by the analytic calculation (see Figure 2.12). The magnetic flux density decreases as the distance to the surface increases.

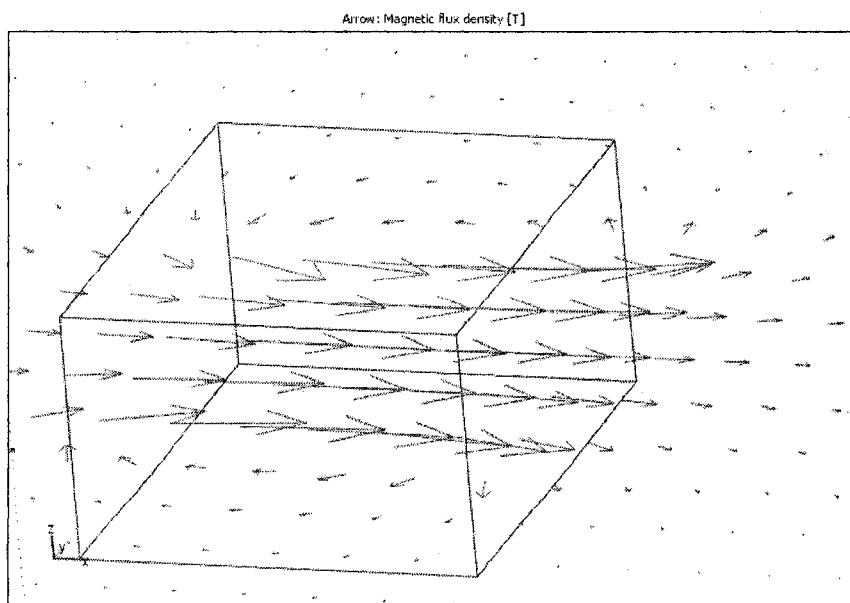


Figure 2.22 Arrow plot of the magnetic flux density of the PM

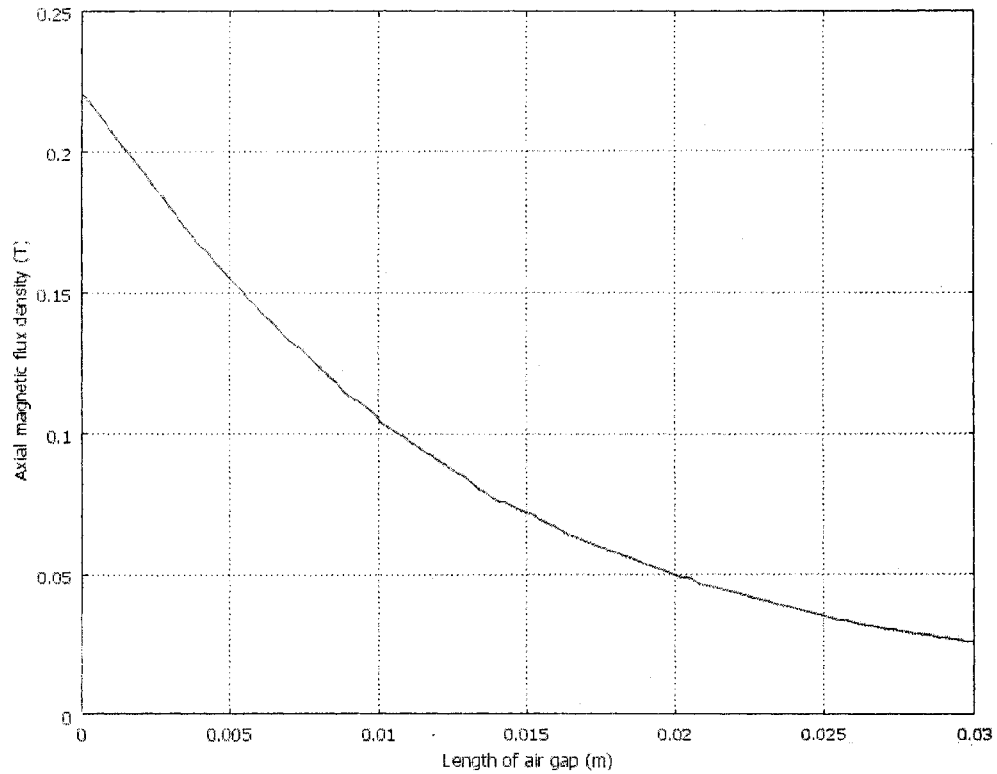


Figure 2.23 Magnetic flux density along the centerline of the PM with the origin located at the center of the pole face.

#### 2.5.4 Determination of the Interacting Force between the Core and the PM

Figure 2.24 shows the model with the PM in the gap of the core. To find the net force acting on the PM, the PM is placed in different locations along the centerline. Table 2.3 lists the PM positions and their corresponding magnetic forces. In the table  $\Delta k_i$  is calculated by

$$\Delta k_i = \frac{F_i - F_{i-1}}{x_i - x_{i-1}}, \quad i = 2, 3, \dots \quad (2.16)$$

where  $F_i$  is the force corresponding to the position  $x_i$  and  $F_{i-1}$  is the force corresponding to the position  $x_{i-1}$ . The average stiffness is  $-14.6 \times 10^3$  N/m. Figure 2.25 plots the simulation result together with a linear regression result. It is found that as the PM is in the middle of the gap, the force is small, and as the PM becomes closer to the core, the attracting force increases. Comparing with the result in Figure 2.13, the stiffness obtained by the present model is much greater than that obtained by the analytic calculation. This is expected because the distance between the PM and the core of the present setup is much smaller than that in [25]. Because it is a 3-D model which consumes much memory, it is impossible to select a finer mesh in the solution process.

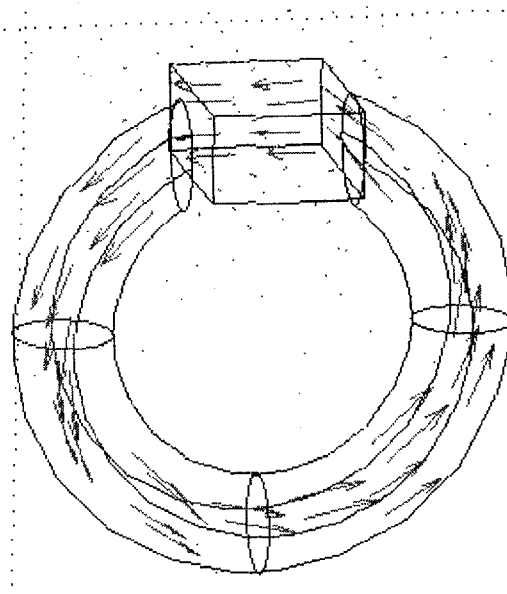


Figure 2.24 The PM placed in the gap of the core.

Table 2.3 Force and position

Position (m)	Force (N)	$\Delta k$ (N/m)	Position (m)	Force (N)	$\Delta k$ (N/m)
0.0000	0.4636		0.0000	0.4636	
0.0001	-1.7494	-12858	-0.0001	1.1587	-6951
0.0002	-1.9555	-2061	-0.0002	1.6165	-4578.5
0.0003	-3.8795	-19240	-0.0003	3.6867	-20702
0.0004	-6.0146	-21351	-0.0004	3.9812	-23647
0.0005	-5.9081	1065	-0.0005	5.8064	-18252
0.0006	-8.3227	-24146	-0.0006	6.8445	-10381
0.0007	-8.0918	2309	-0.0007	8.1986	-13541
0.0008	-9.7281	-16363	-0.0008	10.4380	-22394
0.0009	-10.8716	-11435	-0.0009	7.9760	24620
0.0010	-12.3860	-15144	-0.0010	12.0533	-44773
0.0011	-12.3869	-9	-0.0011	11.0886	9647
0.0012	-14.4446	-109423	-0.0012	14.9852	-38966
0.0013	-15.6732	-12286	-0.0013	15.6643	-6791
0.0014	-16.0735	-4003	-0.0014	16.1305	-4662
0.0015	-18.0213	-19478	-0.0015	18.4883	-23578
0.0018	-20.1370	-7052.3	-0.0018	20.8633	-7916.7
0.0020	-23.3599	-8057.3	-0.0020	24.6281	-9412
0.0022	-25.8830	-12615.5	-0.0022	26.8637	-11178

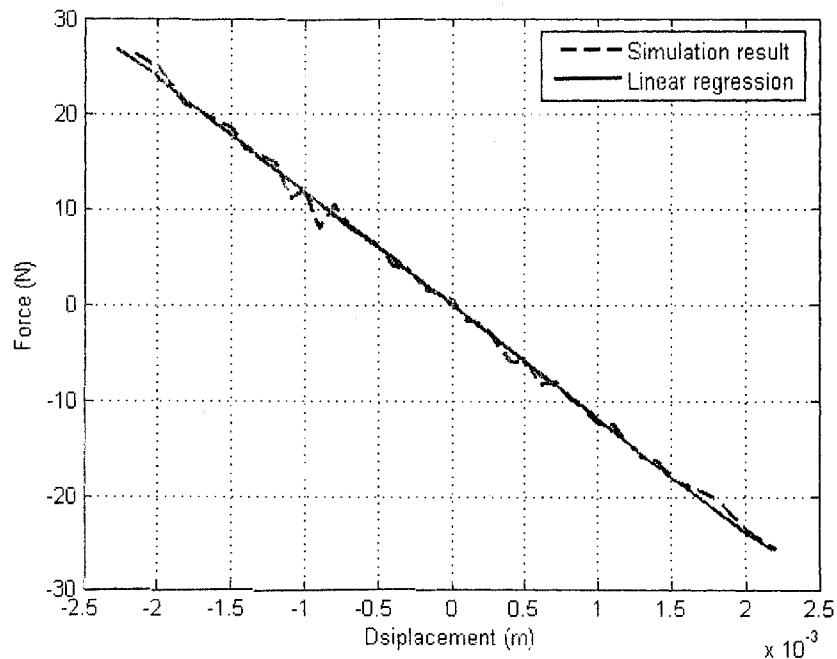


Figure 2.25 Force acting on the PM vs. its position



## 2.5.5 Determination of the Interacting Force Using a Simplified Model

When the PM is placed in the gap of the coil with a core shown in Figure 2.19, the electromagnetic force corresponding to the current can be found. Unfortunately, due to the limited memory of the computer, this kind of model cannot be run. Therefore a simplified model is used. The torus-like electromagnet is replaced by a pair of magnetic cylinders as shown in Figure 2.26. The magnetizations of the cylinders are chosen such that the magnetic flux density curves formed by the two magnetic cylinders are close to those in Figure 2.20, as shown in Figure 2.27. The magnetization values of each cylinder are adjusted to  $45 \times 10^3$ ,  $95 \times 10^3$ ,  $140 \times 10^3$ , and  $185 \times 10^3$  A/m. The PM with a magnetization of  $395.8 \times 10^3$  A/m is placed between these two cylinders and a simplified model is formed. Figure 2.28 shows this simplified model. By placing the PM on different positions between the gap of this pair of the PMs, the force applied on the PM varies. Table 2.4 shows the relationship between the magnetic force and the PM position in four different magnetizations. Figure 2.29 plots this relationship. The stiffness is around  $-1240$  N/m when the current is  $I = -2.0$  A. This means the adjustable range of the stiffness  $k_v$  is between  $-1240$  and  $1240$  N/m when the current is varied from  $I = -2.0$  A to  $I = 2.0$  A.

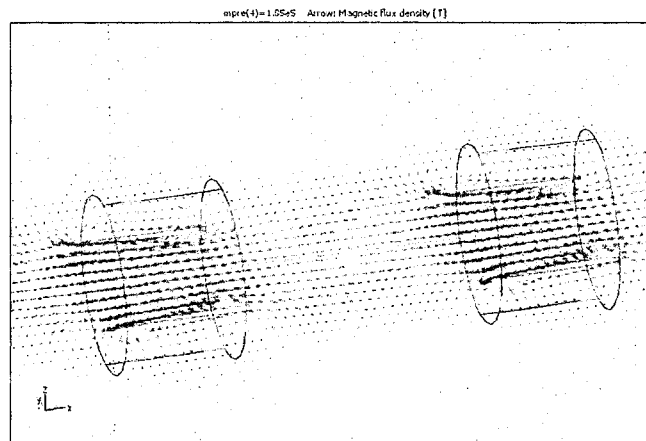


Figure 2.26 A pair of magnetic cylinders

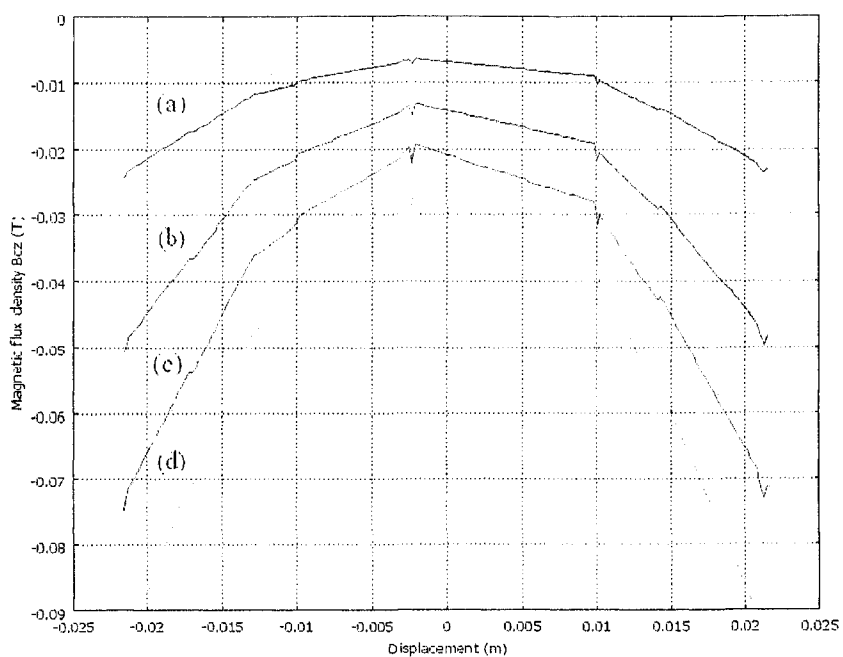


Figure 2.27 Magnetic flux density of the simplified model. The origin is at the gap center. (a)  $45 \times 10^3$  A/m ( $I = -0.5$  A); (b)  $95 \times 10^3$  A/m ( $I = -1.0$  A); (c)  $140 \times 10^3$  A/m ( $I = -1.5$  A); (d)  $185 \times 10^3$  A/m ( $I = -2.0$  A).

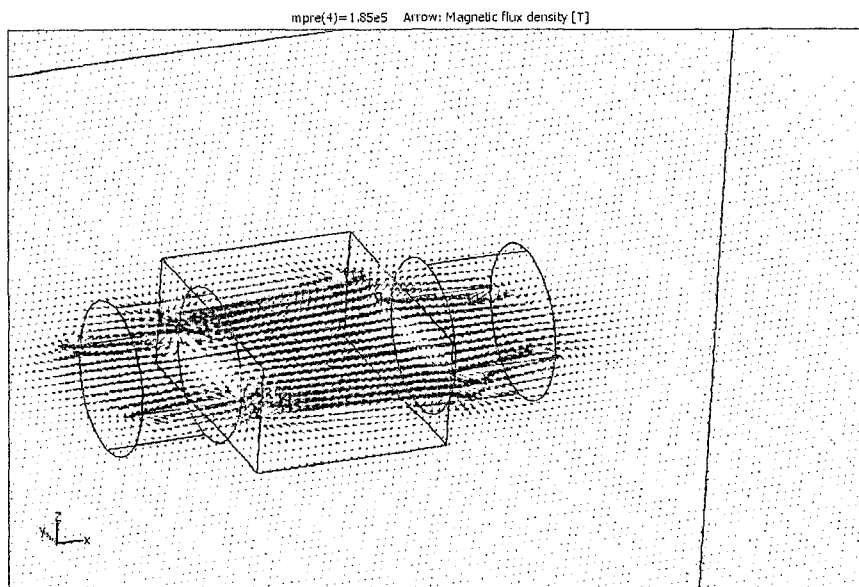


Figure 2.28 The simplified model with the PM

Table 2.4. Magnetic force and displacement

Displacement (m)	Magnetization (A/m)			
	45000	95000	140000	185000
0.0001	-0.0083	-0.0371	-0.0805	-0.1406
0.0002	-0.0183	-0.0814	-0.1768	-0.3086
0.0003	-0.0181	-0.0809	-0.1756	-0.3066
0.0004	-0.0274	-0.1221	-0.2652	-0.4631
0.0005	-0.0310	-0.1383	-0.3003	-0.5244
0.0006	-0.0386	-0.1718	-0.3731	-0.6515
0.0007	-0.0413	-0.1841	-0.3998	-0.6982
0.0008	-0.0584	-0.2601	-0.5649	-0.9865
0.0009	-0.0575	-0.2563	-0.5566	-0.9719
0.0010	-0.0723	-0.3222	-0.6997	-1.2218
0.0011	-0.0775	-0.3454	-0.7502	-1.3099
0.0012	-0.0872	-0.3886	-0.8439	-1.4737
0.0013	-0.0971	-0.4329	-0.9401	-1.6416
0.0014	-0.1061	-0.4730	-1.0272	-1.7937
0.0015	-0.1145	-0.5103	-1.1083	-1.9353
0.0016	-0.1188	-0.5294	-1.1497	-2.0076
0.0017	-0.1342	-0.5979	-1.2985	-2.2674
0.0018	-0.1401	-0.6243	-1.3558	-2.3674
0.0019	-0.1510	-0.6732	-1.4619	-2.5527
0.0020	-0.1461	-0.6511	-1.4140	-2.4691
0.0025	-0.1684	-0.7505	-1.6298	-2.8459

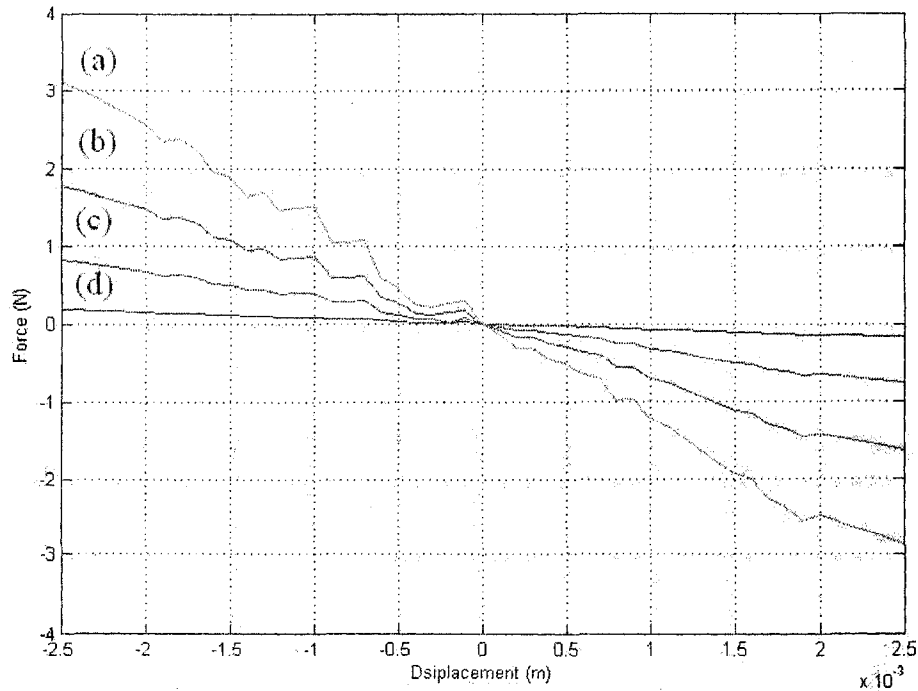


Figure 2.29 Force acting on the PM vs. its position: (a)  $I = -2.0$  A; (b)  $I = -1.5$  A; (c)  $I = -1.0$  A; (d)  $I = -0.5$  A.

### 2.5.6 Simulation of the Interaction of the PM, the Electromagnet, and the Beam

The previous simulations do not include the effect of the absorber beams. With the multiphysics functionality of Comsol, it is possible to build a model that couples the structural mechanics of the beam with the electromagnetic physics of the coil and the PM. To reduce the computational burden, a 2-D model is used. The model deals with magnets, force and structural deformation such that multiphysics modes are used. The model addresses a 2-way coupling between the deformations and the magnetic field. Figure 2.30 shows the model built. The electromagnet is replaced by a pair of PMs referred to as upper PM (R10) and lower PM (R15), which are fixed in space. A PM (R2) referred to as the middle PM is placed in the middle of the upper and lower PMs. Two beams (R1, R3) are attached to the left and right sides of the middle PM, respectively. The other end of each of the beams is fixed. The beam-middle-PM assembly will be deformed when it is

subjected to a force. The beams are made of aluminium with Young's modulus of  $7 \times 10^{10}$  Pa. The beam length is 0.1 m. Two different beam thicknesses, 0.0015 m (thick beam) and 0.001 m (thin beam), are considered. The size of the middle PM is  $0.048 \times 0.038$  (m) (*width*  $\times$  *height*). The size of the upper and lower PMs is  $0.048 \times 0.04$  (m) (*width*  $\times$  *height*). The magnetization of the middle PM is  $395.8 \times 10^3$  A/m. According to the polarity of the upper and lower PMs, two cases are studied. Figure 2.30 shows Case One in which the polarity of the upper and lower PMs is opposite to that of the middle PM, which corresponds to a positive current case in the electromagnet. In Case Two the polarity of the upper and lower PMs is reversed, which corresponds to a negative current case in the electromagnet.

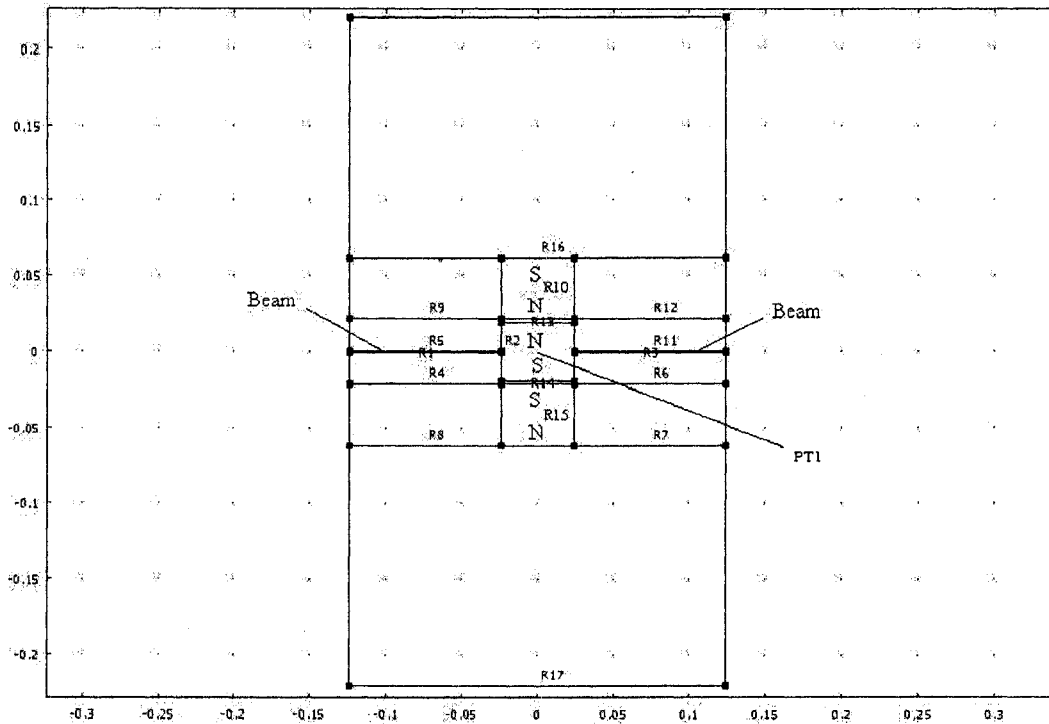


Figure 2.30 The 2-D coupling model.

The coupling model is built using three application modes: 1. the Perpendicular Induction Currents mode, Vector Potential in Quasi-Statics Magnetic from AC/DC

Module, 2. the Plane Strain mode from the Structural Mechanics Module, and 3. the Moving Mesh (ALE) mode from Multiphysics Module. First, the Perpendicular induction current application mode computes the magnetic force acting on the middle PM. Then the Plane strain application mode computes the deformation of the beams under the magnetic force and any external force applied. An iteration solution procedure must be used because the beam deformation will change the position of the middle PM so that the interacting magnetic force alters. The Moving Mesh (ALE-Arbitrary Lagrangian-Eulerian) application mode deals with the deformed mesh.

In the coupling model, the magnetizations of the upper and lower PMs are adjusted to the equivalent values in Section 2.5.5. The magnetic flux densities between the upper and the lower PMs without the middle PM can be found by setting the relative permeability of the middle PM to be that of the air. Figure 2.31 shows the magnetic flux densities along the center line of the lower and upper PMs. Note that the positive magnetization of the upper and lower PMs corresponds to Case Two mentioned previously. Figure 2.32 shows an arrow plot of the magnetic flux density when  $M = -185 \times 10^3$  A/m and the thick beams are used.

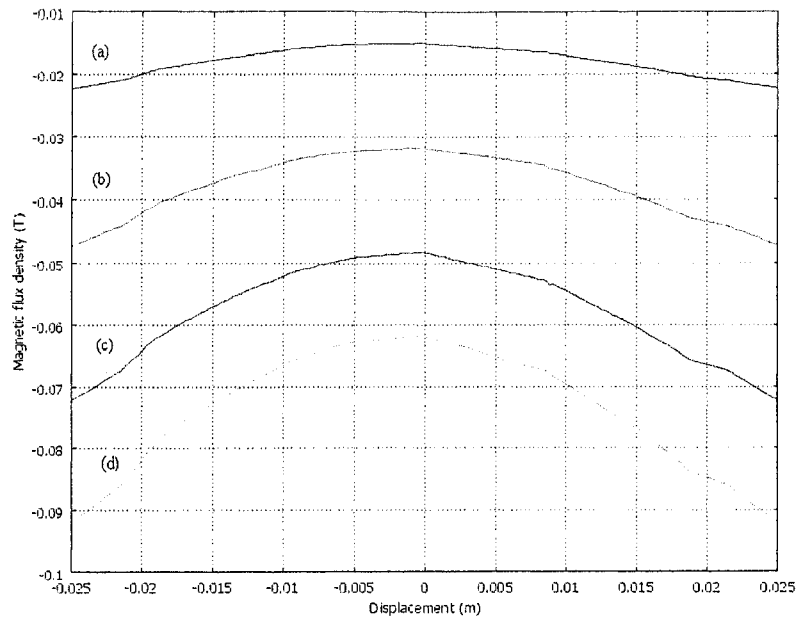


Figure 2.31 Magnetic flux density of the coupling model: (a)  $45 \times 10^3$  A/m ( $I = -0.5$  A); (b)  $95 \times 10^3$  A/m ( $I = -1.0$  A); (c)  $140 \times 10^3$  A/m ( $I = -1.5$  A); (d)  $185 \times 10^3$  A/m ( $I = -2.0$  A).

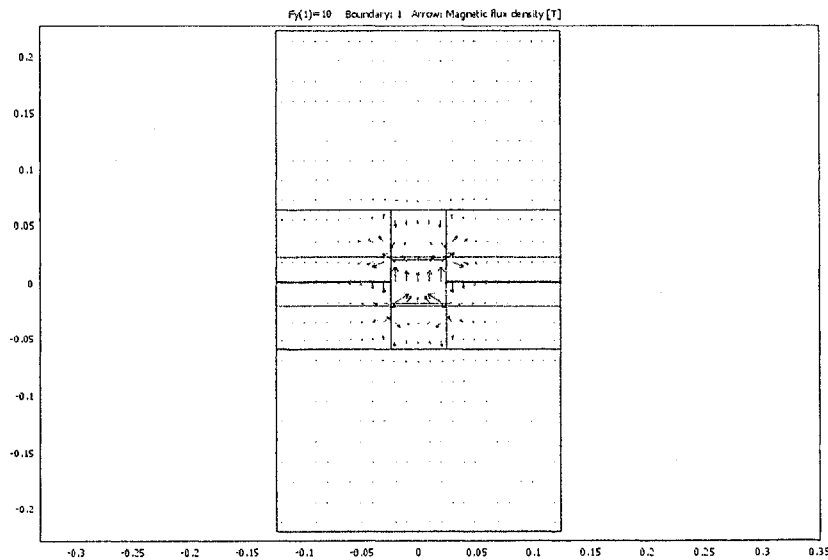


Figure 2.32 Arrow plot of the magnetic density for Case One.

To find the stiffness of this setup, an external force is applied in the center (PT1) of the middle PM in the  $y$ -direction. Then a simulation is conducted and the displacement of the middle PM is found. The relationship between the applied forces and the displacements

of the middle PM can be found. Figure 2.33 compares the results of both Case One and Case Two for the thick beam case. Figure 2.34 compares the results of both Case One and Case Two for the thin beam case. Figure 2.35 shows  $\Delta k$  corresponding to the displacement of the thick beam, where  $\Delta k$  is obtained by equation (2.16). From the figures, the following observations can be drawn. First, the relationship between the applied force and the displacement is not linear. Second, such a nonlinear relationship indicates that the setup possesses the characteristics of a harden spring, i.e., the stiffness increases with the increase of the spring deformation. Third, the increase of the magnetizations of the upper and lower PMs results in a decrease of the displacement of the middle PM, i.e., an increase of the magnetic stiffness. Fourth, a decrease of the magnetization magnitude will soften the magnetic spring. Fifth, Case Two softens the overall stiffness. Sixth, in Case One the stiffness  $\Delta k$  increases with an increase of the magnetization magnitude while in Case Two, the stiffness  $\Delta k$  decreases with an increase of the magnetization magnitude.

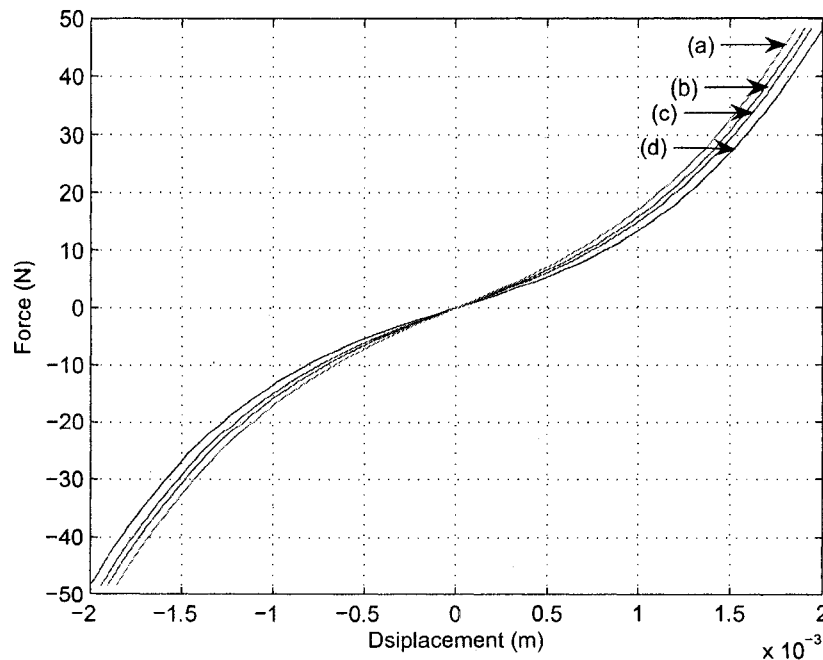


Figure 2.33 Force vs. displacement (thick beam): (a)  $-185 \times 10^3$  A/m; (b)  $-45 \times 10^3$  A/m; (c)  $45 \times 10^3$  A/m; (d)  $185 \times 10^3$  A/m.



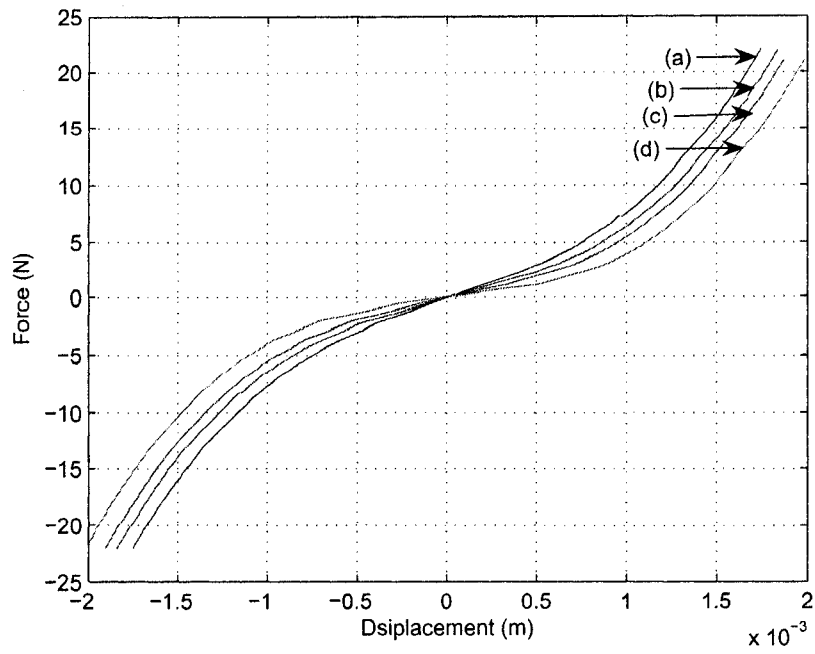


Figure 2.34 Force vs. displacement (thin beam): (a)  $-185 \times 10^3$  A/m; (b)  $-45 \times 10^3$  A/m; (c)  $45 \times 10^3$  A/m; (d)  $185 \times 10^3$  A/m.

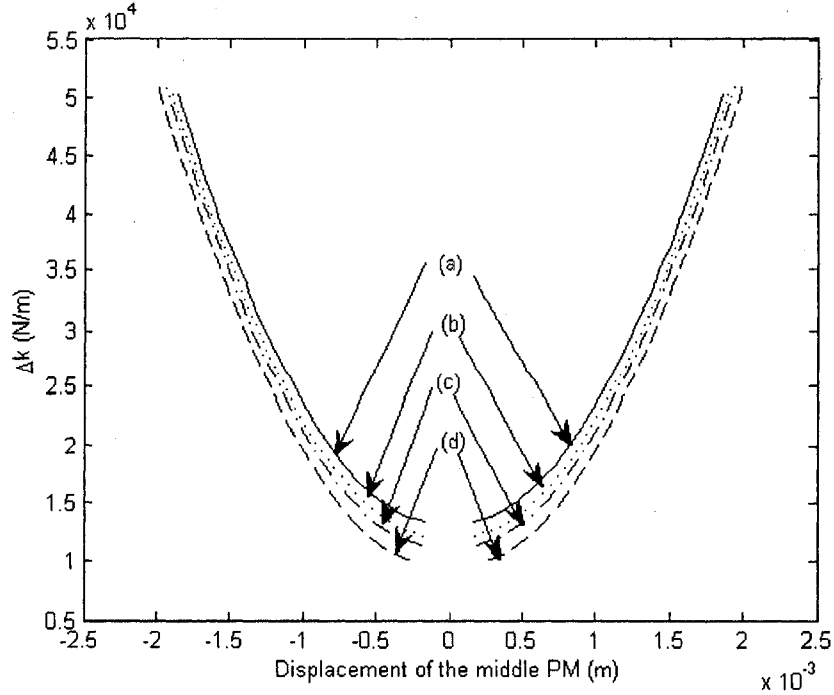


Figure 2.35  $\Delta k$  vs. displacement: (a)  $-185 \times 10^3$  A/m; (b)  $-45 \times 10^3$  A/m; (c)  $45 \times 10^3$  A/m; (d)  $185 \times 10^3$  A/m.

## 2.6 Comparison of the Two Techniques

The original intention of this study was to explore the possibility of using a commercial finite element package to characterize the EMVA. The experience has shown that building an accurate model for the EMVA using Comsol is challenging due to several factors such as a lack of a proper training in the use of Comsol and a memory limitation, etc. Nevertheless, the study has resulted in some useful experience and revealed a great potential in using Comsol to solve similar problems. It is found that Comsol Multiphysics is efficient in geometric modeling and dealing with a single physics problem such as electromagnetic physics. The trends found in the electromagnetism simulation using Comsol follow those from the approximate method. The study also shows that it is possible to simulate the EMVA under a multiphysics setting. The coupling model gives sensible results. However, it is noted that the multiphysics simulation demands a steep learning curve and extra effort in model building.

To build a model in Comsol Multiphysics, several factors have to be considered. 1. The geometric shape of a model. It is desirable to build a model that is “the same” as the real system. But in most cases it is limited by the memory of the computer. The problem “out of memory” often happens in a 3-D or coupling model. It is necessary to simplify the system such that the model can be run. In this chapter, the electromagnetic coil is built as a thin-shell torus. If the memory had allowed, many thin-shell toruses with different inner and external radius would have been built. 2. Determination of parameters. All parameters are supposed to equal to the physical parameters. As the shape of the model is different from the physical one, parameters have to be calibrated again based on the analytic and experimental results. 3. To simulate a physical model with an equivalent model, “physic conditions” (Comsol menu) should be selected to produce similar conditions. In this chapter, a 3-D PMs model and a 2-D PMs of the coupling model, which took the role of a 3-D electromagnetic coil with a core, were built by choosing the magnetization of the two PMs such that the magnetic flux density of these two models are the same. 4. The accuracy of the simulation results of Comsol Multiphysics is often limited by the mesh selection and the size of free space. A finer mesh decreases the error. But the degree of meshes is restricted by the computer memory. 5. Many difficulties were encountered in building the coupling model. Frequently the inverted mesh problem occurs. When working with the Moving Mesh (ALE) application modes to move things around, the computational mesh gets deformed. If the deformations become too large, some of the mesh elements may get inverted. This means that the accuracy of the solution deteriorates and eventually the solution will cease to converge. Sometimes the results from the coupling model do not seem to be sensible.

## **Chapter 3**

### **Analytic Study on Non-collocated Vibration Control**

In Chapter 2, EMVA is studied. This EMVA will be used in non-collocated vibration control. In order to control a non-collocated mass on by EMVA, it is necessary to analyze the system.

#### **3.1 Introduction**

When a periodic force exerts on a machine, vibration results. The vibration may cause damage to the machine. This periodic force may be caused internally (such as the imbalance) or externally (such as earthquake). Generally machine vibration affects the accuracy and the operation of the machine. In some extreme situations, if the machine vibrates in resonance, some parts will be overstressed, worn out or even fractured. In order to suppress the vibration, various methods are used. One of them is vibration absorber. When a vibration absorber is directly attached to a body to suppress its vibration, a collocated vibration control is obtained. Unfortunately, for some applications, it is not possible to collocate the vibration absorber at the location of interest. This is because vibration absorber is a passive vibration control device which has a narrow operation range. Thus it is usually used for suppression of vibration with a constant frequency. If the vibration frequency varies, a passive vibration absorber will not provide satisfactory performance over the frequency variations of the excitation. Adaptive-passive vibration absorber is a tunable device that is capable of maintaining the tuning condition in the event that the excitation frequency shifts. This chapter reviews the theory of non-collocated adaptive-passive vibration control [24].

#### **3.2 Vibration Absorber**

As shown in Figure. 3.1 (a), a mass  $m$  is supported by a spring  $k$  and a damper  $c$ . An external force  $f(t) = F_0 \sin(\omega t)$  is applied to the mass, where  $F_0$  is the magnitude and  $\omega$  the excitation frequency. Note that  $\omega = 2\pi f$  where the unit of  $\omega$  is rad/s and the unit of  $f$  is Hz (cycle/s).

If the frequency of the external force is equal to the natural frequency of the system, the system will vibrate in resonance. Under this condition, the displacement of the mass increases as time goes on, or will develop to infinite if no damping exists between the spring and the mass. This system is referred to as primary system.

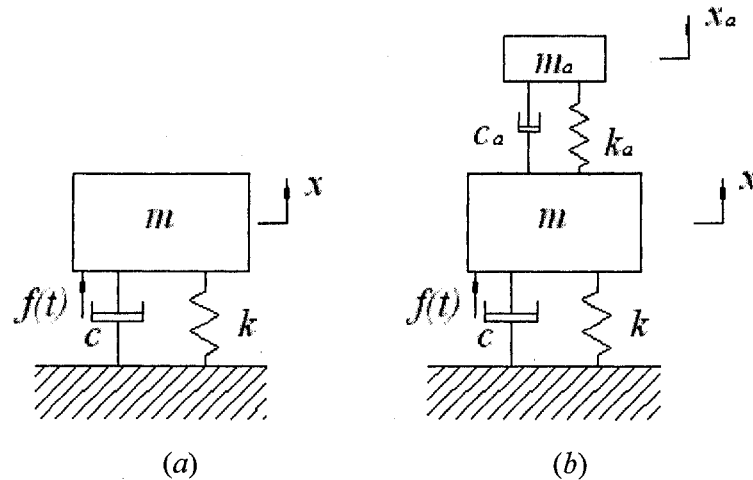


Figure 3.1 A primary system (a) and system with a vibration absorber (b).

As shown in Figure. 3.1 (b), a vibration absorber is attached to mass  $m$ . The vibration absorber consists of a spring  $k_a$ , a mass  $m_a$ , and a damper  $c_a$ . The governing equation of the new system is:

$$\begin{bmatrix} m & 0 \\ 0 & m_a \end{bmatrix} \begin{bmatrix} \ddot{x} \\ \ddot{x}_a \end{bmatrix} + \begin{bmatrix} c+c_a & -c_a \\ -c_a & c_a \end{bmatrix} \begin{bmatrix} \dot{x} \\ \dot{x}_a \end{bmatrix} + \begin{bmatrix} k+k_a & -k_a \\ -k_a & k_a \end{bmatrix} \begin{bmatrix} x \\ x_a \end{bmatrix} = \begin{bmatrix} f(t) \\ 0 \end{bmatrix} \quad (3.1)$$

The solution of the coupling equations can be separated as two parts: the transient and the steady-state. The transient response is not considered here because it dies out rapidly.

Only the steady-state response is considered. The magnitude of the steady-state vibration of the primary mass  $m$ , is

$$X(s) = \frac{(k_a - m_a \omega^2) F_0}{(k + k_a - m \omega^2)(k_a - m_a \omega^2) - k_a^2} \quad (3.2)$$

Note from equation (3.2) that the absorber parameters  $k_a$  and  $m_a$  can be chosen such that the magnitude of the steady-state vibration,  $X$ , is exactly zero. This is accomplished by satisfying the following condition:

$$\omega = \sqrt{\frac{k_a}{m_a}} \quad (3.3)$$

Equation (3.3) is referred to as the tuning condition of a passive vibration absorber.

### 3.3 Non-located Adaptive-passive Vibration Control of a 3-DOF System

A 3-degree-of-freedom (DOF) system, which is the primary system, is shown in Figure 3.2 (a). A force  $f(t) = F_0 \sin(\omega t)$  is applied on mass  $m_1$ . When the excitation frequency  $\omega$  is near any of the natural frequencies of the system  $f_i$  ( $i = 1 \sim 3$ ), the system vibrates at resonance. To control the vibration of the system, a passive vibration absorber is attached to mass  $m_3$ , as shown in Figure 3.2 (b). The system becomes a 4-DOF system. The objective of the control is to minimize the steady-state vibration of the non-located point of mass  $m_1$  by adjusting the stiffness of the vibration absorber  $k_a$ .

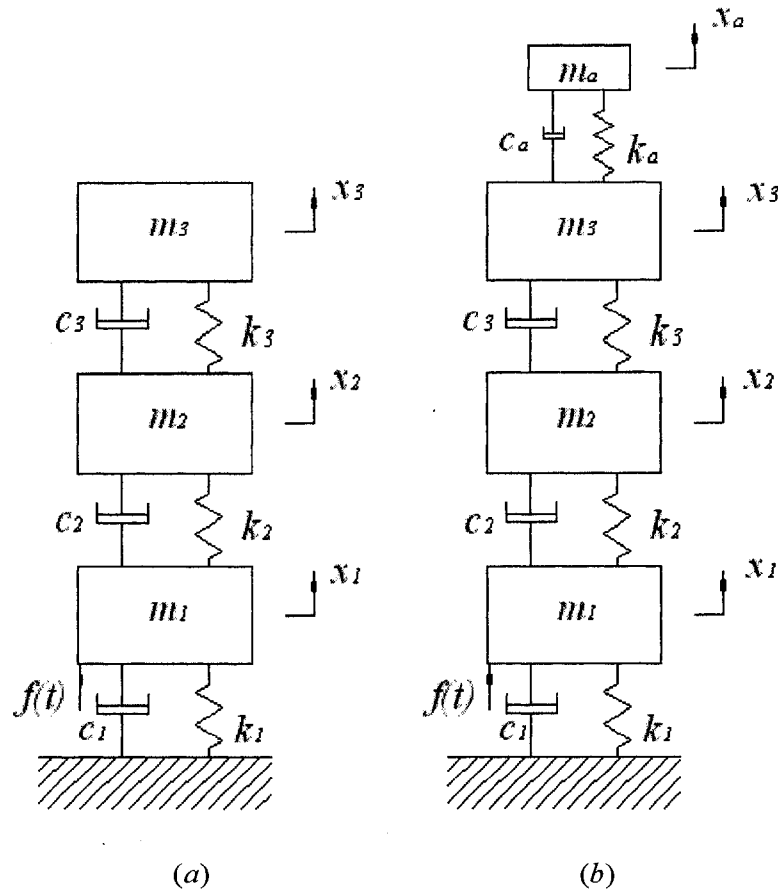


Figure 3.2 The 3-DOF primary system (a) and the system with a vibration absorber (b).

The governing equation of the entire system is given as follows:

$$\begin{bmatrix} m_1 & 0 & 0 & 0 \\ 0 & m_2 & 0 & 0 \\ 0 & 0 & m_3 & 0 \\ 0 & 0 & 0 & m_a \end{bmatrix} \begin{bmatrix} \ddot{x}_1 \\ \ddot{x}_2 \\ \ddot{x}_3 \\ \ddot{x}_a \end{bmatrix} + \begin{bmatrix} c_1 + c_2 & -c_2 & 0 & 0 \\ -c_2 & c_2 + c_3 & -c_3 & 0 \\ 0 & -c_3 & c_3 + c_a & -c_a \\ 0 & 0 & -c_a & c_a \end{bmatrix} \begin{bmatrix} \dot{x}_1 \\ \dot{x}_2 \\ \dot{x}_3 \\ \dot{x}_a \end{bmatrix} + \begin{bmatrix} k_1 + k_2 & -k_2 & 0 & 0 \\ -k_2 & k_2 + k_3 & -k_3 & 0 \\ 0 & -k_3 & k_3 + k_a & -k_a \\ 0 & 0 & -k_a & k_a \end{bmatrix} \begin{bmatrix} x_1 \\ x_2 \\ x_3 \\ x_a \end{bmatrix} = \begin{bmatrix} f(t) \\ 0 \\ 0 \\ 0 \end{bmatrix} \quad (3.4)$$

To find the amplitude  $X_1$  of the steady-state response of mass  $m_1$ , Laplace transform is used, and the following equation is obtained:

$$X(s) = A^{-1}F(s) \quad (3.5)$$

where

$$A = \begin{bmatrix} m_1 s^2 + (c_1 + c_2)s + (k_1 + k_2) & -c_2 s - k_2 & 0 & 0 \\ -c_2 s - k_2 & m_2 s^2 + (c_2 + c_3)s + (k_2 + k_3) & -c_3 s - k_3 & 0 \\ 0 & -c_3 s - k_3 & m_3 s^2 + (c_3 + c_a)s + (k_3 + k_a) & -c_a s - k_a \\ 0 & 0 & -c_a s - k_a & m_a s^2 + c_a s + k_a \end{bmatrix}$$

$$X(s) = \begin{bmatrix} X_1(s) \\ X_2(s) \\ X_3(s) \\ X_a(s) \end{bmatrix}$$

$$F(s) = \begin{bmatrix} F(s) \\ 0 \\ 0 \\ 0 \end{bmatrix}$$

The transfer function between  $F(s)$  and  $X_1(s)$  of mass  $m_1$  is

$$G_{11}(s) = \frac{X_1(s)}{F(s)} = \frac{N_1(s)}{D(s)} \quad (3.6)$$

where  $D(s) = \det(A)$ , i.e., the determinant of  $A$ , or the characteristic equation (CE) of the system.



and

$$N_1(s) = \det \begin{bmatrix} m_2 s^2 + (c_2 + c_3)s + (k_2 + k_3) & -c_3 s - k_3 & 0 \\ -c_3 s - k_3 & m_3 s^2 + (c_3 + c_a)s + (k_3 + k_a) & -c_a s - k_a \\ 0 & -c_a s - k_a & m_a s^2 + c_a s + k_a \end{bmatrix} =$$

$$\begin{aligned} & m_2 m_3 m_a s^6 + (m_2 c_3 m_a + m_2 c_a m_a + c_2 m_3 m_a + c_3 m_3 m_a + m_2 m_3 c_a) s^5 + (m_2 c_3 c_a + k_3 m_3 m_a \\ & + c_2 m_3 c_a + m_2 m_3 k_a + m_2 k_3 m_a + c_2 c_3 m_a + m_2 k_a m_a + c_3 m_3 c_a + c_2 c_a m_a + k_2 m_3 m_a + c_3 c_a m_a) s^4 \\ & + (k_2 c_3 m_a + k_3 c_a m_a + c_2 c_3 c_a + c_3 m_3 k_a + k_3 m_3 c_a + m_2 k_3 c_a + m_2 c_3 k_a + k_2 m_3 c_a + k_2 c_a m_a + \\ & c_2 m_3 k_a + c_2 k_3 m_a + c_2 k_a m_a + c_3 k_a m_a) s^3 + (k_3 m_3 k_a + k_2 k_3 m_a + k_3 k_a m_a + k_2 k_a m_a + c_2 c_3 k_a + \\ & k_2 m_3 k_a + k_2 c_3 c_a + m_2 k_3 k_a + c_2 k_3 c_a) s^2 + (k_2 k_3 c_a + k_2 c_3 k_a + c_2 k_3 k_a) s + k_2 k_3 k_a \end{aligned} \quad (3.7)$$

where  $N_1(s)$  is the determinant of a system including the absorber system and the intervening structure, i.e., the system involving  $m_2$  and  $m_3$ . This system is called the subsystem. When  $N_1(s)$  is zero, the roots of this characteristic equation are the natural frequencies of the subsystem, denoted as  $f_{si}$  ( $i = 1, 2, 3$ ).

In order to completely attenuate  $X_1(s)$ , there must exist a real value  $k_a$  such that  $N_1(s)$  is zero for  $s = j\omega$ , where  $j = \sqrt{-1}$ . The equation of finding the zeros of  $N_1(s)$  can be rewritten in the form:

$$\begin{aligned} & 1 + k_a [(m_2 m_a + m_2 m_3) s^4 + (c_2 m_a + c_2 m_3 + c_3 m_a + c_3 m_3 + m_2 c_3) s^3 + (k_3 m_3 \\ & + k_3 m_a + k_2 m_a + c_2 c_3 + m_2 k_3 + k_2 m_3) s^2 + (c_2 k_3 + k_2 c_3) s + k_2 k_3] / D_1(s) = 0 \end{aligned} \quad (3.8)$$

or

$$1 + k_a G(s) = 0 \quad (3.9)$$

where

$$\begin{aligned}
D_1(s) = & m_2 m_3 m_a s^6 + (c_2 m_3 m_a + m_2 c_3 m_a + c_3 m_3 m_a + m_2 m_3 c_a + m_2 c_a m_a) s^5 \\
& + (c_3 m_3 c_a + k_2 m_3 m_a + m_2 k_3 m_a + m_2 c_3 c_a + c_3 c_a m_a + c_2 m_3 c_a + c_2 c_3 m_a + c_2 c_a m_a + k_3 m_3 m_a) s^4 \\
& + (k_2 c_a m_a + k_2 m_3 c_a + k_2 c_3 m_a + c_2 k_3 m_a + k_3 c_a m_a + c_2 c_3 c_a + k_a m_3 c_a) s^3 \\
& + (c_2 k_3 c_a + k_2 k_3 m_a + k_2 c_3 c_a) s^2 + k_2 k_3 c_a s
\end{aligned}$$

and

$$\begin{aligned}
G(s) = & [(m_2 m_a + m_2 m_3) s^4 + (c_2 m_a + c_2 m_3 + c_3 m_a + c_3 m_3 + m_2 c_3) s^3 + (k_3 m_3 \\
& + k_3 m_a + k_2 m_a + c_2 c_3 + m_2 k_3 + k_2 m_3) s^2 + (c_2 k_3 + k_2 c_3) s + k_2 k_3] / D_1(s)
\end{aligned}$$

The problem can be considered as a typical problem of root locus,  $1 + k_a G(s) = 0$ . The dynamic analysis will proceed as a standard root locus analysis where the system gain to be varied is the vibration absorber spring stiffness  $k_a$ .

In this study, the objective is to suppress the vibration of mass  $m_1$  by changing the absorber stiffness  $k_a$ . The only variant in this subsystem is  $k_a$ . The system is considered as a SISO (Single-Input-Single-Output) system. The transfer function of the subsystem can be written as

$$\frac{X_a(s)}{X_1(s)} = \frac{N_a(s)}{F(s)} \frac{F(s)}{X_1(s)} = \frac{N_a(s)}{N_1(s)} \quad (3.10)$$

The zeros are the roots of the characteristic equation of the subsystem, meaning that when one of the subsystem's frequencies matches the excitation frequency, the displacement of mass  $m_1$  is suppressed. The roots are also referred to as anti-resonance frequencies of the new 4-DOF system. If there exists damping between the absorber and other part of the subsystem, the vibration magnitude of  $m_1$  cannot be attenuated to zero.

In order to suppress the vibration of mass  $m_1$  when the frequency of the excitation frequency is equal to one of the natural frequencies of the primary system, the stiffness of the absorber is chosen such that the anti-resonance of the new 4-DOF system matches the excitation frequency.

### 3.4 Undamped 3-DOF System

Considering the condition without damping in the system, equation (3.8) becomes to

$$1 + k_a \frac{(m_2 m_a + m_2 m_3) s^4 + (k_3 m_3 + k_3 m_a + k_2 m_a + m_2 k_3 + k_2 m_3) s^2 + k_2 k_3}{m_a s^2 [m_2 m_3 s^4 + (k_3 m_3 + m_2 k_3 + k_2 m_3) s^2 + k_2 k_3]} = 0 \quad (3.11)$$

Equation (3.11) can be written in the factored form,

$$1 + k_a \frac{(m_2 m_3 + m_2 m_a)(s^2 + \omega_A^2)(s^2 + \omega_C^2)}{m_a (m_2 m_3) s^2 (s^2 + \omega_B^2)(s^2 + \omega_D^2)} = 0 \quad (3.12)$$

When  $k_a = 0$ , equation (3.12) becomes

$$(s^2 + \omega_B^2)(s^2 + \omega_D^2) = 0 \quad (3.13)$$

When  $k_a = \infty$ , equation (3.12) becomes

$$(s^2 + \omega_A^2)(s^2 + \omega_C^2) = 0 \quad (3.14)$$

The case of  $k_a = 0$  is equivalent to an absence of the absorber system. The absorber mass  $m_a$  has no connection with the primary system. The case of  $k_a = \infty$  is equivalent to a rigid connection of  $m_a$  to  $m_3$ . Under these two bounded conditions, the system in Figure 3.2 (b) becomes the systems shown in Figures 3.3 (a) and 3.3 (b), respectively.

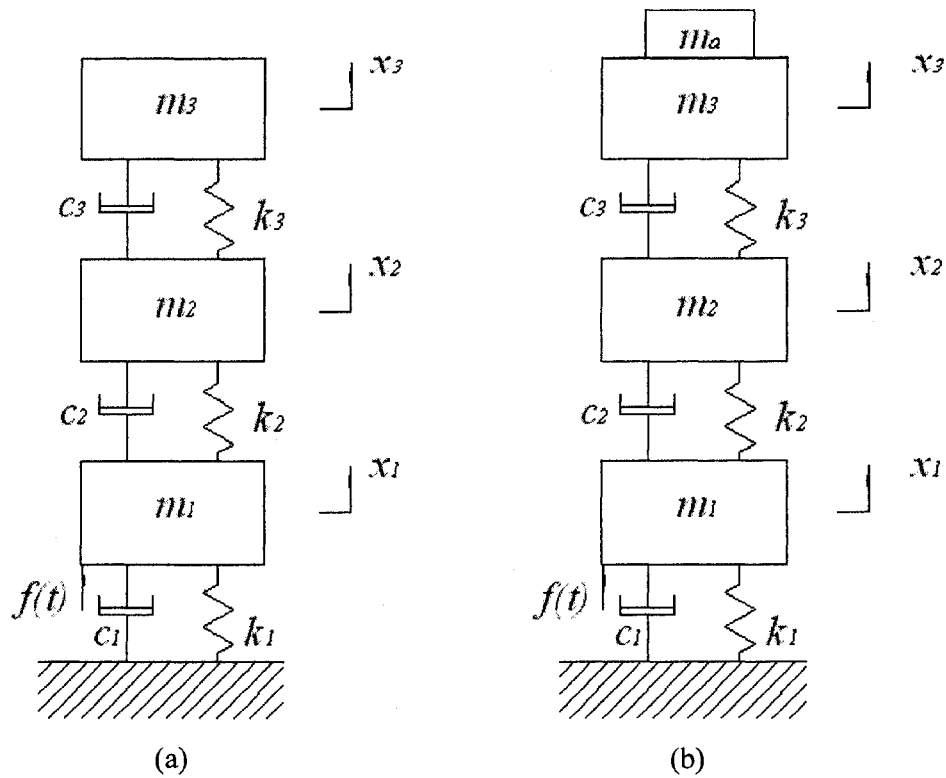


Figure 3.3 (a)  $k_a = 0$ ; (b)  $k_a = \infty$ .

Using the values in Table 3.1, when the stiffness changes between  $k_a = 0$  and  $k_a = \infty$ , frequency response of mass  $m_1$  is shown in Figure. 3.4. In Figure 3.4, A, B, C and D represent  $\omega_A$ ,  $\omega_B$ ,  $\omega_C$  and  $\omega_D$ , respectively.

As  $k_a$  changes from zero to infinity, the natural frequencies of the subsystem change in the ranges:  $0 \leq \omega_{s1} \leq \omega_A$ ,  $\omega_B \leq \omega_{s2} \leq \omega_C$ , and  $\omega_D \leq \omega_{s3} \leq \omega_\infty$  respectively. When the excitation frequency is between the ranges  $\omega_A \leq \omega \leq \omega_B$  and  $\omega_C \leq \omega \leq \omega_D$ , the vibration of mass  $m_1$  cannot be suppressed to zero.

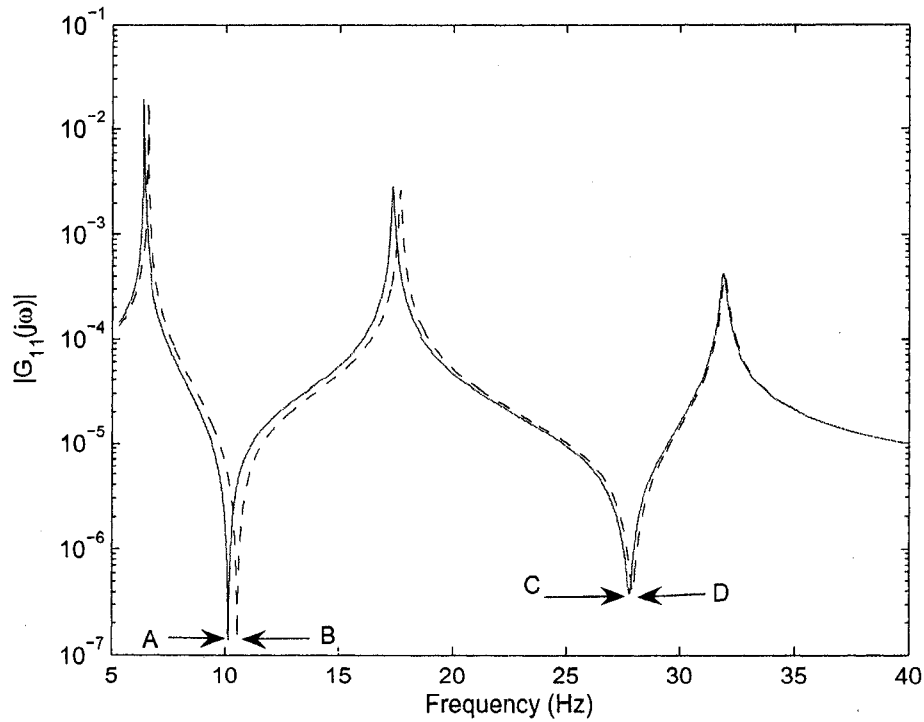


Figure 3.4 Frequency response of the entire system: solid line,  $k_a = \infty$ ; dashed line,  $k_a = 0$ .

### 3.5 Frequency Response of the Primary System and the System with the Vibration Absorber

To better understand the analysis presented in the previous section, various frequency responses are computed using the numerical values given in Table 3.1. These parameter values are chosen to be as close as possible to a physical model given in the next chapter.

Figure 3.5 shows the frequency response of mass  $m_1$  of the primary system. The primary system has three natural frequencies. In terms of displacement, the resonance at the first natural frequency results in the largest magnitude. The three natural frequencies of the primary system are  $f_1 = 6.59$  Hz,  $f_2 = 17.70$  Hz, and  $f_3 = 32.15$  Hz, respectively.

Table 3.1 System parameters

Symbol	Description	Quantity, Unit
$m_1$	Mass	2.73 kg
$m_2$	Mass	2.048 kg
$m_3$	Mass	2.635 kg
$m_a$	Absorber mass	0.2515 kg
$c_1$	Damping coefficient	1 Ns/m
$c_2$	Damping coefficient	1 Ns/m
$c_3$	Damping coefficient	1 Ns/m
$c_a$	Damping coefficient of absorber damper	0
$k_1$	Stiffness of spring	17183 N/m
$k_2$	Stiffness of spring	35401 N/m
$k_3$	Stiffness of spring	20616 N/m
$k_a$	Stiffness of absorber spring	Tunable

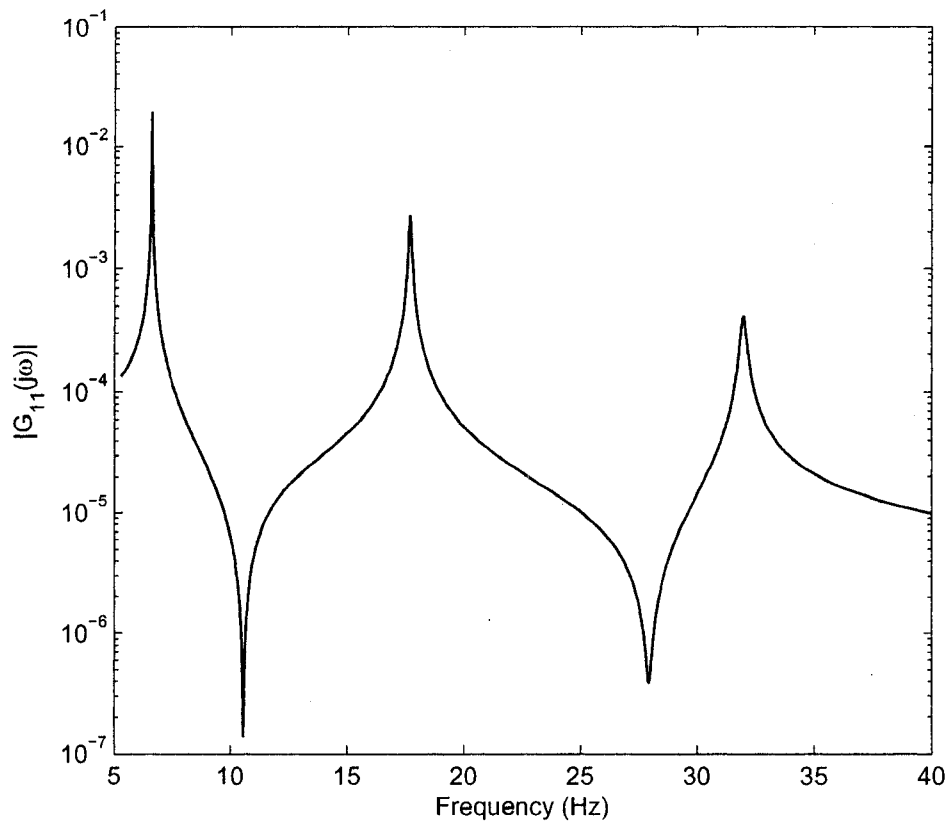


Figure 3.5 Frequency response of the primary system

Figure 3.6 compares the frequency response  $|G_{11}(j\omega)|$  of mass  $m_1$  of the primary system (solid line) and the frequency responses  $|G_{11}(j\omega)|$  of mass  $m_1$  of the entire system when  $f = f_{s1}$  (dotted line),  $f = f_{s2}$  (dashdot line), and  $f = f_{s3}$  (dashed line), respectively. These are the lower bounds that can be achieved when  $k_a$  is tuned in the range of  $320 \text{ N/m} \leq k_a \leq 21200 \text{ N/m}$ . It can be seen that with a tuned absorber, the amplitude of mass  $m_1$  can be suppressed significantly.

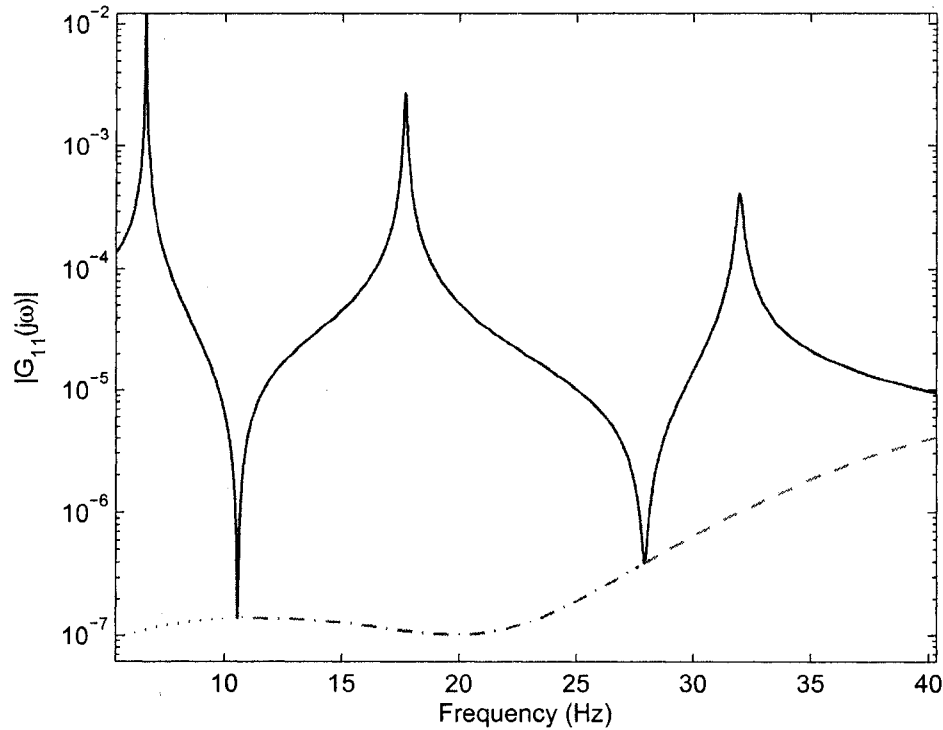


Figure 3.6 Frequency Response and lower bound of the optimum tuning: solid line, Primary system response; lower bound response, when  $f_{s1} = f$  (dotted line),  $f_{s2} = f$  (dashdot line), and  $f_{s3} = f$  (dashed line).

The objective of adding a vibration absorber is to suppress  $X_1$  at  $f_i$  ( $i=1\sim 3$ ), one of the three natural frequencies of the primary system. The absorber stiffness  $k_a$  must be set such that  $f_{si} = f_i$ . Figure 3.7 shows, as the absorber stiffness  $k_a$  changes from 0.1 N/m to 25,000 N/m, the differences between the natural frequencies of the subsystem and the natural frequencies of the primary system, so as to find the optimal stiffnesses of the absorber. The three optimal stiffnesses are represented by three points at which the curves cross with  $x$ -axis. They are  $k_{a1} = 457$  N/m,  $k_{a2} = 2785$  N/m, and  $k_{a3} = 8963$  N/m. As the stiffness reaches the optimal point, one of the natural frequencies of the subsystem  $f_{si}$



matches the natural frequency of the primary system  $f_i$  such that the vibration of mass  $m_i$  is zero if the excitation frequency  $f$  equals to  $f_i$  ( $i=1\sim 3$ ).

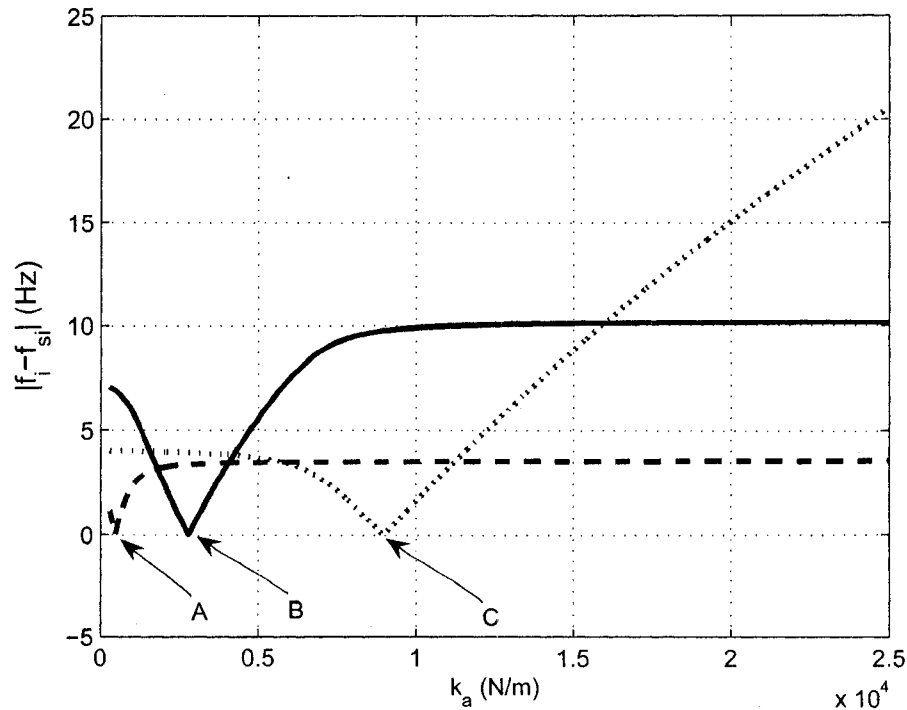


Figure 3.7 Optimal stiffness for three natural frequencies of the primary system: dashed line,  $|f_1 - f_{s1}|$ ; solid line,  $|f_2 - f_{s2}|$ ; dotted line,  $|f_3 - f_{s3}|$ .

Figure 3.8 shows a comparison of  $|G_{11}(j\omega)|$  of the primary system and those of the entire system when  $f_{s_i} = f_i$  ( $i=1\sim 3$ ). In each scenario, when one of the subsystem's natural frequencies  $f_{s_i}$  ( $i=1\sim 3$ ) matches one of the natural frequencies of the primary system  $f_i$  ( $i=1\sim 3$ ), the frequency response of the entire system separates into two low peaks around the peak  $f_i = f_{s_i}$ , and between them there is the anti-resonance point.

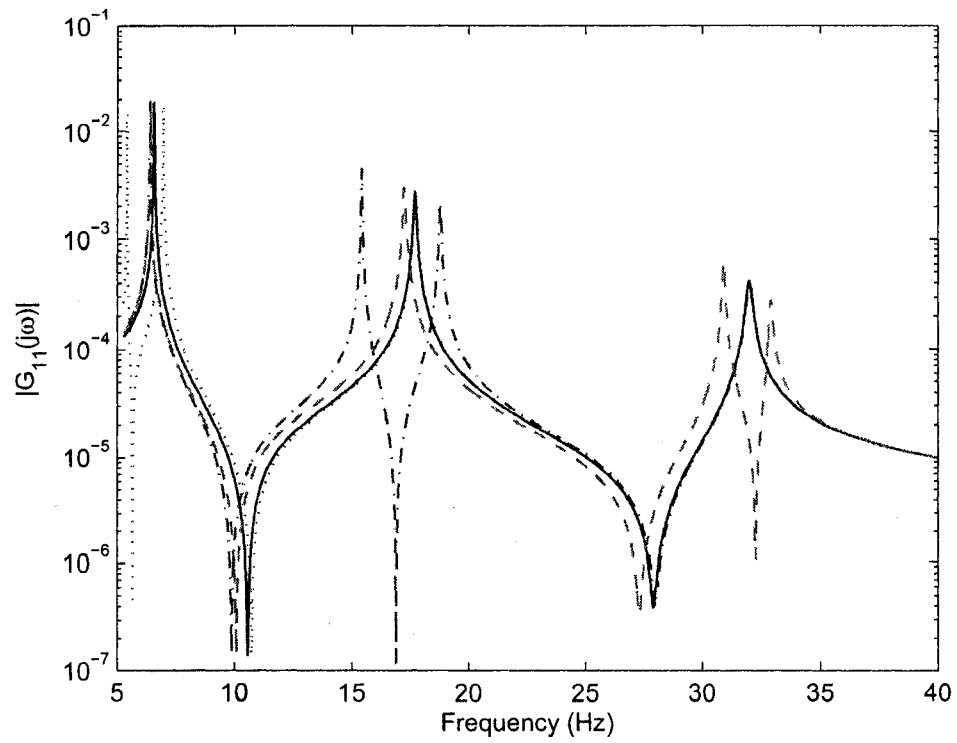


Figure 3.8  $|G_{11}(j\omega)|$  of the primary system and of the entire system as  $f_{s1} = f_1$  (dotted line),  $f_{s1} = f_1$  (dashdot line), and  $f_{s1} = f_1$  (dashed line).

## Chapter 4

### Experimental Studies

The previous chapter has analyzed a 3-DOF primary system and found that the vibration of mass  $m_1$  is suppressed when one of the natural frequencies of the subsystem equals to the excitation frequency. This chapter is devoted to implement the non-collocated vibration using the modified EMVA.

#### 4.1 Description of the Experimental Setup

Figure 4.1 shows the experimental system which includes five parts: primary system, absorber system, data collection system, computer control system, and shaker system.

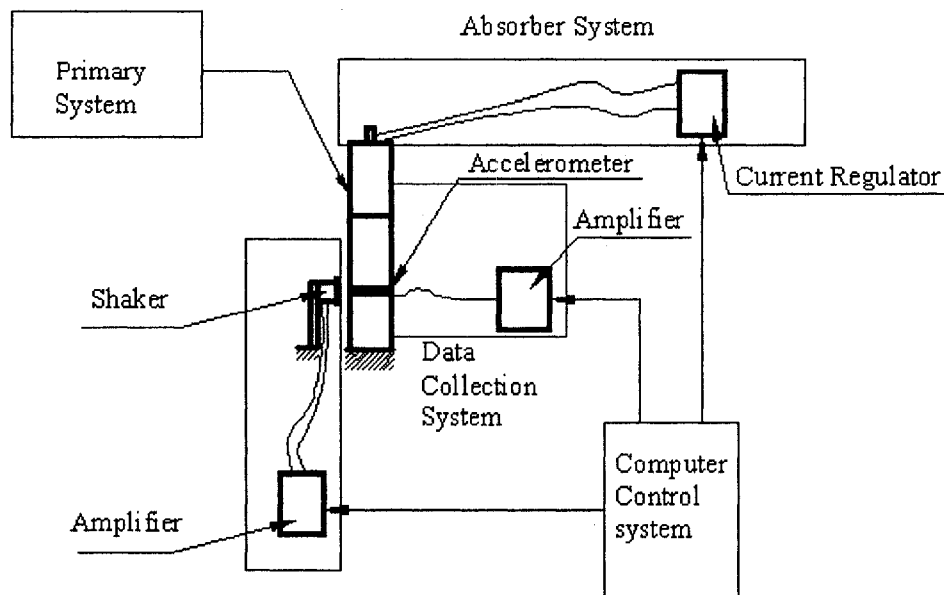


Figure 4.1 Experiment system

Figure 4.2 is a photograph of the experiment model. The primary system is formed by two vertical aluminium plates and three aluminium slabs. The slabs are fastened between the two plates by bolts. The structure is fastened to a base (see Figure 4.3). The absorber

system, which has been described in Chapter 2, is fastened on the top of the third aluminium slab.

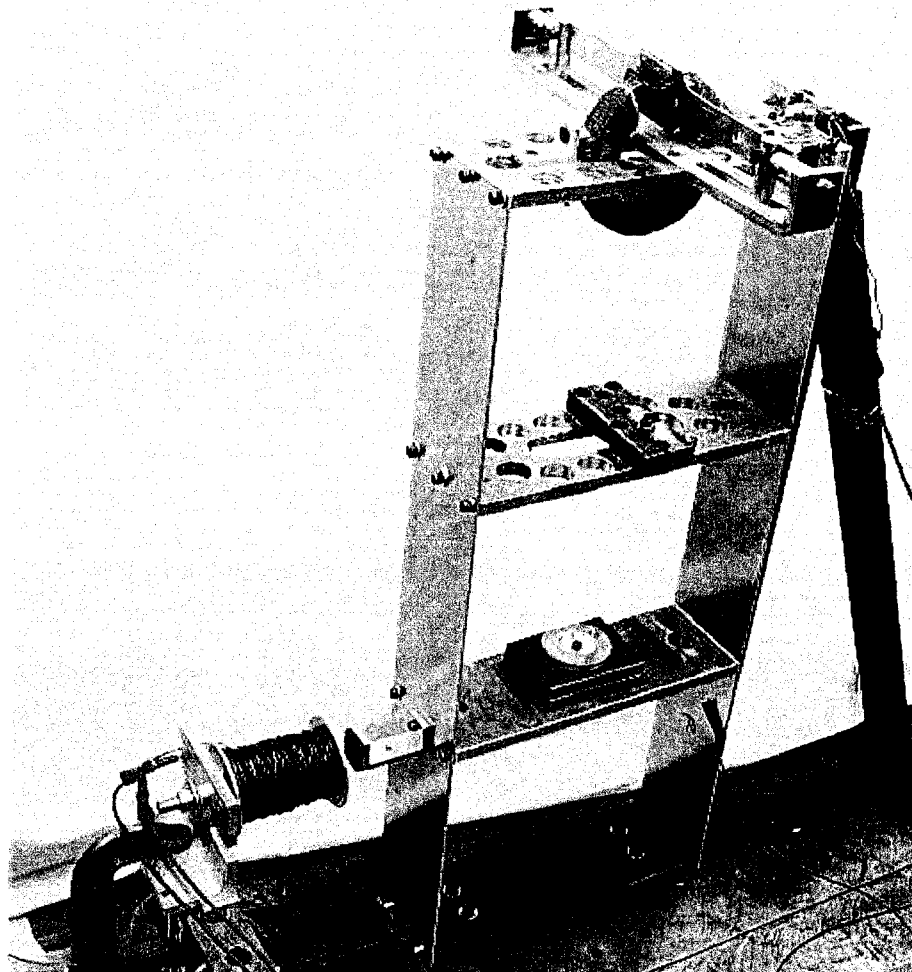


Figure 4.2 Photograph of the experiment model.

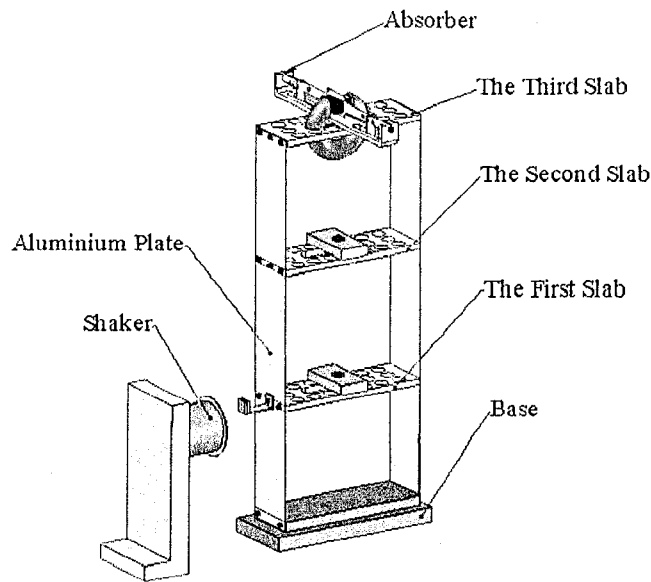


Figure 4.3 CAD drawing of the entire System

The data collection system includes an accelerometer (Brüel & Kjær 4393 V) and a charge amplifier (Brüel & Kjær 2692). The accelerometer is placed on mass  $m_1$  to measure its vibration and the signals are fed into the charge amplifier. The charge amplifier is used to condition the acceleration signals.

The computer control system consists of a Data Acquisition (DAQ) Board (DS1102 dSpace) and a microprocessing computer. The latter, a Pentium III (550 MHz) PC, is used to control the system. The dSPACE ControlDesk provides a graphic user interface with Matlab, Simulink and the DAQ board.

The shaker system includes a power amplifier (Brüel & Kjær 2706) and an electromagnetic coil. An excitation signal generated and controlled by the control system is sent to the power amplifier. A controlled periodic current (DC) is sent from this power amplifier to the electromagnet coil. The interaction between the electromagnet coil and a permanent magnet glued on mass  $m_1$  produces a non-contact excitation force.

## 4.2 Identification of the Parameters of the Primary System

The values of masses  $m_1$ ,  $m_2$ , and  $m_3$  can be easily found to be  $m_1 = 2.73$  kg,  $m_2 = 2.048$  kg, and  $m_3 = 2.635$  kg. In order to find the equivalent stiffnesses  $k_1$ ,  $k_2$ , and  $k_3$ , impact tests were conducted. Figure 4.4 shows a typical Fast Fourier transform (FFT) spectrum of mass  $m_1$ 's response to an impact. The sampling time of the FFT system is 0.001 second.

From Figure 4.4, the three natural frequencies of the primary system were found to be  $f_1 = 6.59$  Hz,  $f_2 = 17.7$  Hz and  $f_3 = 32.15$  Hz.

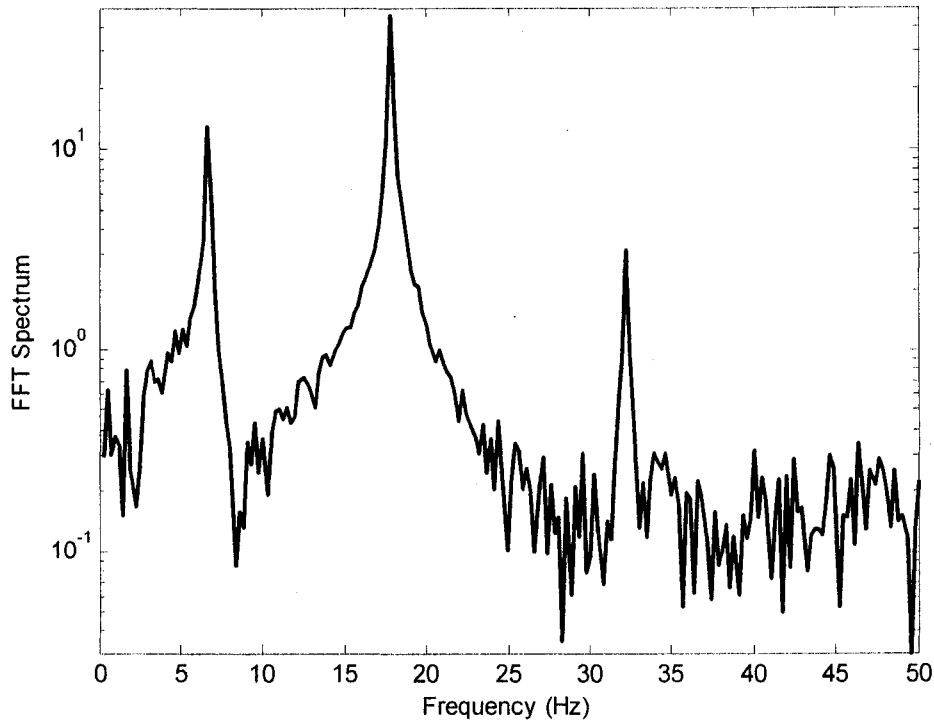


Figure 4.4 FFT spectrum of the response of mass  $m_1$  of the primary system to an impact

In order to find  $k_1$ ,  $k_2$ , and  $k_3$ , a nonlinear optimization was employed. If trial values  $k'_1$ ,  $k'_2$ , and  $k'_3$  are given, estimated natural frequencies can be found by solving the following eigenvalue problem

$$\det[\mathbf{K}' - (2\pi f)^2 \mathbf{M}] = 0, \quad i = 1, 2, 3 \quad (4.1)$$

Solving Equation (4.1) results in three estimated frequencies  $f_i^e, i = 1, 2, 3$  corresponding to the trial values  $k_1', k_2'$  and  $k_3'$ .

$$\mathbf{K}' = \begin{bmatrix} k_1' + k_2' & -k_2' & 0 \\ -k_2' & k_2' + k_3' & -k_3' \\ 0 & -k_3' & k_3' \end{bmatrix}$$

$$\mathbf{M} = \begin{bmatrix} m_1 & 0 & 0 \\ 0 & m_2 & 0 \\ 0 & 0 & m_3 \end{bmatrix} = \begin{bmatrix} 2.73 & 0 & 0 \\ 0 & 2.048 & 0 \\ 0 & 0 & 2.635 \end{bmatrix}$$

A cost function is defined as:

$$J(k_1, k_2, k_3) = \frac{|f_1^e - f_1|}{f_1} + \frac{|f_2^e - f_2|}{f_2} + \frac{|f_3^e - f_3|}{f_3} \quad (4.2)$$

where  $f_i, i = 1, 2, 3$  are the natural frequencies obtained by impact testing.

The problem can be solved by Nelder-Mead sequential complex method [34]-[35]. The sequential simplex method employs geometric properties of the  $n$ -dimensional space. First the cost functions at the  $n+1$  corner points are evaluated to form a simplex. Second a new simplex is formed by replacing the point with the highest function value with a newly selected point. And the process repeats. The iteration continues again until the cost function reaches the convergence criterion.

This problem has 3 variables  $k_1, k_2,$  and  $k_3,$  so 4 corners are required to form a simplex by selecting 4 groups of stiffness. They are presented as:

$$\mathbf{K}_1^0 = [k_{1(1)}^0 \quad k_{2(1)}^0 \quad k_{3(1)}^0]^T, \mathbf{K}_2^0 = [k_{1(2)}^0 \quad k_{2(2)}^0 \quad k_{3(2)}^0]^T, \mathbf{K}_3^0 = [k_{1(3)}^0 \quad k_{2(3)}^0 \quad k_{3(3)}^0]^T \text{ and}$$

$$\mathbf{K}_4^0 = [k_{1(4)}^0 \quad k_{2(4)}^0 \quad k_{3(4)}^0]^T$$

where superscript denotes the number of iteration, the first subscript denotes the stiffness of each spring while the subscript inside the brackets denotes the corner number. The iteration terminates when a certain criteria is satisfied:  $J(k_1, k_2, k_3) < 0.0005$ . Different initial simplex values of  $k_1^i$ ,  $k_2^i$ , and  $k_3^i$  are tried to get the final results, see Table 4.1.

Table 4.1 Initial simplexes vs. the optimal results

Initial simplex	$k_1$	$k_2$	$k_3$	$J$
$\mathbf{K}_1^0 = [20,000 \quad 30,000 \quad 30,000]^T$ $\mathbf{K}_2^0 = [30,000 \quad 20,000 \quad 15,000]^T$ $\mathbf{K}_3^0 = [35,000 \quad 25,000 \quad 35,000]^T$ $\mathbf{K}_4^0 = [30,000 \quad 16,000 \quad 20,000]^T$	17184	35401	20616	$7.923 \times 10^{-9}$
$\mathbf{K}_1^0 = [20,000 \quad 33,000 \quad 30,000]^T$ $\mathbf{K}_2^0 = [32,000 \quad 20,000 \quad 15,000]^T$ $\mathbf{K}_3^0 = [30,000 \quad 25,000 \quad 35,000]^T$ $\mathbf{K}_4^0 = [30,000 \quad 16,000 \quad 20,000]^T$	17183	35401	20616	$4.863 \times 10^{-6}$
$\mathbf{K}_1^0 = [20,000 \quad 23,000 \quad 29,000]^T$ $\mathbf{K}_2^0 = [30,000 \quad 20,000 \quad 45,000]^T$ $\mathbf{K}_3^0 = [35,000 \quad 15,000 \quad 35,000]^T$ $\mathbf{K}_4^0 = [40,000 \quad 19,000 \quad 22,000]^T$	17183	35400	20617	$1.533 \times 10^{-5}$

This method is realized by programming the algorithm in Matlab. The three different groups of the initial values result in almost identical results. The stiffnesses of the primary system were chosen to be  $k_1 = 17183$  N/m,  $k_2 = 35400$  N/m,  $k_3 = 20617$  N/m.



### 4.3 Vibration Suppression Using Manual Adjustment

The EMVA, discussed in Chapter 2, is used as the vibration absorber. The absorber is designed to have a mass of  $m_a = 0.2515$  kg. To suppress the vibration of mass  $m_1$ , the absorber needs to be adjusted to a certain stiffness such that one of the natural frequencies of the subsystem  $f_{si}$  ( $i=1\sim 3$ ) equals the excitation frequency  $f$ . The objective of using the EMVA is to suppress the vibration of  $m_1$  when the system is excited at  $f = f_1$ ,  $f_2$ , or  $f_3$ , i.e., the natural frequencies of the primary system, respectively. Following the analysis in Chapter 3,  $k_{a1} = 457$  N/m will result in  $f_{s1} = f_1$ ,  $k_{a1} = 2785$  N/m will lead to  $f_{s2} = f_2$ , and  $k_{a3} = 8963$  N/m will yield  $f_{s3} = f_3$ . Under these conditions, the natural frequencies of the absorber itself would be  $f_{a1} = 6.747$  Hz,  $f_{a2} = 16.569$  Hz and  $f_{a3} = 29.256$  Hz, respectively.

To find the natural frequency of the absorber, the primary system was fastened to the base by a rigid triangle frame. By impacting the absorber mass and collecting its acceleration signals and applying the FFT, the natural frequency  $f_a$  was found. Experiment showed that when the absorber was set to be  $f_{a1} = 6.747$  Hz, the PM deflected away from the equilibrium position and the absorber spring was so soft that the PM was stuck on one side of the electromagnet. As a result, the absorber cannot be used to attenuate the vibration of mass  $m_1$  when the excitation frequency is equal to the first natural frequency of the primary system. Due to this limitation, this study deals with only the second and third natural frequencies of the primary system. Section 3.5 has shown that the absorber stiffness needed to suppress  $X_1$ , the vibration of mass  $m_1$ , at  $f = f_2$  is significantly different from the one needed to suppress  $X_1$  at  $f = f_3$ . This requires the tunable absorber to have a large tuning range. However, normally an online tunable vibration absorber has a limited tuning range. For example, the EMVA used in [26] and [36] has about 5 Hz tuning range when the current varied from -2.3 A to 2.3 A. For this purpose, the EMVA developed in [26] and [36] was modified to provide both manual

tuning and online tuning, as shown in Figure 2.2 in Section 2.2 of Chapter 2. Figure 4.5 shows the modified EMVA.

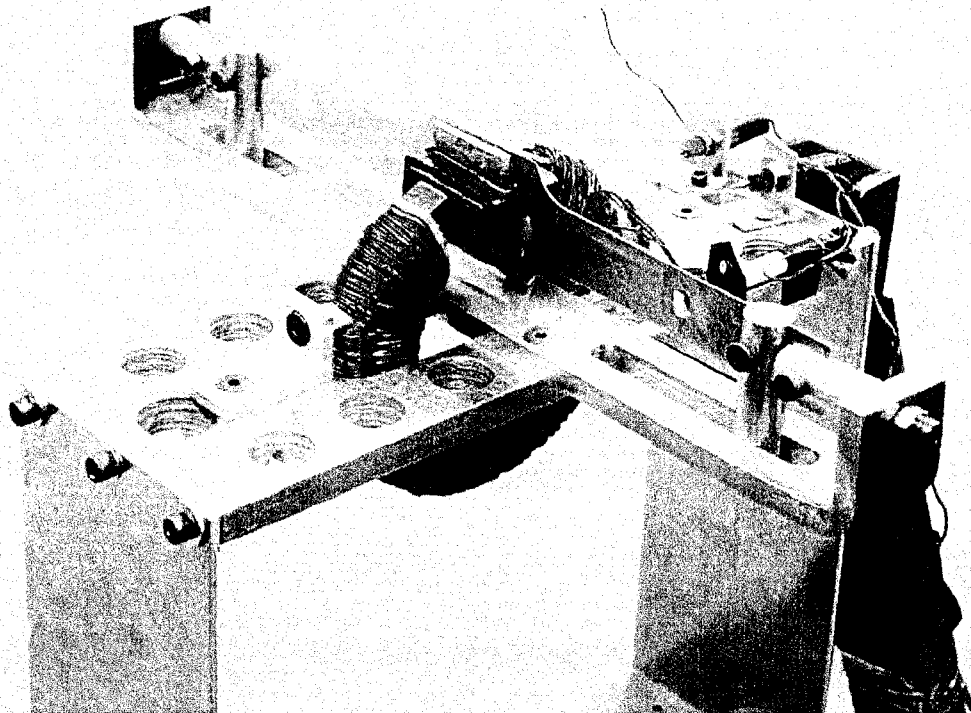


Figure 4.5 Photograph of the modified EMVA

Figure 4.6 and Figure 4.7 show the response of mass  $m_1$  to an impact testing as  $f_{s2} = f_2$  (as  $f_{a2} = 16.569$  Hz) and  $f_{s3} = f_3$  (as  $f_{a3} = 29.256$  Hz). When the absorber was set to a point such that one of the natural frequencies of the subsystem was the same as a natural frequency of the primary system  $f_{si} = f_i$  ( $i = 1 \sim 3$ ), the vibration of mass  $m_1$  was drastically suppressed when the excitation frequency was the same as the subsystem. In other words, mass  $m_1$  was at its lowest magnitude when the anti-resonance frequency was just the same as the excitation frequency. The magnitude increased as the excitation frequency drifted from the anti-resonance. Due to damping between the absorber and other element, the magnitude of mass  $m_1$  could not be zero.

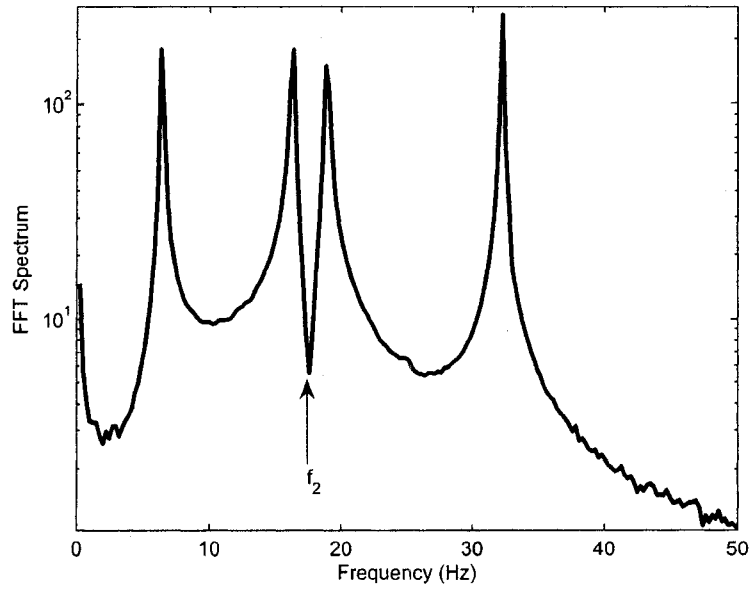


Figure 4.6 FFT spectrum of an impact response of mass  $m_1$  when the EMVA is tuned such that  $f_{s2} = f_2$ .

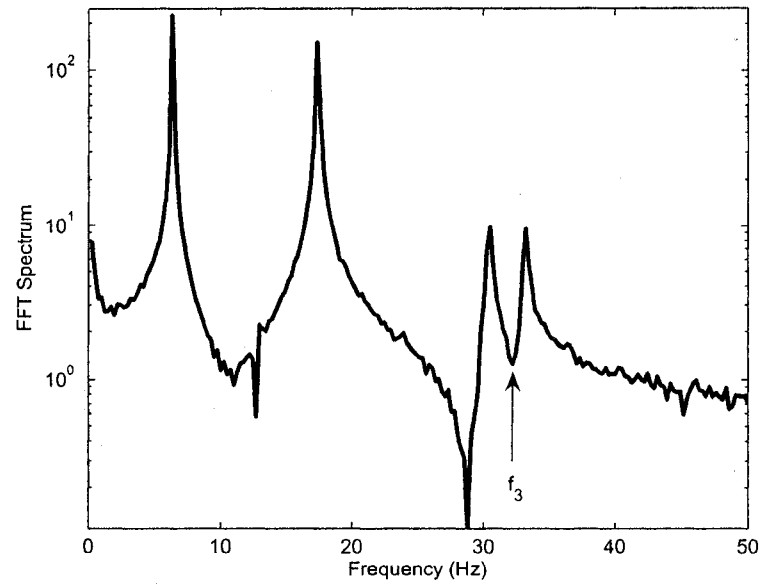


Figure 4.7 FFT spectrum of an impact response of mass  $m_1$  when the EMVA is tuned such that  $f_{s3} = f_3$ .

When the manually preset point of the absorber was at  $f_{a2} = 16.569$  Hz, the second natural frequency of the subsystem was the same as the second natural frequency of the primary system. When the excitation frequency  $f$  was the same as the second natural frequency of the primary system ( $f = f_2$ ), the vibration of mass  $m_1$  was attenuated to minimum. The range of the natural frequency of the absorber varied from  $f_{a2\min} = 13.184$  Hz to  $f_{a2\max} = 20.264$  Hz as the current to the EMVA was changed from  $-2.3$  A to  $2.3$  A. On the other hand, when the excitation frequency  $f$  was around the third natural frequency of the primary system ( $f = f_3$ ), the absorber had to be  $f_{a3} = 29.256$  Hz such that the third natural frequency of the subsystem was the same as the third natural frequency of the primary system. The absorber had to be manually adjusted to be  $f_{a3}$  to suppress the vibration of mass  $m_1$  as the excitation frequency is around the third natural frequency of the primary system.

#### 4.4 The EMVA Calibration

Once the absorber was manually preset close to a required point, the EMVA could be adjusted by changing the current to the electromagnet. To find the relationship between the absorber frequencies  $f_{a2}$ ,  $f_{a3}$  and the current  $I$ , the primary system was fastened to the base by a rigid triangle frame. Impact testing was also used to obtain the natural frequencies  $f_{a2}$  and  $f_{a3}$  when the current was varied. The currents to the electromagnet changed in three stages: stepped up from 0 A to 2.3 A, stepped down to -2.3 A, then stepped up to 2.3 A. For each given current, the absorber mass was tapped and the acceleration signals of the absorber mass were recorded. The natural frequencies  $f_{a2}$  and  $f_{a3}$  were found through applying FFT to the measured response. Figure 4.8 shows the relationship between the absorber frequency  $f_{a2}$  versus the loading and unloading of the coil current and Figure 4.9 shows the relationship between the absorber frequency  $f_{a3}$  versus the loading and unloading of the coil current. The dots represent  $f_{ai}$  and the solid lines represent a third-order polynomial curve-fit of the average results when the current

changed from 0 to 2.3 A, from 2.3 A to -2.3 A, and from -2.3 A to 2.3 A. Because of the nature of the steel core, the results exhibited the characteristics of slight hysteresis. At the preset value  $f_{a2} = 16.569$  Hz, the variation range of  $f_{a2}$  is between 13.184 Hz and 20.020 Hz. As for  $f_{a3} = 29.256$  Hz, the range is between 27.832 Hz and 31.494 Hz when the current varies.

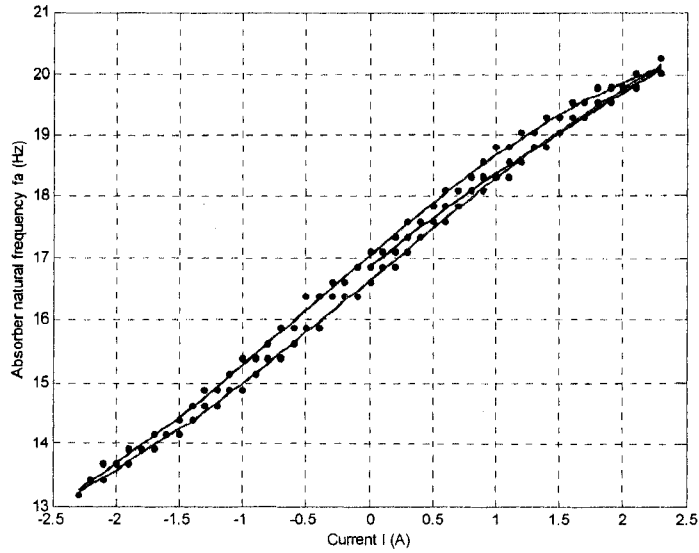


Figure 4.8 Absorber frequency versus the coil current with current loading and current unloading when  $f_a$  was preset to be 16.569 Hz manually.

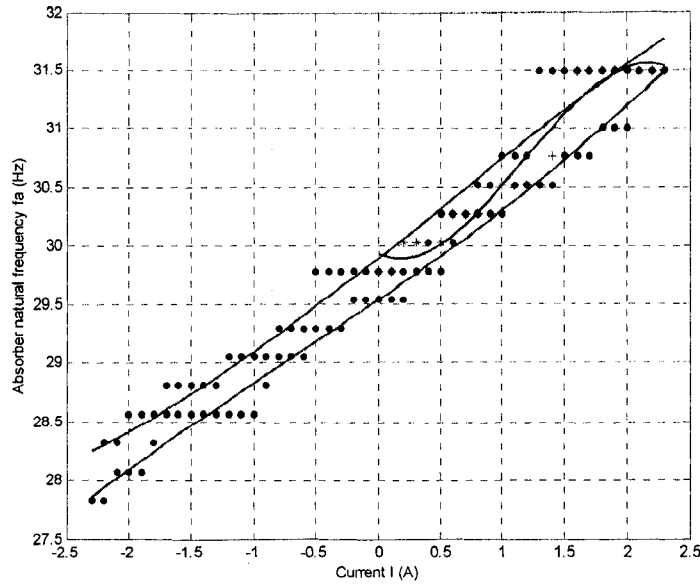


Figure 4.9 Absorber frequency versus the coil current with current loading and current unloading when  $f_a$  was preset to be 29.256 Hz manually.

#### 4.5 The EMVA Performance when Attached to the Primary System

It is desired to know the EMVA adjustment range when it is attached to the primary system and the current of the electromagnet varies. It was done by a sinusoidal sweeping experiment. After the EMVA was manually tuned such that  $f_{a2} = 16.569$  Hz which results in  $f_{s2} = f_2$ , mass  $m_1$  was excited by a sinusoidal force. Then the magnitude of the steady-state response was measured. Next, the excitation frequency was increased by 1 Hz, the process was repeated. As a result the relationship between the magnitude of the steady-state response and the excitation frequency was found. Now, the current of the electromagnet was set to be -2.3 A, the process was repeated. The same procedure was conducted with a current of 2.3 A. Figure 4.10 shows the results. It can be seen that when the current is -2.3 A, the anti-resonance shifts to the left, and when the current is 2.3 A, the anti-resonance shifts to the right. This indicates that the EMVA adjustment range is about 4 Hz (from 15 Hz to 19 Hz) when the current varies from -2.3 A to 2.3 A. The

natural frequency of the absorber  $f_{a2} = 16.569$  Hz is within the range of the anti-resonance.

As the EMVA was manually tuned such that  $f_{a3} = 29.256$  Hz which results in  $f_{s3} = f_3$ , mass  $m_1$  was excited at a sinusoidal force. The same testing was repeated. Figure 4.11 shows the results. It can be seen that when the current is  $-2.3$  A, the anti-resonance shifts to the left, and when the current is  $2.3$  A, the anti-resonance shifts to the right. The EMVA adjustment range is about 2 Hz (from 31 Hz to 33 Hz) when the current varies from  $-2.3$  A to  $2.3$  A. The natural frequency of the absorber  $f_{a3} = 29.256$  Hz is outside of the range of the anti-resonance.

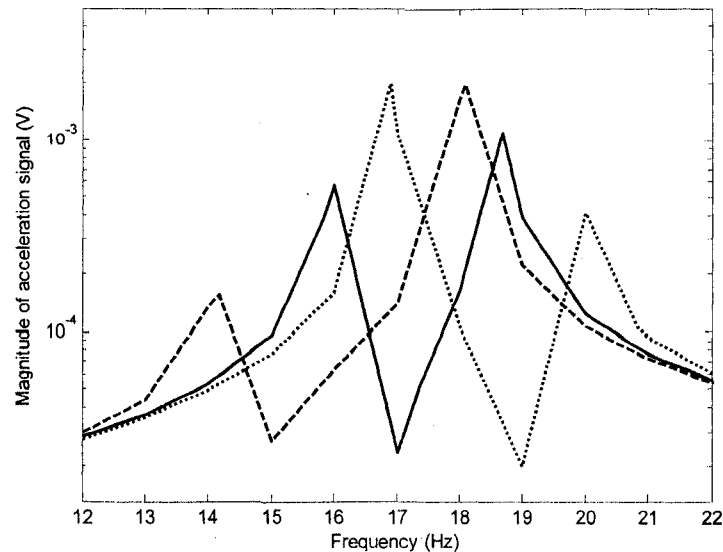


Figure 4.10 Magnitude of the steady-state acceleration signal versus the excitation frequency when the system is excited by a sinusoidal force and  $f_{a2}$  is manually tuned to be  $f_{a2} = 16.569$  Hz: dashed line,  $I = -2.3$  A; solid line,  $I = 0$ ; dotted line,  $I = 2.3$  A.

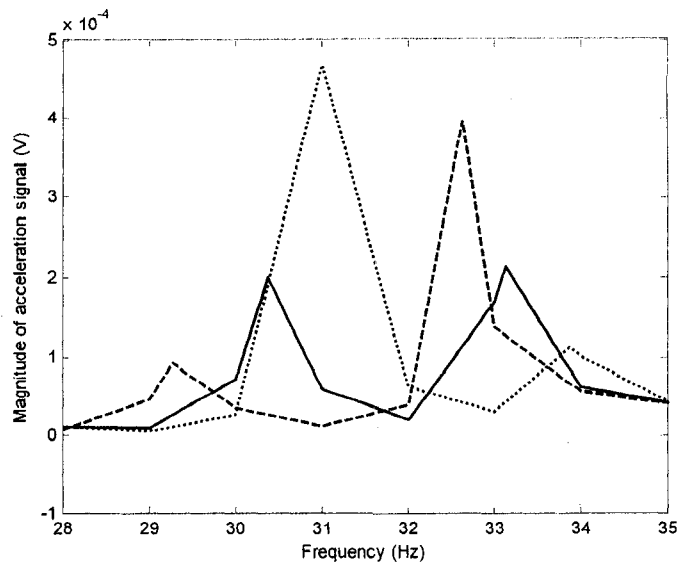


Figure 4.11 Magnitude of the steady-state acceleration signal versus the excitation frequency when the system is excited by a sinusoidal force and  $f_{a3}$  is manually tuned to be  $f_{a2} = 29.256$  Hz: dashed line,  $I = -2.3$  A ; solid line,  $I = 0$  ; dotted line,  $I = 2.3$  A .

#### 4.6 The EMVA Calibration

The EMVA can be manually adjusted and used to suppress the vibration of mass  $m_1$  when a natural frequency of the subsystem equals to the excitation frequency  $f_{si} = f$  ( $i = 2 \sim 3$ ). If the excitation frequency varies, the new system may be in resonance again. The EMVA's capability of on-line tuning offers a solution to ensure the tuning condition in the event that the excitation frequency varies. The objective of the on-line tuning is to adjust the current of the EMVA such that the natural frequency  $f_{s2}$  or  $f_{s3}$  of the subsystem equals the excitation frequency.

To this end, the relationship between the current  $I$  and  $f_{s2}$  or  $f_{s3}$  is needed. In Section 4.4, the relationships between the current  $I$  and  $f_a$  have been found experimentally. Using the average of the values for current stepping up and the values for



current stepping down, a third-order polynomial curve fit equation is obtained. The equation is, for  $f_a = 16.569$  Hz

$$I = -43.204 + 6.7045f_a - 0.3736f_a^2 + 0.0076f_a^3 \quad (4.4)$$

and for  $f_a = 29.256$  Hz

$$I = 309.02 - 35.122f_a + 1.2700f_a^2 - 0.0147f_a^3 \quad (4.5)$$

Figure 4.12 shows as the absorber was at the preset point  $f_a = 16.569$  Hz the relationship between the current  $I$  and the natural frequency of the absorber  $f_a$  by taking into consideration of the average results as the current stepped down from 2.3 A to -2.3 A and stepped up from -2.3 A to 2.3 A. The solid line is obtained by applying the third-order polynomial curve-fit of the average results. The circles represent the average results of the current and the natural frequency of the absorber. Figure 4.13 shows as the absorber was at the preset point  $f_a = 29.256$  Hz the relationship between the current and the natural frequency of the absorber by taking into consideration of the average results as the current stepped down from 2.3 A to -2.3 A and stepped up from -2.3 A to 2.3 A. The solid line is obtained by applying the third-order polynomial curve-fit of the average results. The circles represent the average result of the current and the natural frequency of the absorber.

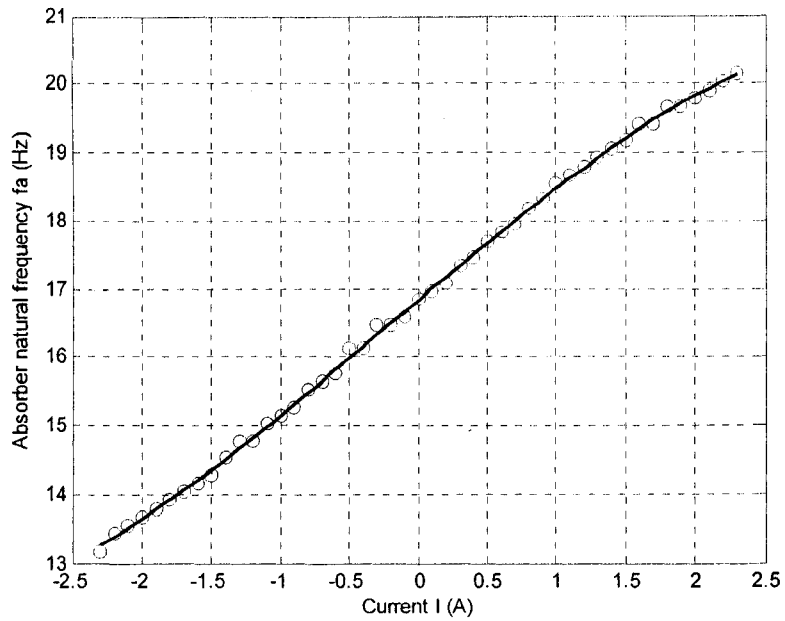


Figure 4.12 Relationship between the current and the natural frequency of the absorber when  $f_a = 16.569$  Hz.

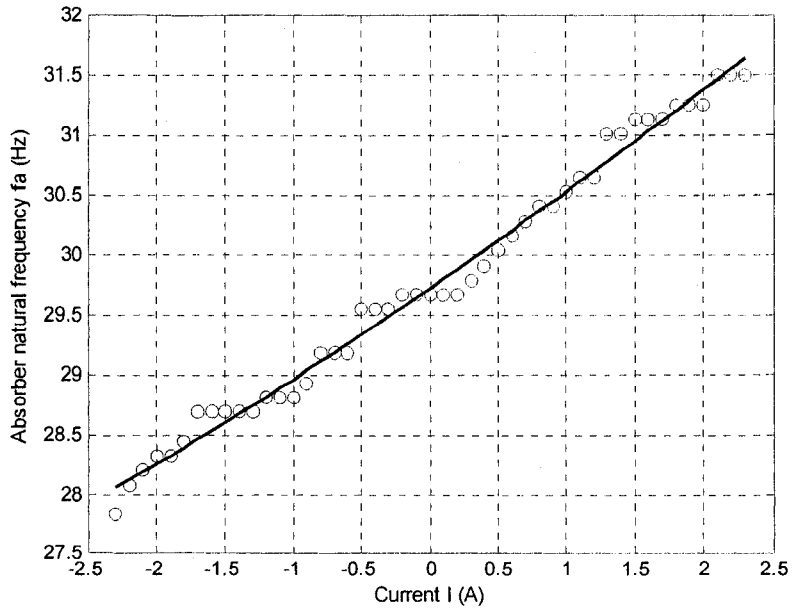


Figure 4.13 Relationship between the current and the natural frequency of the absorber when  $f_a = 29.256$  Hz.

As the relationship between the current  $I$  and the natural frequency of the absorber  $f_a$  is known, the stiffness of the absorber corresponding to current  $I$  is obtained by

$$k_a = (2\pi f_a)^2 m_a \quad (4.6)$$

Then the natural frequencies of the subsystem  $f_{si}$  ( $i = 1 \sim 3$ ) are decided by

$$\det[\mathbf{K}_s - (2\pi f_s)^2 \mathbf{M}_s] = 0 \quad (4.7)$$

where

$$\mathbf{K}_s = \begin{bmatrix} k_2 + k_3 & -k_3 & 0 \\ -k_3 & k_3 + k_a & -k_a \\ 0 & -k_a & k_a \end{bmatrix}$$

$$\mathbf{M}_s = \begin{bmatrix} m_2 & 0 & 0 \\ 0 & m_3 & 0 \\ 0 & 0 & m_a \end{bmatrix}$$

The relationship between the current  $I$  and the natural frequencies of the subsystem is built by applying the third order polynomial curve-fit of the average result of current and  $f_{si}$ . Figure 4.14 shows the third-order polynomial curve-fit of the second natural frequency of the relationship between  $I$  and  $f_{s2}$  when  $f_a$  is manually preset to be  $f_a = 16.569$  Hz. When the current  $I$  changes from -2.3 A to 2.3 A, the second natural frequency  $f_{s2}$  of the subsystem changes from 14.300 Hz to 21.090 Hz. The best fit curve equation is given as

$$I = -58.529 + 8.807 f_{s2} - 0.4686 f_{s2}^2 + 0.0089 f_{s2}^3 \quad (4.8)$$

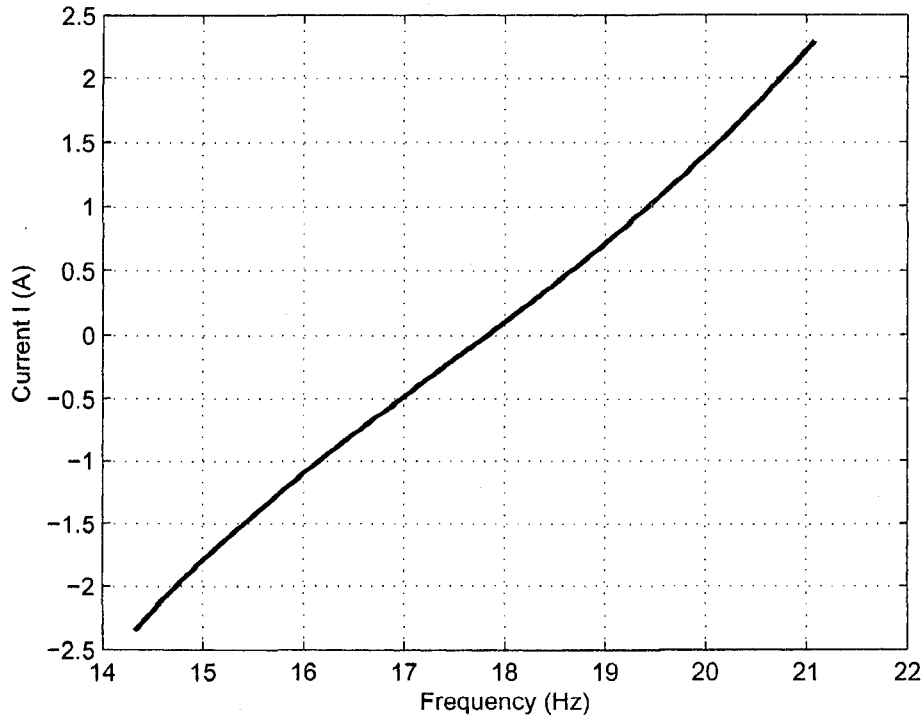


Figure 4.14 The best-fit curve of the second natural frequency of the subsystem and the current of the electromagnet

Figure 4.15 shows the third-order polynomial curve-fit of the relationship between  $I$  and  $f_{s3}$  when  $f_a$  is manually preset to be  $f_a = 29.256$  Hz. When the current changes from  $-2.3$  A to  $2.3$  A, the third natural frequency  $f_{s3}$  of the subsystem changes from  $30.350$  Hz to  $33.500$  Hz. The best fit curve equation is given as

$$I = -339.36 + 25.779f_{s3} - 0.6593f_{s3}^2 + 0.0058f_{s3}^3 \quad (4.9)$$

It is noted that as the natural frequency of the absorber  $f_a = 16.569$  Hz is within the adjusting range of the anti-resonance of the entire system, but the natural frequency of the absorber  $f_a = 29.256$  Hz is not in that of the entire system.

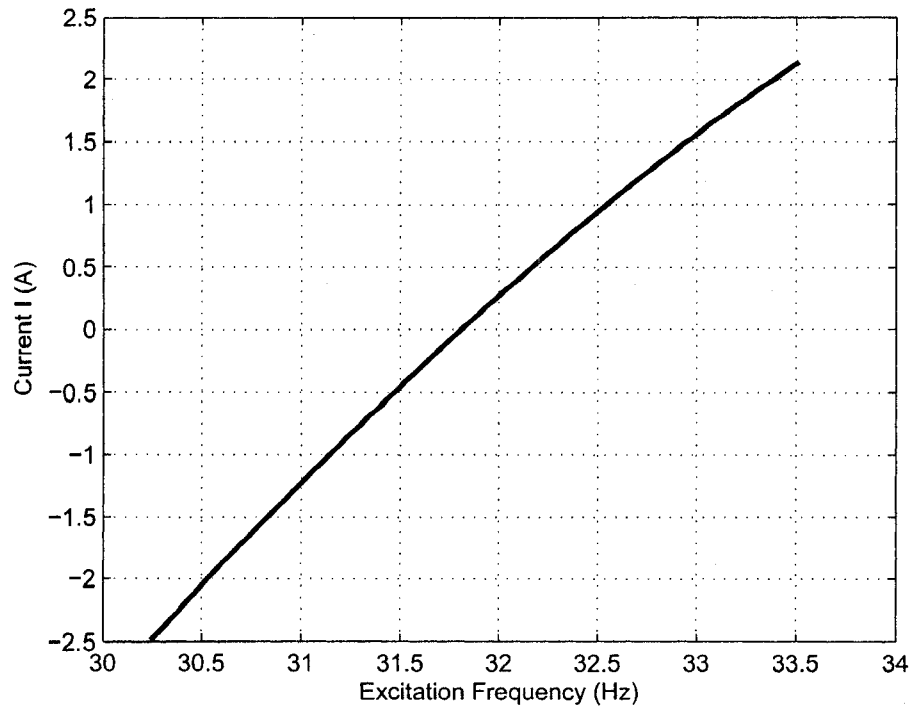


Figure 4.15 The best-fit curve of the third natural frequency of the subsystem and the current of the electromagnet

## 4.7 Experimental Results

Three control methods were tested experimentally. The first one is a FFT-based method. The second one is the FFT-based plus fine tuning. The third one is a response root-mean-squares (RMS) based method. Each method and the results will be presented as follows.

### 4.7.1 Simulink Model for the FFT-based Tuning Method

The FFT-based method applies the FFT to the measured response of mass  $m_1$  to find the frequency of the highest peak in the FFT spectrum. This frequency is then considered

to be the excitation frequency and used in Equation (4.8) or (4.9) to determine the desired current in order to tune the EMVA.

Figure 4.16 shows a Simulink model for the FFT-based method. The Excitation Subsystem generates a sinusoidal signal. The signal is sent to a digital to analog channel, DAC #1. The analog signal from DAC #1 is fed into a power amplifier to drive the shaker. The acceleration signal measured by an accelerometer is sampled at an analog to digital channel ADC #1. An S-function Buffer is used to collect a specified length of data. In this case the data length used is 2048. The sampling time used is 0.001 second. Zero-Order Hold 2 executes every 2.048 seconds. FFT block, an S-function executing every 2.048 seconds, outputs frequency of the response. The Compute\_current block calculates the output current either by equation (4.8) or (4.9) according to the input frequency. Saturation limits the output current to the DS1102DAC such that the current applied to the EMVA does not exceed  $\pm 2.3$  A, which is the maximum allowed current to the coil of the EMVA.

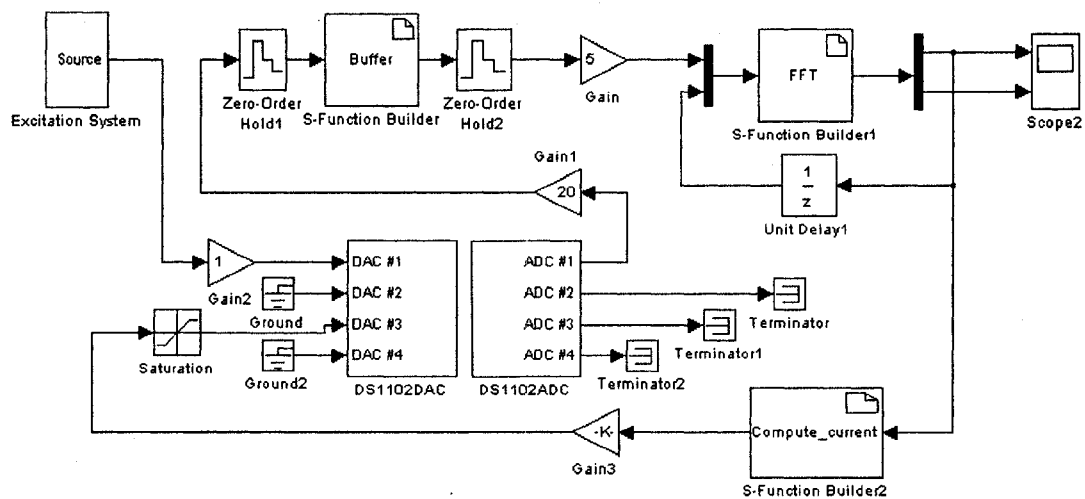


Figure 4.16 Simulink model for the FFT-based tuning.

When experiment conditions change, the relationship between the current and the stiffness of the system will not be the same, such as variation of the coil resistance of the EMVA due to different temperature. Under these conditions, the relationship built in equations (4.8) and (4.9) may not be accurate for the vibration attenuation. It is necessary

to use an adjusting controller to cope with the variable conditions. Figure 4.17 shows the FFT-based plus fine tuning model. By adding a Fine\_control block between Compute\_current block and Saturation block in Figure 4.16, this new model is formed. The Fine\_control block, an S-function, is to adjust the current in fine steps. The block considers the measured frequency and root mean squared value (RMS). The RMS value is calculated as

$$rms = \sqrt{\frac{\sum_{i=1}^N (x_i)^2}{N}}$$

where  $N$  is the number of measured points in the sampled period, or 2.048 second. When the RMS value exceeds a prescribed threshold value, the current is adjusted according to the FFT-based method. When the RMS value is below the threshold value, the current is adjusted by the following way. The present RMS value is compared with the previous RMS value. If the RMS value is increased due to increasing (or decreasing) the current, the current is decreased (or increased) by a prescribed increment. If the RMS value is decreased due to decreasing (or increasing) the current, the current is decreased (or increased) by the prescribed increment.

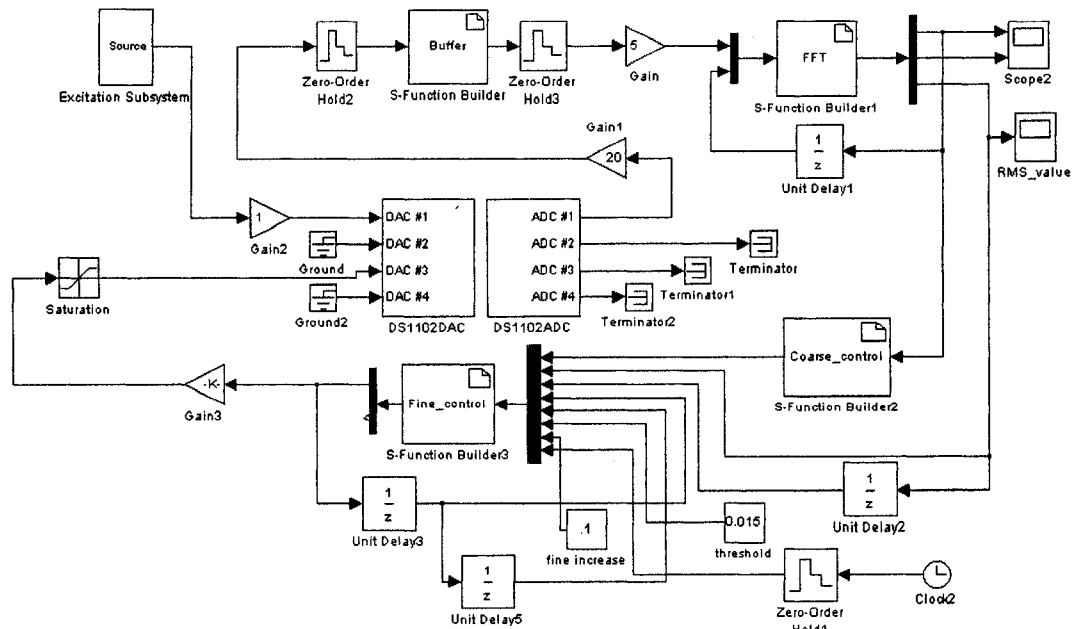


Figure 4.17 Simulink model for the FFT-based plus fine tuning method

Figure 4.18 shows the Simulink model developed for the RMS auto-tuning method. The signal measured by the accelerometer is discretized by Zero-Order Hold 2 with a sampling time of 0.001 second. The S-function Buffer is used to collect a length of 512 data. Zero-Order Hold 3 executes every 0.512 seconds. RMS block, an S-function executing every 0.512 seconds, outputs RMS of the acceleration signals. The RMS\_analyzer block analyzes the RMS value and its change direction, and outputs current according to these two factors. If the value of RMS is smaller than the threshold, the output current remains unchanged. If the value of RMS exceeds the threshold, the output current is changed according to the value of RMS change. If the value of RMS increases (or decreases) due to decreasing (or increasing) the current, the current is increased (or decreased) by a prescribed value. If the value of RMS decreases (or increases) due to increasing (or decreasing) the current, the current is decreased (or increased) by a prescribed value.



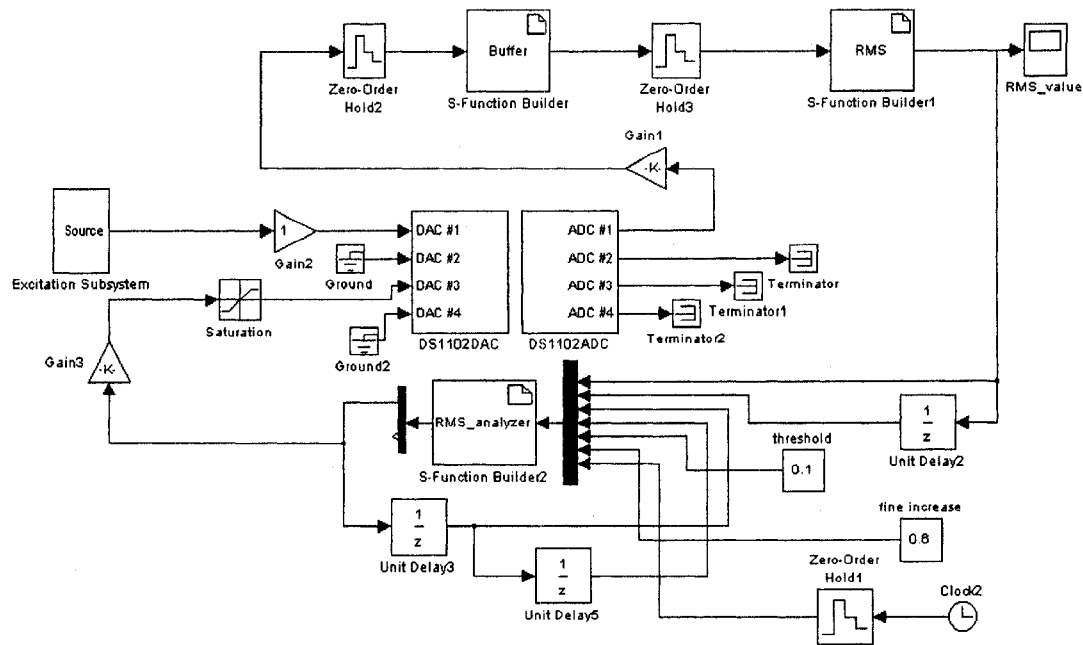


Figure 4.18 Simulink model for the RMS-based tuning method

Two testing scenarios were devised to test the effectiveness of the EMVA in dealing with variable excitation frequencies. The following sections describe the testing scenarios and results.

#### 4.7.2 Testing Scenario One

In scenario one, the EMVA was manually preset such that the second natural frequency of the subsystem equals the second natural frequency of the primary system, i.e.,  $f_{s2} = f_2 = 17.700$  Hz or  $f_a = 16.569$  Hz. The excitation frequency was changed in three steps. First, the excitation frequency was set to be  $f = 17.700$  Hz. After 6.7 seconds, the excitation frequency was switched to be  $f = 18.860$  Hz which was close to the third natural frequency of the entire system. At around  $t = 16.7$  second, the excitation frequency was changed to be  $f = 16.240$  Hz which was close to the second natural frequency of the entire system. If the EMVA is used as a passive vibration absorber, the system will be at the anti-resonance during the first 6.7 seconds, at the resonance at the

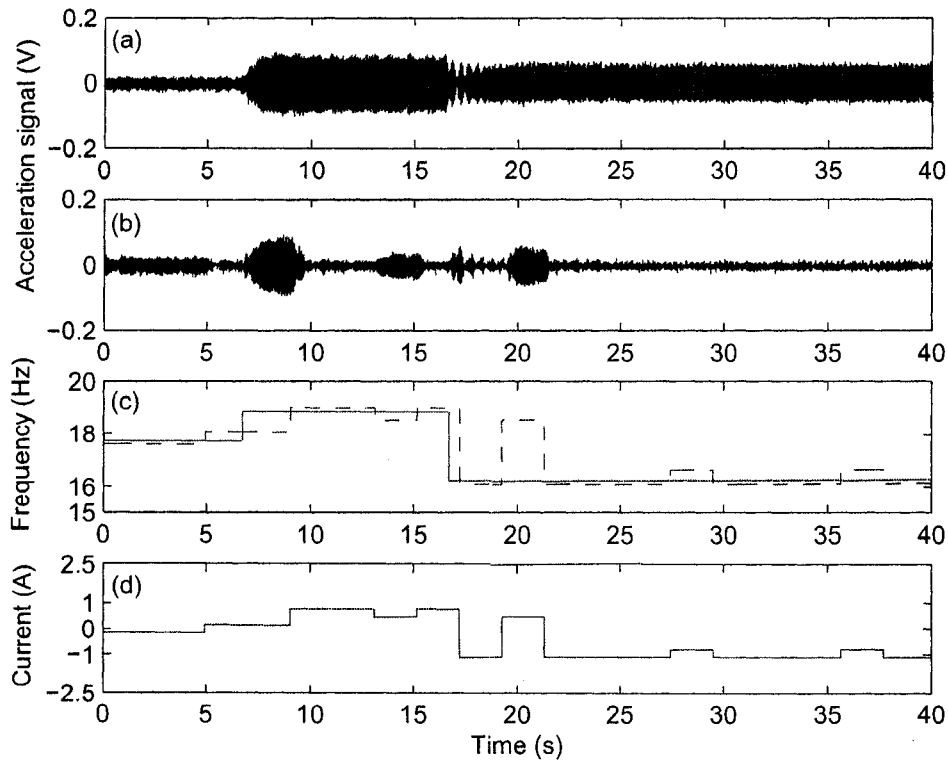


Figure 4.19 Experimental results using the FFT-based method when the absorber was manually preset at  $f_{a2} = 16.569$  Hz: (a) response of mass  $m_1$  without control, (b) response of mass  $m_1$  with control, (c) the frequencies: solid line, excitation frequency; dashed line, estimated frequency, (d) the EMVA current.

Figure 4.20 shows the results when the FFT-based plus fine tuning with a small threshold was applied. The threshold was 0.005 and the fine current increment was 0.2. Figure 4.20 (a) shows the response of mass  $m_1$  without control. Figure 4.20 (b) shows the response of mass  $m_1$  when the EMVA was activated. Figure 4.20 (c) shows the variation of the excitation frequency and the estimated excitation frequency. Figure 4.20 (d) shows the current to the EMVA. As shown in the figure, the response was small and the current was low during the first 6.7 seconds because the system was at the anti-resonance state. After the system was set into the resonance at  $t = 6.7$  second, the response was increased. It took 2.048 seconds for the control system to activate the EMVA. After the EMVA was

tuned so that  $f_{s2} = f_2$ , the response was reduced. At  $t = 16.7$  second, the excitation frequency varied. Once again it took 2.048 seconds for the control system to respond to this change. Based on the identified excitation frequency, the EMVA current was adjusted to the desired one so that the response was suppressed again. As the RMS value was always greater than the threshold, the fine tuning was not activated and the tuning was determined by the FFT-based method.

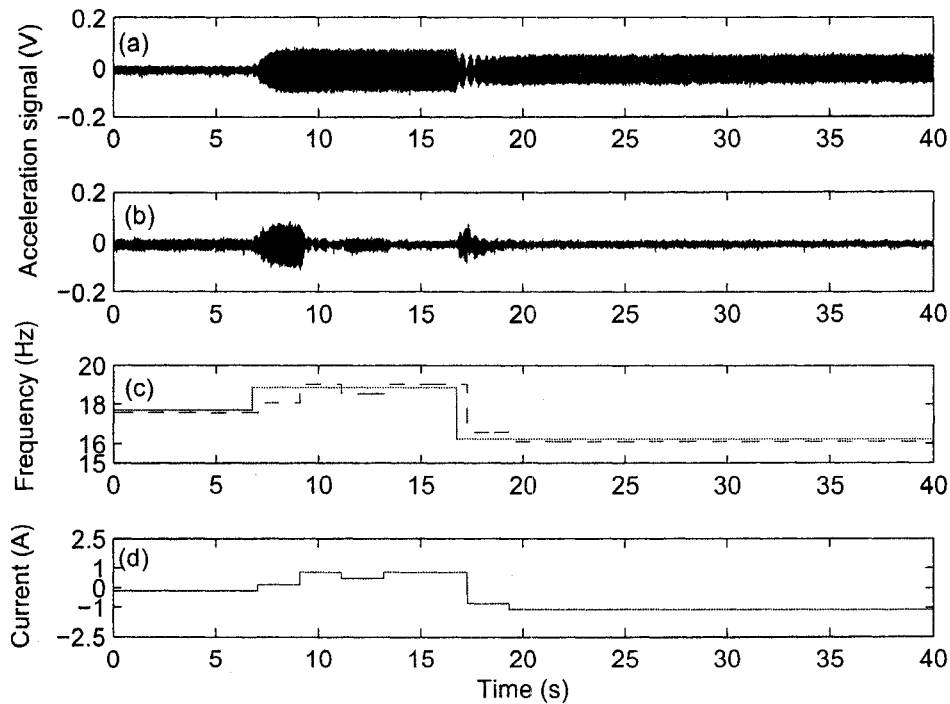


Figure 4.20 Experimental results using the FFT-based plus fine tuning with a small threshold when the absorber was manually preset at  $f_{a2} = 16.569$  Hz: (a) response of mass  $m_1$  without control, (b) response of mass  $m_1$  with control, (c) the frequencies: solid line, excitation frequency; dashed line, estimated frequency, (d) the EMVA current.

Figure 4.21 shows the results when the FFT-based plus fine tuning when a proper threshold was used. The threshold was set to be 0.051 and the fine current increment was 0.2. Figure 4.21 (a) shows the response of mass  $m_1$  without control. Figure 4.21 (b)

shows the response of mass  $m_1$  when the EMVA was activated. Figure 4.21 (c) shows the variation of the excitation frequency and the estimated excitation frequency. Figure 4.21 (d) shows the current to the EMVA. As shown in the figure, the response was small and the current was low during the first 6.7 seconds because the system was at the anti-resonance state. After the system was set into the resonance at  $t=6.7$  second, the response was increased. It took 2.048 seconds for the control system to activate the EMVA. After the EMVA was tuned so that  $f_{s2} = f_2$ , the response was reduced. At  $t=16.7$  second, the excitation frequency varied. Once again it took 2.048 seconds for the control system to respond to this change. Based on the identified excitation frequency, the EMVA current was adjusted to the desired one to suppress the vibration. The fine tuning changed the current in a small step to reduce the vibration further.

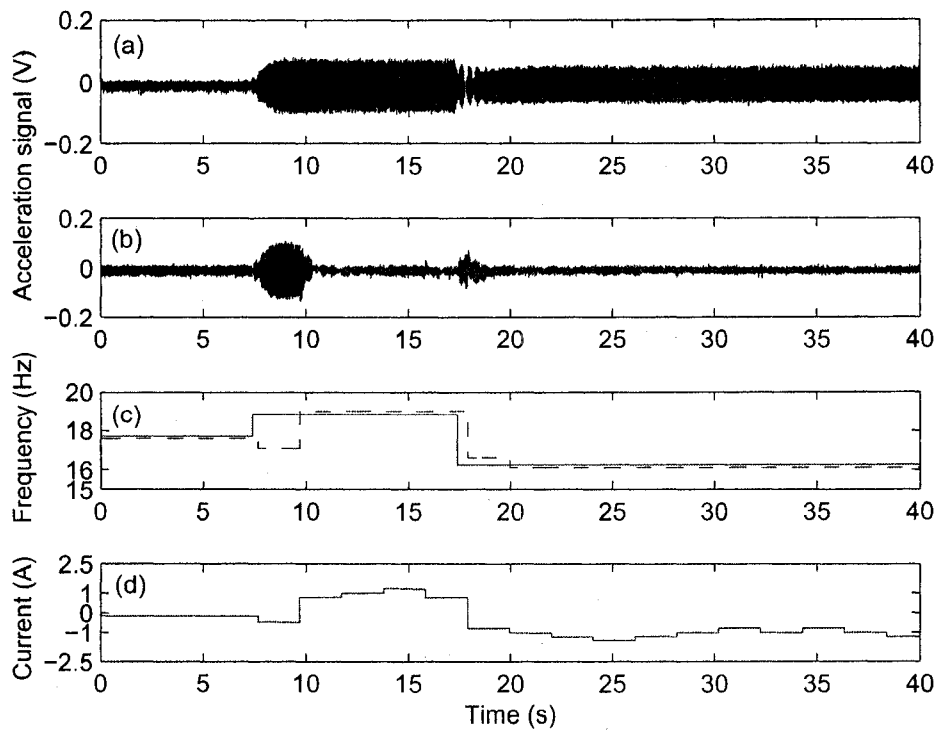


Figure 4.21 Experimental results using the FFT-based plus fine tuning with a proper threshold when the absorber was manually preset at  $f_{a2} = 16.569$  Hz: (a) response of mass  $m_1$  without control, (b) response of mass  $m_1$  with control, (c) the frequencies: solid line, excitation frequency; dashed line, estimated frequency, (d) the EMVA current.

Figure 4.22 shows the results when the FFT-based plus fine tuning with a large threshold was applied. The threshold was set to be 0.5 and the fine current increment was 0.8. Figure 4.22 (a) shows the response of mass  $m_1$  without control. Figure 4.22 (b) shows the response of mass  $m_1$  when the EMVA was activated. Figure 4.22 (c) shows the variation of the excitation frequency and the estimated excitation frequency. Figure 4.22 (d) shows the current to the EMVA. As shown in the figure, the response was small and the current was low during the first 6.7 seconds because the system was at the anti-resonance state. After 2.048 seconds, the fine tuning began to adjust the EMVA by increasing the current and the action caused the increase of the response. Then the fine tuning adjusted the EMVA back to zero current after sensing the increase of the response. The fine tuning continued increasing the current in another direction and changed the current to negative. As the system was set into the resonance at  $t = 6.7$  second, the response was increased. It took 2.048 seconds for the control system to re-activate the EMVA. The current changed in the direction of decreasing the response. In this situation, because the RMS value was always smaller than the threshold, the EMVA current was adjusted according to the fine tuning scheme only.

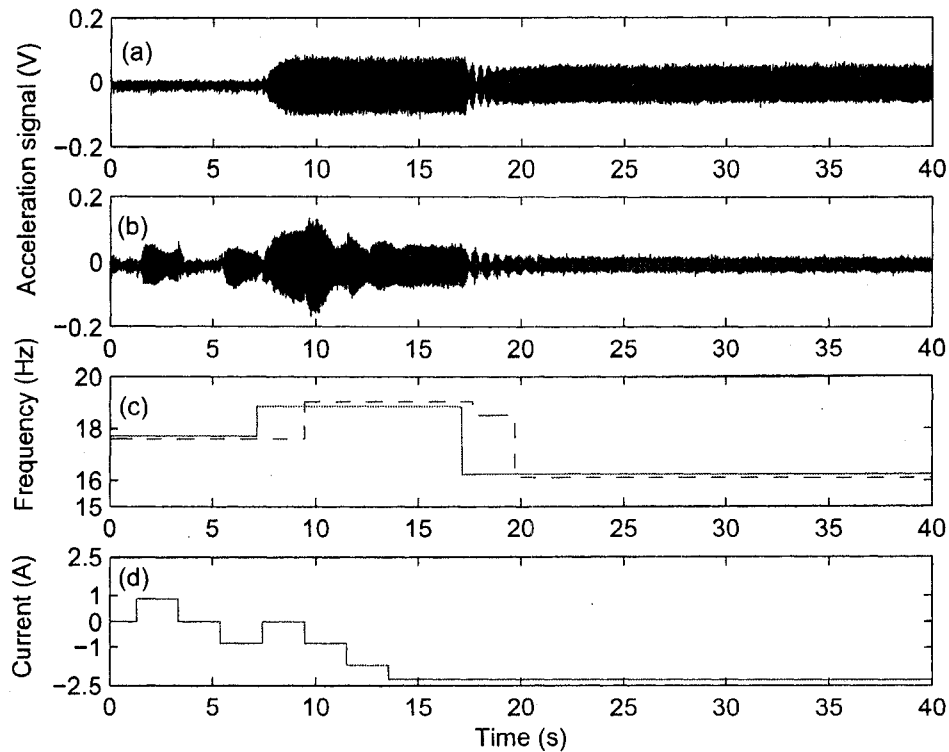


Figure 4.22 Experimental results using the FFT-based plus fine tuning with a larger threshold when the absorber was manually preset at  $f_{a2} = 16.569$  Hz: (a) response of mass  $m_1$  without control, (b) response of mass  $m_1$  with control, (c) the frequencies: solid line, excitation frequency; dashed line, estimated frequency, (d) the EMVA current.

Figure 4.23 shows the results when the RMS-based method was applied. The threshold was 0.051 and the fine increase was 0.5. Figure 4.23 (a) shows the response of mass  $m_1$  without control. Figure 4.23 (b) shows the response of mass  $m_1$  when the EMVA was activated. Figure 4.23 (c) shows the variation of the excitation frequency. Figure 4.23 (d) shows the current to the EMVA. As shown in the figure, the response was small and the current was around zero at first because the system was at the anti-resonance state. After the system was set into the resonance at  $t = 6.7$  second, the value of RMS was increased significantly. It took 0.512 second for the control system to react and the current changed suddenly. Then the response was reduced gradually. At  $t = 16.7$  second, the response was increased again. It took 0.512 second for the control system to respond to this change.

Based on the value of RMS, the EMVA current was decreased to suppress the response again. The RMS-based method took longer time to reach the final adjustment than the other two methods.

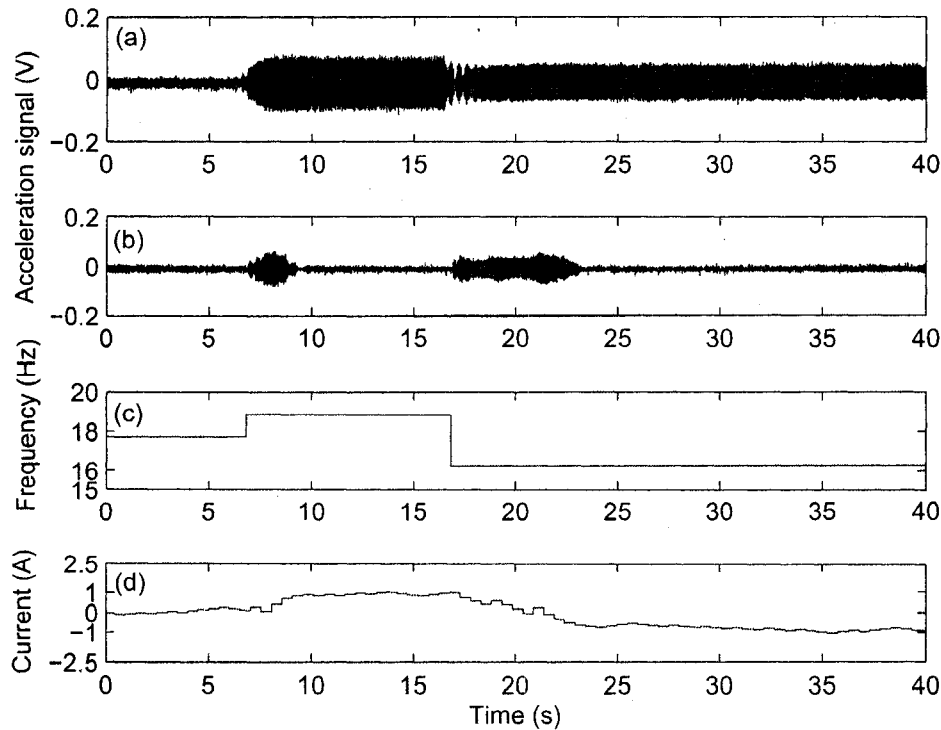


Figure 4.23 Experimental results using the RMS-based method when the absorber was manually preset at  $f_{a2} = 16.569$  Hz: (a) response of mass  $m_1$  without control, (b) response of mass  $m_1$  with control, (c) the excitation frequency, (d) the EMVA current.

### 4.7.3 Testing Scenario Two

In scenario two, the EMVA was manually preset such that the third natural frequency of the subsystem equals the third natural frequency of the primary system, i.e.,  $f_{s3} = f_3 = 31.740$  Hz or  $f_a = 29.256$  Hz. The excitation frequency was changed in three steps. First, the excitation frequency was set to be  $f = 31.740$  Hz. After 6.7 seconds, the excitation frequency was switched to be  $f = 33.450$  Hz which was close to the fourth

natural frequency of the entire system. At around  $t=16.7$  second, the excitation frequency was changed to be  $f=30.280$  Hz which was close to the third natural frequency of the entire system. If the EMVA is used as a passive vibration absorber, the system will be at the anti-resonance during the first 6.7 seconds, at the resonance at the fourth natural frequency during the next 10 seconds, and at the resonance at the third natural frequency during the rest of the time.

Figure 4.24 shows the results when the FFT-based method. Figure 4.24 (a) shows the response of mass  $m_1$  without control. Figure 4.24 (b) shows the response of mass  $m_1$  when the EMVA was activated. Figure 4.24 (c) shows the variation of the excitation frequency and the estimated excitation frequency. Figure 4.24 (d) shows the current to the EMVA. As shown in the figure, the response was small and the current was low at first. But due to the change of the measured frequency, the current changed. After the system was set into the resonance at  $t=6.7$  second, the response was increased significantly. It took 2.048 seconds for the control system to activate the EMVA. After the EMVA was tuned so that  $f_{s3} = f_3$ , the response was reduced. At  $t=16.7$  second, it took 2.048 seconds for the control system to respond to this change. The change of current also caused the system to change and this transient response made the current changed again. Based on the identified excitation frequency, the EMVA current was adjusted to the desired one so that the response was suppressed again.



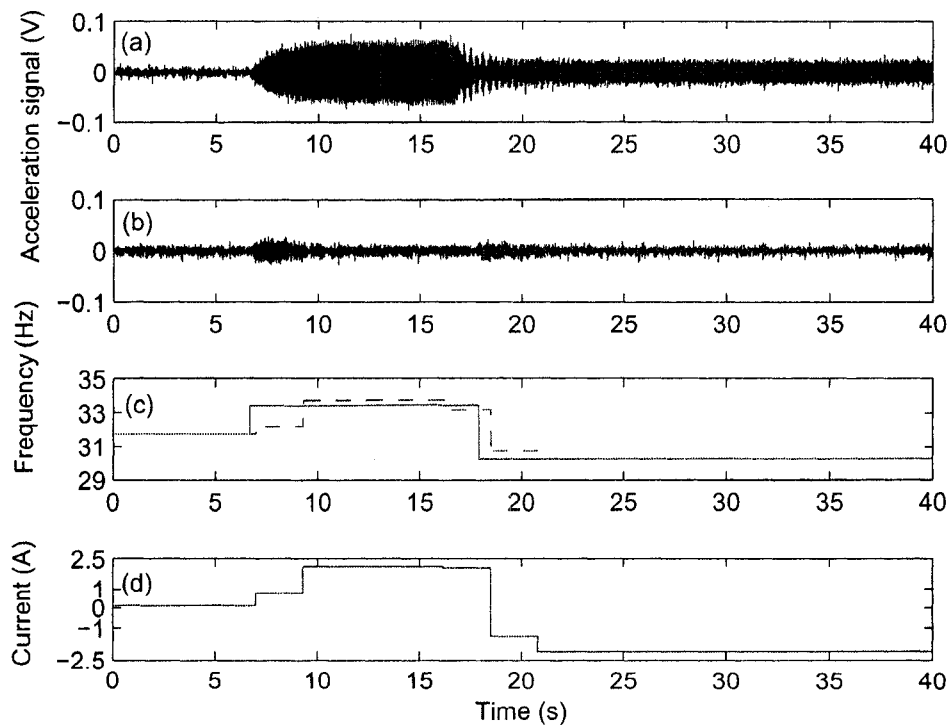


Figure 4.24 Experimental results using the FFT-based method when the absorber was manually preset at  $f_{a3} = 29.256$  Hz: (a) response of mass  $m_1$  without control, (b) response of mass  $m_1$  with control, (c) the frequencies: solid line, excitation frequency; dashed line, estimated frequency, (d) the EMVA current.

Figure 4.25 shows the results when the FFT-based plus fine tuning with a small threshold was applied. The threshold was 0.005 and the fine increase was 0.2. Figure 4.25 (a) shows the response of mass  $m_1$  without auto-tuning. Figure 4.25 (b) shows the response of mass  $m_1$  when the EMVA was activated. Figure 4.25 (c) shows the variation of the excitation frequency and the estimated excitation frequency. Figure 4.25 (d) shows the current to the EMVA. As shown in the figure, the response was small and the current was around zero at first. After the system was set into the resonance at  $t = 6.7$  second, the response was increased. It took 2.048 seconds for the control system to activate the EMVA. After the EMVA was tuned so that  $f_{s3} = f_3$ , the response was reduced. At

$t = 16.7$  second, the excitation frequency varied. Once again it took 2.048 seconds for the control system to respond to this change. Based on the identified excitation frequency, the EMVA current was adjusted to the desired one so that the response was suppressed again. As the RMS value was always greater than the threshold, the fine tuning did not work. The tuning was determined by the FFT-based method.

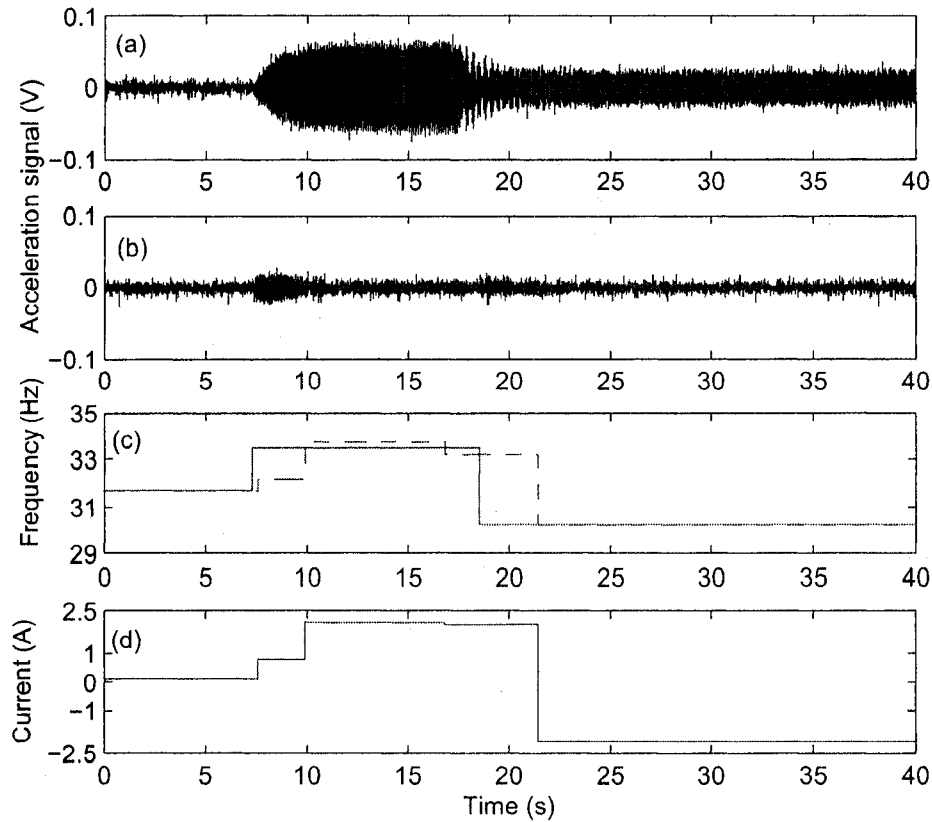


Figure 4.25 Experimental results using the FFT-based plus fine tuning with a small threshold when the absorber was manually preset at  $f_{a3} = 29.256$  Hz: (a) response of mass  $m_1$  without control, (b) response of mass  $m_1$  with control, (c) the frequencies: solid line, excitation frequency; dashed line, estimated frequency, (d) the EMVA current.

Figure 4.26 shows the results when the FFT-based plus fine tuning when a proper threshold was applied. The threshold was set to be 0.051 and the fine current increment was 0.2. Figure 4.26 (a) shows the response of mass  $m_1$  without control. Figure 4.26 (b)

shows the response of mass  $m_1$  when the EMVA was activated. Figure 4.26 (c) shows the variation of the excitation frequency and the estimated excitation frequency. Figure 4.26 (d) shows the current to the EMVA. As shown in the figure, the response was small and the current was low during the first 6.7 seconds because the system was at the anti-resonance state. The current was adjusted around  $t = 2.048$  second by the fine tuning to decrease the response. After the system was set into the resonance at  $t = 6.7$  second, the response was increased. It took 2.048 seconds for the control system to activate the EMVA. After the EMVA was tuned so that  $f_{s3} = f_3$ , the response was reduced. At  $t = 16.7$  second, the excitation frequency varied. Once again it took 2.048 seconds for the control system to respond to this change. Based on the identified excitation frequency, the EMVA current was adjusted to the desired one to suppress the vibration. The fine tuning then changed the current in a small step to reduce the vibration further.

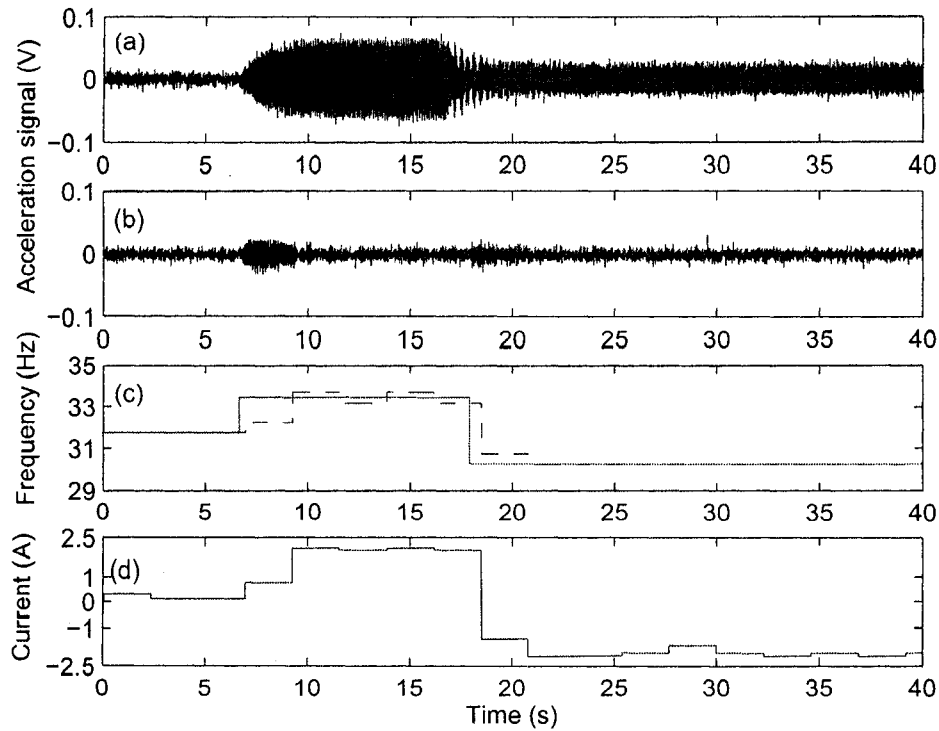


Figure 4.26 Experimental results using the FFT-based plus fine tuning with a proper threshold when the absorber was manually preset at  $f_{a3} = 29.256$  Hz: (a) response of mass  $m_1$  without control, (b) response of mass  $m_1$  with control, (c) the frequencies: solid line, excitation frequency; dashed line, estimated frequency, (d) the EMVA current.

Figure 4.27 shows the results when the FFT-based plus fine tuning with a large threshold was applied. The threshold was set to be 0.5 and the fine current increment was 1. Figure 4.27 (a) shows the response of mass  $m_1$  without control. Figure 4.27 (b) shows the response of mass  $m_1$  when the EMVA was activated. Figure 4.27 (c) shows the variation of the excitation frequency and the estimated excitation frequency. Figure 4.27 (d) shows the current to the EMVA. As shown in the figure, the response was small and the current was low at first because the system was at the anti-resonance state. At  $t=1$  second, the fine tuning began to adjust the EMVA by increasing the current and the response increased. Then the fine tuning adjusted the current after sensing the increase of RMS. The current changed in another direction and returned the current to zero. As the

system was set into the resonance at  $t = 6.7$  second, the response was increased. It took 2.048 seconds for the control system to re-activate the EMVA. The current changed when tracking the direction of decreasing the value of RMS. At  $t = 16.7$  second, the excitation frequency changed again. As the current changed in the direction to decrease the response, the current increased further. In this situation, because the RMS value was always smaller than the threshold, the EMVA current was adjusted by the fine tuning only.

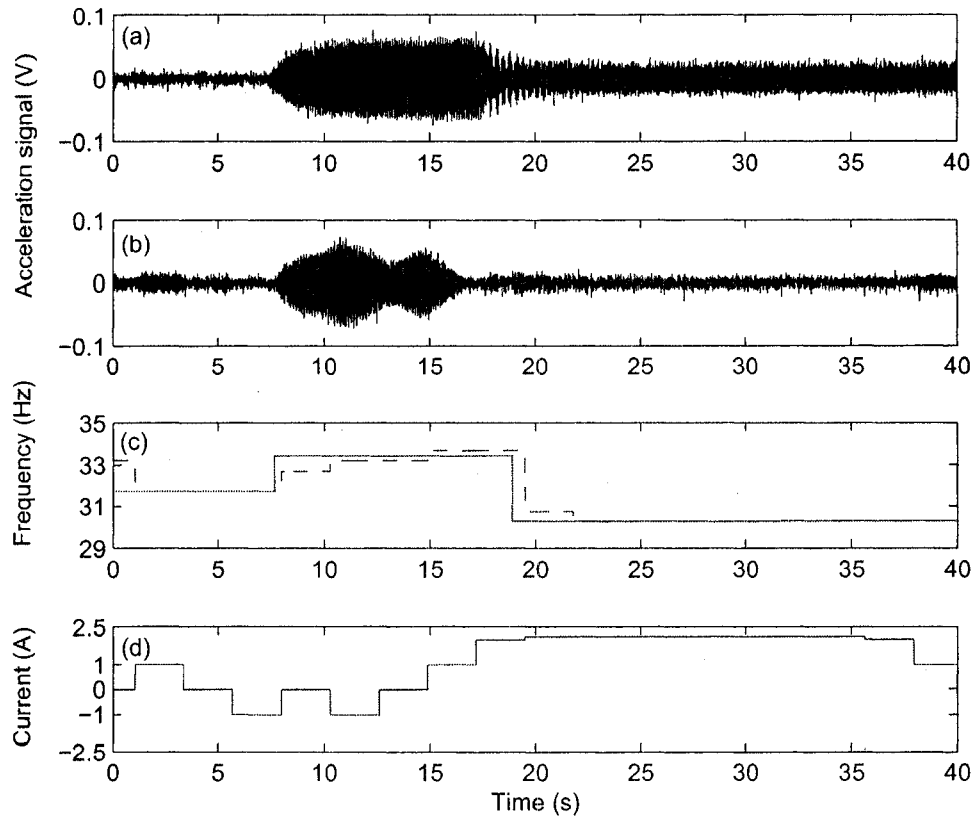


Figure 4.27 Experimental results using the FFT-based plus fine tuning with a large threshold when the absorber was manually preset at  $f_{a3} = 29.256$  Hz: (a) response of mass  $m_1$  without control, (b) response of mass  $m_1$  with control, (c) the frequencies: solid line, excitation frequency; dashed line, estimated frequency, (d) the EMVA current.

Figure 4.28 shows the results when the RMS-based method was applied. The threshold was 0.005 and the fine increase was 0.3. Figure 4.28 (a) shows the response of mass  $m_1$  without auto-tuning. Figure 4.28 (b) shows the response of mass  $m_1$  when the EMVA was activated. Figure 4.28 (c) shows the variation of the excitation frequency. Figure 4.28 (d) shows the current to the EMVA. As shown in the figure, the response was small and the current was around zero during the first 6.7 seconds because the system was at the anti-resonance state and the value of RMS was small. After the system was set into the resonance at  $t = 6.7$  second, the value of RMS was increased significantly. It took 0.512 second for the control system to react and the current changed. Then the response was reduced gradually. At  $t = 16.7$  second it took 0.512 second for the control system to respond to the frequency change. It is interesting to note that unlike the previous two cases, the current was led to a positive value after  $t = 16.7$  second. Although the EMVA was not tuned to achieve the anti-resonance according to the tuning condition, the stiffness of the EMVA was such that the system was tuned away from the resonance and vibration was suppressed.

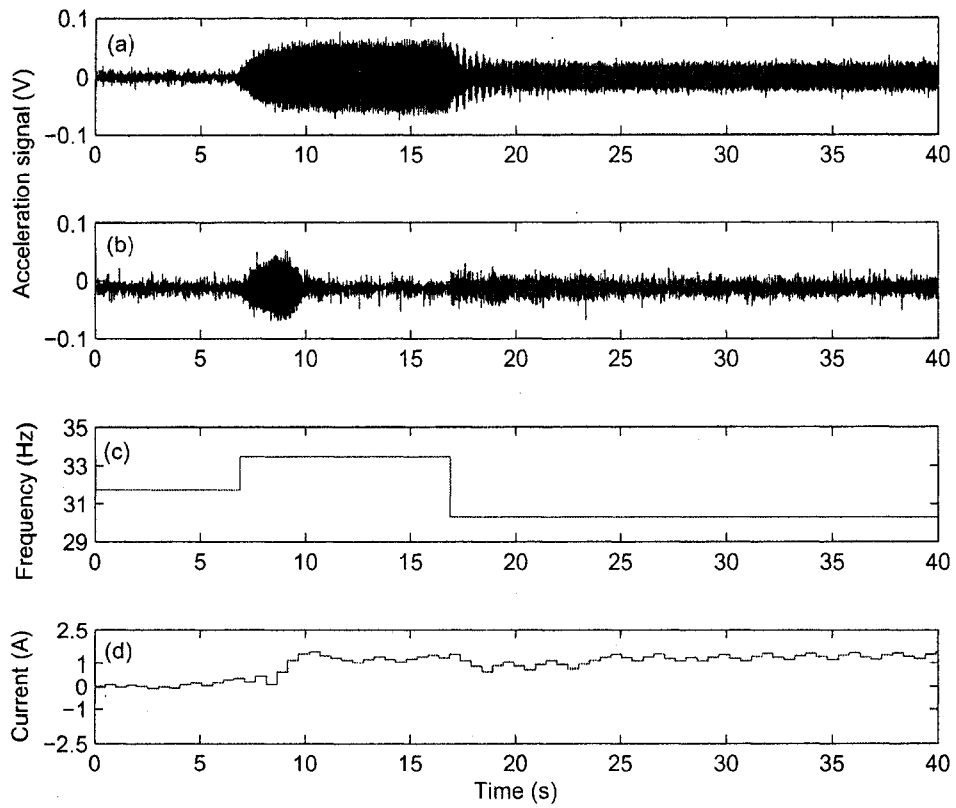


Figure 4.28 Experimental results using the RMS-based method when the absorber was manually preset at  $f_{a3} = 29.256$  Hz: (a) response of mass  $m_1$  without control, (b) response of mass  $m_1$  with control, (c) the excitation frequency, (d) the EMVA current.

## Chapter 5

# Conclusions and Future Work

### 5.1 Conclusions

The main object of this thesis was to apply the electromagnetic vibration absorber (EMVA) as a tunable vibration absorber in non-collocated vibration of a 3-DOF structure. The theoretic study on electromagnetism of the EMVA was reviewed. A commercial package Comsol Multiphysics was used to simulate similar models. It was found that Comsol models correctly represented the magnetic flux densities of electromagnetic coil by multiplying a factor of 1.76, the magnetic flux density of the permanent magnet (PM), and the forces on the PM caused by the core as the PM in the gap of the electromagnetic core. By utilizing a simplified model, the magnetic forces on the PM under different currents was obtained. A coupling model, which coupled the structural mechanics of the beam with electromagnetic physics of the coil and the PM, was built to simulate the force and displacement of the PM in different magnetizations. The results of the analytic and Comsol methods agreed in general. It was shown that Comsol Multiphysics was a useful software for solving problems related to electromagnetism, force and multiphysics. Multiphysics functionality of Comsol offered a great potential in dealing with the characterization of the mechatronics devices such as the EMVA.

A 3-DOF system was used to implement the non-collocated vibration control. By analyzing the frequency response, it was found that in most cases the vibration of a non-collocated mass could be thoroughly attenuated through adjusting the stiffness of the absorber such that one of the natural frequencies of the subsystem was equal to the excitation frequency if there was no damping between the absorber and the primary system.

Three auto-tuning methods had been developed. The first method, FFT-based method, was based on the frequency measured through the response. The second method, FFT-based plus fine tuning, added a fine controller which modifies the current determined from the coarse controller. The third method, RMS-based method, used the root-mean-



square value of the response. The first and second methods controlled the vibration of the system by adjusting the current of the EMVA based on the analytic study of the system. In case the physical conditions of the model or the EMVA changed, the first method could not correct the differences. The second method showed a better result than the first method if physical conditions of the system changed. The third method controlled the system in a slower speed and based on the precondition that the amplitude of the objective mass in the changing range of the frequency spectrum was unimodal. If the precondition did not exist, the method did not work effectively.

## **5.2 Future Work**

The work undertaken is the study of the EMVA and the non-collocated control. To apply the EMVA in a wider range of bandwidth, its structure may need to be modified such that a manual adjusting is easier and the adjusting range is larger enough to be used in suppressing the first natural frequency of the primary system. Study on the new EMVA is required such that it is more efficient. This can be facilitated with the help of Comsol Multiphysics, especially for complicated structures and multi-physical conditions. Applying Comsol Multiphysics in the study of a whole system is also one of the potential tasks.

## Reference

- [1] M. Setareh, Floor vibration control using semi-active tuned mass dampers, *Canadian Journal of Civil Engineering*, 29 (2002), 76-84.
- [2] K. Williams, G. Chui, and R. Bernhard, Geometric design of adaptive tuned vibration absorbers, *Proceedings of Inter-noise 99*, 901-906, Fort Landerdale, Florida, USA, 1999.
- [3] J. Q. Sun, M. R. Jolly, and M. A. Norris, Passive, adaptive and active tuned vibration absorbers- a survey, *Journal of Mechanical Design*, 117 (1995), 234-242.
- [4] J. P. Den Hartog, *Mechanics of Vibration*, 4th edition, McEraw-Hill, 1956.
- [5] N. K. Harris, E.J. Obrien, and A. González, Reduction of bridge dynamic amplification through adjustment of vehicle suspension damping, *Journal of Sound and Vibration*, 302 (2007), 471-485.
- [6] N. D. Sims, R. Stanway, D. J. Peel, W. A. Bullough and A. R. Johnson, Controllable viscous damping: an experimental study of an electrorheological long-stroke damper under proportional feedback control, *Smart Material Structure*, 8 (1999), 601-615.
- [7] L. Zuo and S.A. Nayfeh, Minimax optimization of multi-degree-of-freedom tuned mass dampers, *Journal of Sound and Vibration*, 272 (2004), 893-908.
- [8] J. C. Chang and T. T. Soong, Structural control using active tuned mass dampers, *Journal of the Engineering Mechanical Division*, 106 (1980), 1091-1098.
- [9] M. R. Jolly and J. Q. Sun, Passive Tuned vibration absorbers for sound radiation attenuation from panels, *Society of Photo-optical Instrumentation Engineers*, 2193 (194-201), 1994.
- [10] B. Breukelman, Good vibration, *Civil Engineering Magazine*, 12 (2001), American Society of Civil Engineering.
- [11] P. Dallard, A. J. Fitzpatrick, A. Flint, S. Le Bourva, A. Low, R. M. Ridsdill Smith, and M. Willford, The London millennium footbridge, *The Structural Engineer*, 79 (2001), 17-33.

- [12] Y. Hu, and A. Ng, Active robust vibration control of flexible structures, *Journal of Sound and Vibration*, 288 (2005) 43–56.
- [13] E. Lefevre, A. Badel, L. Petit, C. Richard and D. Guyomar, Semi-passive piezoelectric structural damping by synchronized switching on voltage sources, *Journal of Intelligent Material Systems and Structures*, 17 (2006), 653-660.
- [14] K. Nagaya, A. Kurusu, S. Ikai and Y. Shitani, Vibration control of a structure by using a tunable absorber and an optimal vibration absorber under auto-tuning control, *Journal of Sound and Vibration*, 228 (1999), 773-792.
- [15] K. Liu, L. Liao, and J. Liu, Comparison of two auto-tuning methods for a variable stiffness vibration absorber, *The Transactions of Canadian Society for Mechanical Engineering*, 29 (2005) 81-96.
- [16] C. L. Giliomee and P.S. Els, Semi-active hydropneumatic spring and damper system, *Journal of Terramechanics*, 35 (1998), 109-117.
- [17] J. N. Yang and A. K. Agrawal, Semi-active hybrid control systems for nonlinear buildings against near-field earthquakes, *Engineering Structures*, 24 (2002), 271–280.
- [18] J. Onoda, H. Ung Oh, and K. Minesugi, Semi-active vibration suppression of truss structures by electro-rheological fluid, *Acta Astronautica*, 40 (1997), 771-779.
- [19] D. Guo and H. Hu, Nonlinear stiffness of a magneto-rheological damper, *Nonlinear Dynamics*, 40 (2005), 241–249.
- [20] F. Casciati, G. Magonette, and F. Marazzi, *Technology of Semiactive Devices and Applications in Vibration Mitigation*, John Wiley & Sons Ltd, 2006.
- [21] P. Dupont, P. Kasturi, and A. Stokes, Semi-active control of friction dampers, *Journal of Sound and Vibration*, 202 (1997), 203-218.
- [22] N. Varadarajan and S. Nagarajaiah, Response control of building with variable stiffness tuned mass damper using empirical mode decomposition and Hilbert transform algorithm, *16th ASCE Engineering Mechanics Conference*, July 2003, Seattle.
- [23] M. A. Franchek, M. W. Ryan, and R. J. Bernhard, Adaptive passive vibration control, *Journal of Sound and Vibration*, 189 (1995), 565-585.

- [24] C. Buhr, M. A. Franchek, and R. J. Bernhard, Non-collocated adaptive-passive vibration control, *Journal of Sound and Vibration*, 206 (1997), 371-398.
- [25] J. Liu, *Design and Implementation of a Tunable Vibration Absorber and a Time-Delayed Vibration Absorber*, Master's thesis, Lakehead University, Thunder Bay, 2005.
- [26] J. Liu and K. Liu, A tunable electromagnetic vibration absorber characterization and application, *Journal of Sound and Vibration*, 295 (2006), 708-724.
- [27] W. Bong, Q. Liu, and F. Bauer, Classical and robust  $H_{\infty}$  control redesign for the Hubble Space Telescope, *Journal of Guidance, Control, and Dynamics*, 16 (1993), 1069-1077.
- [28] G. J. Balas and J. C. Doyle, Control of lightly damped, flexible modes in the controller crossover region, *Journal of Guidance, Control, and Dynamics* 17 (1994), 370-377.
- [29] B. Yang and C. D. Mote Jr., On time delay in noncollocated control of flexible mechanical systems, *Transaction of the American Society of Mechanical Engineers, Journal of Dynamic Systems, Measurement, and Control*, 114 (1992), 409-415.
- [30] T. W. Long, E. L. Hanzevack, and S. Caggiano, Noncollocated vibration control using neural networks. *IEEE International Symposium on Intelligent Control*, Monterey, CA, USA, 1995, 9-14.
- [31] R. S. Smith, C. Chu, and J. L. Fanson, The Design of  $H_{\infty}$  controllers for an experimental non-collocated flexible structure problem, *IEEE Transactions on Control Systems Technology*, 2 (2) (1994), 101-109.
- [32] D. J. Craik, *Magnetism: Principles and Applications*, Wiley, Chichester, New York, 1995.
- [33] <http://hyperphysics.phy-astr.gsu.edu/hbase/tables/magprop.html#c2>.
- [34] K. Liu, *Course Note, Computational Methods in Mechanical Engineering (Engi0579) - Part 3. Introduction to Optimization Design*, Lakehead University, August 2006.
- [35] M. H. Wright, *Optimization Methods for Base Station Placement in wireless Applications, Vehicular Technology Conference*, Ottawa, Ont., Canada, 48th IEEE, 1998.

- [36] J. Liu and K. Liu, Several Design Issues on the Tunable Electromagnetic Vibration Absorber, *the Transactions of the CSME*, 29 (2005), 655-668.

## Appendix A

### Determination of $\omega_A$ , $\omega_B$ , $\omega_C$ and $\omega_D$ in Equation (3.12)

Consider Equation (3.8) in Chapter 3

$$1 + k_a \frac{(m_2 m_a + m_2 m_3)s^4 + (k_3 m_3 + k_3 m_a + k_2 m_a + m_2 k_3 + k_2 m_3)s^2 + k_2 k_3}{m_a s^2 [m_2 m_3 s^4 + (k_3 m_3 + m_2 k_3 + k_2 m_3)s^2 + k_2 k_3]} = 0 \quad (\text{A-1})$$

Let

$$a = m_2 m_a + m_2 m_3$$

$$b = k_3 m_3 + k_3 m_a + k_2 m_a + m_2 k_3 + k_2 m_3$$

$$B = k_3 m_3 + m_2 k_3 + k_2 m_3$$

Equation (A-1) becomes

$$1 + k_a \frac{as^4 + bs^2 + k_2 k_3}{m_a s^2 [m_2 m_3 s^4 + Bs^2 + k_2 k_3]} = 0 \quad (\text{A-2})$$

Equation (A-1) can also be written in the factored form

$$1 + k_a \frac{a(s^2 + \omega_A^2)(s^2 + \omega_C^2)}{m_a (m_2 m_3) s^2 (s^2 + \omega_B^2)(s^2 + \omega_D^2)} = 0 \quad (\text{A-3})$$

When  $k_a = 0$ , for equation (A-2) the following equation exists

$$m_a m_2 m_3 s^6 + m_a B s^2 + m_a k_2 k_3 = 0 \quad (\text{A-4})$$

And for equation (A-3) the following exists

$$m_a m_2 m_3 (s^2 + \omega_B^2)(s^2 + \omega_D^2) = 0$$

or

$$m_a m_2 m_3 s^6 + m_a m_2 m_3 (\omega_B^2 + \omega_D^2) s^4 + m_a m_2 m_3 \omega_B^2 \omega_D^2 = 0 \quad (\text{A-5})$$

As equation (A-4) equals equation (A-5)

$$m_a B = m_a m_2 m_3 (\omega_B^2 + \omega_D^2) \quad (\text{A-6})$$

$$m_a k_2 k_3 = m_a m_2 m_3 \omega_B^2 \omega_D^2 \quad (\text{A-7})$$

From (A-6) and (A-7), the following results are obtained

$$\omega_B = \sqrt{\frac{B \pm \sqrt{B^2 - 4m_2 m_3 k_2 k_3}}{2m_2 m_3}} \quad (\text{A-8})$$

$$\omega_D = \sqrt{\frac{2k_2 k_3}{B \pm \sqrt{B^2 - 4m_2 m_3 k_2 k_3}}} \quad (\text{A-9})$$

When  $k_a = \infty$ , for equation (A-2) the following equation exists

$$as^4 + bs^2 + k_2 k_3 = 0 \quad (\text{A-10})$$

And for equation (A-3) the following equation exists

$$a(s^2 + \omega_A^2)(s^2 + \omega_C^2) = 0$$

or

$$as^4 + a(\omega_A^2 + \omega_C^2)s^2 + a\omega_A^2\omega_C^2 = 0 \quad (\text{A-11})$$

As equation (A-10) equals equation (A-11)

$$a = a(\omega_A^2 + \omega_C^2) \quad (\text{A-12})$$

$$k_2k_3 = a\omega_A^2\omega_C^2 \quad (\text{A-13})$$

From (A-12) and (A-13), the following results are obtained

$$\omega_C = \sqrt{\frac{b \pm \sqrt{b^2 - 4ak_2k_3}}{2a}} \quad (\text{A-14})$$

$$\omega_A = \sqrt{\frac{2k_2k_3}{b \pm \sqrt{b^2 - 4ak_2k_3}}} \quad (\text{A-15})$$

As the following parameters are considered

$$m_1 = 2.73 \text{ kg}; m_2 = 2.048 \text{ kg}; m_3 = 2.635 \text{ kg}; m_a = 0.2515 \text{ kg}; k_1 = 17181 \text{ N/m};$$

$$k_2 = 35401 \text{ N/m}; k_3 = 20616 \text{ N/m}.$$

The following results are obtained

$$\omega_{A1} = 10.1361 \text{ Hz}; \omega_{A2} = 27.7671 \text{ Hz}; \omega_{B1} = 175.4495 \text{ Hz}; \omega_{B2} = 66.2831 \text{ Hz};$$

$$\omega_{C1} = 59.9199 \text{ Hz}; \omega_{C2} = 164.1465 \text{ Hz}; \omega_{D1} = 10.5493 \text{ Hz}; \omega_{D2} = 27.9236 \text{ Hz}.$$

It must be noted that  $\omega_A$ ,  $\omega_B$ ,  $\omega_C$  and  $\omega_D$  mentioned in Section 3.4 of Chapter 3 (Page 50-52) are now represented as  $\omega_{A1}$ ,  $\omega_{D1}$ ,  $\omega_{A2}$  and  $\omega_{D2}$ , respectively. Because only the



frequency under 40 Hz is considered, all other frequencies obtained by equation (A-8), (A-9), (A-14), (A-15) above 40 Hz were considered infinite.

## Appendix B

### Procedure to Build the Electromagnet Model

(Comsol 3.3a)

#### MODEL NAVIGATOR

Select **COMSOL Multiphysics**, select **3D> AC/DC Module>Statics> Magnetostatics** mode in the **Model Navigator**.

#### OPTIONS AND SETTINGS

In **Options> Constants**, enter the following names and expressions.

Name	Expression	Description
murFe	25	Relative permeability of steel
R	0.05	Radius of the torus center line
r	0.015	Medium radius of the electromagnetic coil

#### GEOMETRY MODELING

Building a hollow torus

1. In **Draw>Work Plane Setting>Plane**, click 'x-y, z:0'. Click **OK**.
2. Draw a circle with a diameter of 0.03 (A-semiaxes: 0.015; B-semiaxes: 0.015) with the center at (0.05, 0), the name is E1.
3. Draw a circle with a diameter of 0.025 (A-semiaxes: 0.0125; B-semiaxes: 0.0125) with the center at (0.05, 0), the name is E2.
4. Click the inner circle. Hold Ctrl key and click the outer circle.
5. Open **Draw> Create Composite Object**.
6. In **Set formula**, input 'E1-E2'. Click **OK**.
7. In **Draw> Revolve**, select **Revolution**. In **Revolution axis> Point on axis**: x=0, y=0; **Axis direction through> Second point**: x=0, y=1. Click **OK**.

Now a hollow torus is formed.

Building a solid block

Draw a circle with a diameter of 0.025 with the center at (0.05, 0), the name is E2.

In **Draw**> **Revolve**, select **Revolution**. In **Revolution axis**> **Point on axis**:  $x=0, y=0$ ;  
**Axis direction through**> **Second point**:  $x=0, y=1$ . Click **OK**.

Now a solid torus is formed.

Building a block

1. In **Draw**, select **Block**.
2. In '**Base**', select **center**.
3. In **Length**, select:  $X=0.043, Y=0.045, Z=0.05$ .
4. In **Axis base point**, select:  $x=0, y=0, z=0.05$ .

Now a block (BLK1) is formed.

Copying a block

1. Copy the block made above.
2. Paste the block. Choose the **displacement**:  $x=0, y=0, z=0$ .

Now another block (BLK2) is formed.

Forming the gap

1. Open **Draw** > **Create Composite object**.
2. In '**Set formula**', input 'REV1-BLK1'. Click **OK**.
3. In '**Set formula**', input 'REV2-BLK2'. Click **OK**.

Now the hollow torus (CO2) and the solid torus (CO1) are cut with a gap.

Creating a block for free space

1. In **Draw**, select **Block**.
2. In **Base**, select **center**.
3. In **Length**, select:  $X=0.2, Y=0.2, Z=0.2$ .
4. In **Axis base point**, select **center** and enter:  $x=0, y=0, z=0$ .

Now a block is formed (BLK1).

## PHYSICS SETTINGS FOR ELECTROMAGNETICS

Apply the Current

1. In **Physics**> **Subdomain Settings**.
2. Select  $B = \mu_0\mu_r H$  for all subdomains.

### *Subdomain Settings*

In the Subdomain Settings dialog box, enter the coefficients according to the table below.

SUBDOMAIN	1	2	3
$\mu_r$	1	1	murFe
$J^e$	0	$-J0*x*y/(r*\sqrt{x^2+z^2})$	0
	0	$J0*(\sqrt{x^2+z^2}-R)/r$	0
	0	$-J0*z*y/(r*\sqrt{x^2+z^2})$	0

### *Boundary Conditions*

Keep default boundary conditions according to the table below.

BOUNDARY	1-5, 42	ALL OTHER
Boundary condition	Magnetic insulation	Dim (keep default)

## MESH GENERATION

1. In **Mesh**> **Free Mesh Parameters**, select 'Extra coarse' in **Predefined mesh sizes**.
2. Click **OK**.

## COMPUTING THE SOLUTION

1. From the **Solver** menu open the **Solver Parameters** dialog box.
2. Go to the **Solver** list and select **Parametric**.
3. In the **Name of parameter** edit field, type J0.
4. In the **List of parameter values** edit field enter 581343\*1.76:581343\*1.76:  
2325372\*1.76.
5. In **Linear system solver** edit field, select **Direct (UMFPACK)**.

6. Go to the **Parametric** in the same dialog window, select **Linear** in **Predictor** edit field.
7. Go to the **Stationary** in the same dialog window, select **Automatic** in **Linearity** edit field.
8. Click **OK**.
9. Click the **Solve** button on the **Main** toolbar (**Solve**> **Solve Problem**).

#### Postprocessing

1. Go to **Options**> **Suppress**> **Suppress Boundaries**.
2. Select 1, 2, 3, 4, 5, and 42. Click.
3. Open **Postprocessing**> **Plot Parameters**> **General**, select **Boundary, Arrow**.
4. Open **Postprocessing**> **Plot Parameters**> **Arrow**, select **Total current density** in **Subdomain Data**. Still in **Arrow**, select **x points, y points** and **z points**, and enter **Number of points=30** the three directions. Click **Apply**. The arrow plot of current density is shown.
5. Open **Postprocessing**> **Cross-Section Plot Parameters**>**Line/Extrusion**. In **y-axis data**, in **Prdefined quantities**, select **Magnetic flux density, x component**. In **x-axis data**, select **x**. In **Cross-section line data**, input:  $x_0=-0.0185$ ,  $x_1=0.0185$ .  $y_0=0$ ,  $y_1=0$ ,  $z_0=0.05$ ,  $z_1=0.05$ .
6. Click **Apply**. The magnetic flux density along the centerline between C-gap is shown.

## Appendix C

### Part I. Procedure to build a coupling model (Comsol 3.3a)

This instruction shows the procedure of building the coupling model shown in Figure 2.30. The primary problem the model addresses is the 2-way coupling between the deformations and the magnetic field. It solves the magnetic equation in the air domain surrounding the model using the arbitrary Lagrangian-Eulerian (ALE) method to account for geometry changes associated with the deformation.

#### MODEL NAVIGATOR

1. In the **Model Navigator** select **2D** in the **Space dimension** list and then click **Multiphysics**.
2. From the list of application modes on the left side of the dialog box select **Structural Mechanics Module>Plane Stress** and then click **Add**.
3. From the list of application modes select **COMSOL Multiphysics>Deformed Mesh>Moving Mesh (ALE)** and then click **Add**.
4. In the **Multiphysics** list on the right side of the dialog box select **Frame (Ale)** then add **AC/DC Module> Quasi-Statics, Magnetic> Perpendicular Induction Currents, Vector Potential (emqa)** to that list.

#### OPTIONS AND SETTINGS

In **Options> Constants**, enter the following names and expressions.

Name	Expression	Value	Description
m <sub>pre</sub>	45000	45000	Magnetization of the upper and lower PMs
M <sub>pre</sub>	395800	395800	Magnetization of the middle PM

#### GEOMETRY MODELING

1. Draw the following rectangles:

Rectangle name	Width	Height	X	Y
R1(left beam)	0.1	0.0015	-0.124	-0.00075
R2(right beam)	0.1	0.0015	0.024	-0.00075
R3(middle PM)	0.048	0.038	-0.024	-0.019
R4(upper gap)	0.048	0.0025	-0.024	0.019
R5(lower gap)	0.048	0.0025	-0.024	-0.0215
R6	0.1	0.02075	-0.124	-0.0215
R7	0.1	0.02075	-0.124	0.00075
R8	0.1	0.02075	0.024	-0.0215
R9	0.1	0.02075	0.024	0.00075
R10 (lower PM)	0.048	0.04	-0.024	-0.0615
R11 (upper PM)	0.048	0.04	-0.024	0.0215
R12	0.1	0.04	-0.124	0.0215
R13	0.1	0.04	-0.124	-0.0615
R14	0.1	0.04	0.024	-0.0615
R15	0.1	0.04	0.024	0.0215
R16	0.248	0.12	-0.124	-0.1815
R17	0.248	0.12	-0.124	0.0615

2. Click the **Zoom Extents** button on the **Main** toolbar at the top of the graphical user interface.
3. Go to **Draw>Draw Objects>Point**. Draw a point PT17 at X=0 and Y=0. Point position can be adjusted by going to **Draw>Object Properties**, selecting 1 in **Point** edit field. Enter 0 for x and y.

## PHYSICS SETTINGS FOR ELECTROMAGNETICS

### *Subdomain Settings*

1. Go to the **Multiphysics** menu and make sure that **Perpendicular Induction Currents, Vector Potential (emqa)** is selected.

2. Open the **Physics>Subdomain Settings** dialog box and select all Subdomains except the three PMs (Subdomains 8, 10, 12). The default settings ( $\mu_r = 1$ ) corresponds to air, so keep them. While still in that dialog box, select Subdomain 8. In constitutive relation, select  $B = \mu_0 H + \mu_0 M$ . In the magnetization edit field **M**, input 0 and Mpre for **X and Y magnetization**, respectively. In **Forces**, input Fes in **Name**. Return to the dialog box in **Physics**, select **Subdomain 10, 12**. In constitutive relation, select  $B = \mu_0 H + \mu_0 M$ . In the magnetization edit field **M**, input 0 and mpre for **X and Y magnetization**, respectively.
3. Click **OK**.

#### *Boundary Conditions*

1. From the **Physics** menu open the **Boundary Settings** dialog box.
2. Keep **Interior Boundaries** clear. Keep default conditions (**Boundaries 1, 2, 3, 5, 7, 9, 11, 13, 15, 42-48: Magnetic insulation**. Other Boundaries: **Continuity**).
3. Click **OK**.

### **PHYSICS SETTINGS FOR MOVING MESH**

#### *Subdomain Settings*

1. From the **Multiphysics** menu select **Moving Mesh (ale)**.
2. In the **Subdomain Settings** dialog box select the Subdomains for air (except Subdomains 4, 8, 10, 12, 15). Keep the default **Free displacement** setting.
3. While still in that dialog box select Subdomains 8, 12 (the upper and lower PMs). Select **Mesh> No displacement**. Select Subdomains 4, 10, 15 (the middle PM, right and left beams). Select **Mesh> Physics induced displacement**. For the displacement variables, **dx** and **dy**, enter u and v respectively. There are the displacements from the **Plane Stress application mode**.
4. Click **OK**.

#### *Boundary Conditions*



1. From the **Physics** menu open the **Boundary Settings** dialog box.
2. In the **Boundary Settings** dialog box for the mesh displacements, **dx** and **dy**, enter the following values for outer settings:

<b>SETTINGS</b>	<b>Subdomains 1, 2, 3, 5, 9, 11, 13, 15-17, 19, 26-29, 39, 42-44, 46-48</b>	<b>Subdomains 8, 10, 20, 21, 23, 25, 33, 35, 37</b>	<b>ALL OTHER</b>
Dx	0	u	Do not assign
Dy	0	v	Do not assign

3. Click **OK**.

#### *Properties*

1. From **Physics> Properties> Application Mode Properties** dialog box, select **Winslow** in **Smooth method**.
2. Click **OK** to close the dialog box.

### **PHYSICS SETTINGS FOR PLANE STRESS**

#### *Application Mode Properties*

1. From **Multiphysics** menu choose **Plane Stress (smps)**.
2. From the **physics** menu open the **Properties** dialog box.
3. Click the **Application Mode Properties** button, go to the **Large deformation** list, select **On**; then click **OK**.
4. Click **OK** to close the dialog box.

The large-deformation option ensures that the solver uses a nonlinear stress-strain relationship to calculate the results in the **Plane Strain application mode**.

#### *Subdomain Settings*

1. In the **Subdomain Settings** dialog box select **Subdomain> Material** enter the following settings:

Name	Subdomains 4, 15	Subdomains 10
E	70e9	70 e11
$\nu$	0.33	0.33
$\alpha$	23e-6	23e-6
$\rho$	2700	2700
Thickness	1	1

2. While still in the dialog box select **Subdomains 4, 10, 15** and click **Active** in these **Subdomains**. Select all other **Subdomains** and clear **Active in this domain** to inactive these domains.
3. Click **OK**.

#### *Boundary Conditions*

1. From the **Physics** menu select **Boundary Settings**. In the resulting dialog box verify that the **Interior boundaries** check box is cleared.
2. Click the **Constraint** tab, then select **Boundaries 7, 45**. From the **Constraint condition** list select **Fixed**. For all other **Boundaries**, select **Free**.
3. In the same window, click the **Load** tab, then select **Boundaries 21 and 25**. In the **Value/expression** edit field for **Fx** enter 0 and for **Fy** enter  $Fes\_nTy\_emqa$ . For all other **Boundaries**, select default  $Fx=0$  and  $Fy=0$ .
4. Click **OK** to accept the boundary conditions.

#### *Point Conditions*

Apply a variable force  $Fy$  on the center point of the middle PM in y-direction.

1. Click the **Physics>Point Settings** tab. Select **Point 17**. Click **Load**, and enter 0 for **Fx** and  $Fy$  for **Fy**.
2. Click **OK**.

### **MESH GENERATION**

1. Select **Mesh> Free Mesh Parameters**, select **Fine** in **Predefined mesh sizes**.

2. Click **OK**.
3. Click **Initialize Mesh** to complete mesh.

### **COMPUTING THE SOLUTION**

1. From the **Solver** menu open the **Solver Parameters** dialog box.
2. Go to the **Solver** list and select **Parametric**.
3. In the **Name of parameter** edit field, enter **Fy**.
4. In the **List of parameter values** edit field enter **-2100:100:2100**.
5. In **Linear system solver** edit field, select **Direct (UMFPACK)** in **Linear system solver**.
6. Go to the **Parametric** edit field in the same dialog window, select **Linear** in **Predictor** edit field.
7. Go to the **Stationary** in the same dialog window, select **Automatic** in **Linearity** edit field. And click **Highly nonlinear problem**.
8. Click **OK**.
9. Click the **Solve** button on the **Main** toolbar (**Solve> Solve Problem**).

### **POSTPROCESSING AND VISUALIZATION**

To view magnetic field and displacement of the middle PM and beam, follow these instructions:

1. From the **Postprocessing** menu open the **Plot Parameters** dialog box.
2. On the **General** page select **Boundary** and **Arrow**. Make sure the check boxes for all other types are cleared.
3. Go to the **Boundary**. Enter 1 in **Expression**. Go to the **Arrow**, select **Magnetic flux density** in **Subdomain Data> Predefined quantities**. Click **OK**.
4. Go to **Postprocessing> Domain Plot Parameters> Line/Extrusion**. Select **y-displacement** in **y-axis data>Predefined quantities**. Select 8 in **Boundary selection**.
5. Click **Apply**. The deformation of the left beam is shown.

## Part II. Procedure to build a simple coupling model

This instruction shows the procedure of building a simple coupling model shown in Fig A.1. The model is the same as Figure 2.30 except it has only the same boundary rectangle, three PMs and two beams while moving away other rectangles. It solves the magnetic equation in the air domain surrounding the model using the arbitrary Lagrangian-Eulerian (ALE) method to account for geometry changes associated with the deformation.

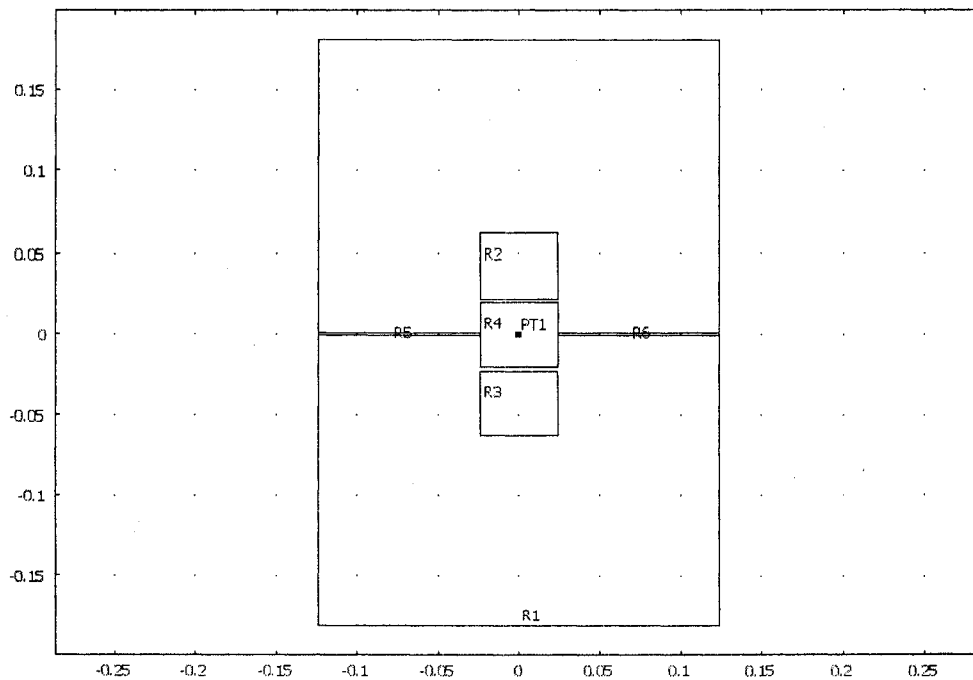


Figure A.1 Simple coupling model

### MODEL NAVIGATOR

1. In the **Model Navigator** select **2D** in the **Space dimension** list and then click **Multiphysics**.
2. From the list of application modes on the left side of the dialog box select **Structural Mechanics Module>Plane Stress** and then click **Add**.
3. From the list of application modes select **COMSOL Multiphysics>Deformed Mesh>Moving Mesh (ALE)** and then click **Add**.

- In the **Multiphysics** list on the right side of the dialog box select **Frame (Ale)** then add **AC/DC Module> Quasi-Statics, Magnetic> Perpendicular Induction Currents, Vector Potential (emqa)** to that list.

### OPTIONS AND SETTINGS

In **Options> Constants**, enter the following names and expressions.

Name	Expression	Value	Description
mpre	45000	45000	Magnetization of the upper and lower PMs
Mpre	395800	395800	Magnetization of the middle PM

### GEOMETRY MODELING

- Draw the following rectangles:

Rectangle name	Width	Height	X	Y
R1(boundary rectangle)	0.248	0.363	-0.124	-0.1815
R2(upper PM)	0.048	0.04	-0.024	0.0225
R3 (lower PM)	0.048	0.04	-0.024	-0.0625
R4(middle PM)	0.048	0.04	-0.024	-0.02
R5(left beam)	0.1	0.0015	-0.124	-0.00075
R6(right beam)	0.1	0.0015	0.024	-0.00075

- Click the **Zoom Extents** button on the **Main** toolbar at the top of the graphical user interface.
- Go to **Draw>Draw Objects>Point**. Draw a point PT17 at X=0 and Y=0. Point position can be adjusted by going to **Draw>Object Properties**, selecting 1 in **Point** edit field. Enter 0 for x and y.

### PHYSICS SETTINGS FOR ELECTROMAGNETICS

### *Subdomain Settings*

1. Go to the **Multiphysics** menu and make sure that **Perpendicular Induction Currents, Vector Potential (emqa)** is selected.
2. Open the **Physics>Subdomain Settings** dialog box and select all Subdomains except the three PMs (Subdomains 4, 5, 6). The default settings ( $\mu_r = 1$ ) corresponds to air, so keep them. While still in that dialog box, select Subdomain 5. In constitutive relation, select  $B = \mu_0 H + \mu_0 M$ . In the magnetization edit field **M**, enter 0 and Mpre for **X and Y magnetization**, respectively. In **Forces**, input Fes in Name. Return to the dialog box in **Physics**, select **Subdomain 4, 6**. In constitutive relation, select  $B = \mu_0 H + \mu_0 M$ . In the magnetization edit field **M**, input 0 and mpre for **X and Y magnetization**, respectively.
3. Click **OK**.

### *Boundary Conditions*

1. From the **Physics** menu open the **Boundary Settings** dialog box.
2. Keep **Interior Boundaries** clear. Keep default conditions (**Boundaries 1, 2, 3, 5, 7, 26-28: Magnetic insulation**. Other Boundaries: **Continuity**).
3. Click **OK**.

## **PHYSICS SETTINGS FOR MOVING MESH**

### *Subdomain Settings*

1. From the **Multiphysics** menu select **Moving Mesh (ale)**.
2. In the **Subdomain Settings** dialog box select the Subdomain 1 for air. Keep the default **Free displacement** setting.
3. While still in that dialog box select Subdomains 4, 6 (the upper and lower PMs). Select **Mesh> No displacement**. Select Subdomains 2, 5, 7 (the middle PM, right and left beams). Select **Mesh> Physics induced displacement**. For the displacement variables, **dx** and **dy**, enter u and v respectively. There are the displacements from the **Plane Stress application mode**.

4. Click **OK**.

*Boundary Conditions*

1. From the **Physics** menu open the **Boundary Settings** dialog box.
2. In the **Boundary Settings** dialog box for the mesh displacements, **dx** and **dy**, enter the following values for outer settings:

<b>SETTINGS</b>	<b>Subdomains 1, 2, 5, 7-10, 16-19, 25-26, 28</b>	<b>Subdomains 4, 6, 11,12, 14, 15, 20, 22, 23, 24</b>	<b>ALL OTHER</b>
dx	0	u	Do not assign
dy	0	v	Do not assign

3. Click **OK**.

*Properties*

1. From **Physics> Properties> Application Mode Properties** dialog box, select **Winslow** in **Smooth method**.
2. Click **OK** to close the dialog box.

**PHYSICS SETTINGS FOR PLANE STRESS**

*Application Mode Properties*

1. From **Multiphysics** menu choose **Plane Stress (smps)**.
2. From the **physics** menu open the **Properties** dialog box.
3. Click the **Application Mode Properties** button, go to the **Large deformation** list, select **On**; then click **OK**.
4. Click **OK** to close the dialog box.

The large-deformation option ensures that the solver uses a nonlinear stress-strain relationship to calculate the results in the **Plane Strain application mode**.

### *Subdomain Settings*

1. In the **Subdomain Settings** dialog box select **Subdomain> Material** enter the following settings:

<b>Name</b>	<b>Subdomains 2, 7</b>	<b>Subdomains 5</b>
E	70e9	70 e11
$\nu$	0.33	0.33
$\alpha$	23e-6	23e-6
$\rho$	2700	2700
Thickness	1	1

2. While still in the dialog box select **Subdomains 2, 5, 7** and click **Active** in these **Subdomains**. Select all other **Subdomains** and clear **Active in this domain** to inactive these domains.
3. Click **OK**.

### *Boundary Conditions*

1. From the **Physics** menu select **Boundary Settings**. In the resulting dialog box verify that the **Interior boundaries** check box is cleared.
2. Click the **Constraint** tab, then select **Boundaries 3, 27**. From the **Constraint condition** list select **Fixed**. For all other **Boundaries**, select **Free**.
3. In the same window, click the **Load** tab, then select **Boundaries 12 and 15**. In the **Value/expression** edit field for **Fx** enter 0 and for **Fy** enter  $F_{es\_nTy\_emqa}$ . For all other **Boundaries**, select default  $F_x=0$  and  $F_y=0$ .
4. Click **OK** to accept the boundary conditions.

### *Point Conditions*

Apply a variable force  $F_y$  on the center point of the middle PM in y-direction.

1. Click the **Physics>Point Settings** tab. Select **Point 13 (PT1)**. Click **Load**, and enter 0 for **Fx** and  $F_y$  for **Fy**.
2. Click **OK**.



## MESH GENERATION

1. Select **Mesh> Free Mesh Parameters**, select **Fine** in **Predefined mesh sizes**.
2. Click **OK**.
3. Click **Initialize Mesh** to complete mesh.

## COMPUTING THE SOLUTION

1. From the **Solver** menu open the **Solver Parameters** dialog box.
2. Go to the **Solver** list and select **Parametric**.
3. In the **Name of parameter** edit field, type **Fy**.
4. In the **List of parameter values** edit field enter **-2100:100:2100**.
5. In **Linear system solver** edit field, select **Direct (UMFPACK)** in **Linear system solver**.
6. Go to the **Parametric** edit field in the same dialog window, select **Linear** in **Predictor** edit field.
7. Go to the **Stationary** in the same dialog window, select **Automatic** in **Linearity** edit field. And click **Highly nonlinear problem**.
8. Click **OK**.
9. Click the **Solve** button on the **Main** toolbar (**Solve> Solve Problem**).

## POSTPROCESSING AND VISUALIZATION

To view magnetic field and displacement of the middle PM and beam, follow these instructions:

1. From the **Postprocessing** menu open the **Plot Parameters** dialog box.
2. On the **General** page select **Boundary** and **Arrow**. Make sure the check boxes for all other types are cleared.
3. Go to the **Boundary**. Enter 1 in **Expression**. Go to the **Arrow**, select **Magnetic flux density** in **Subdomain Data> Predefined quantities**. Click **OK**.
4. Go to **Postporcessing> Domain Plot Parameters> Line/Extrusion**. Select **y-displacement** in **y-axis data>Predefined quantities**. Select 6 in **Boundary selection**.
5. Click **Apply**. The deformation of the left beam is shown.

**Appendix D**  
**Development of a Control Model using dSPACE ControlDesk**  
**(ControlDesk Developer Version 2.1.1)**

**Part I. Procedures**

1. Turn on Computer.
2. Open Matlab first, and then open Simulink.
3. Open the simulink model built.
4. Open DSpace Controldesk to get into the ControlDesk environment.
5. Set up the new ControlDesk Layout file: File > New > Layout, then save it.
6. Go back to Simulink. Build Simulink model: Tools > Real-Time Workshop > Build Model.
7. Back to ControlDesk. Set up the connection between ControlDesk and Simulink: **Data Acquisition** (on the right of the screen) > click **CaptureSettings** > click any point on the **Layout** window, hold the pointer to draw a small window for the instruments to be embedded in > double click this small window, a window **dSPACE Capture Settings Control Properties** comes out. In this window, select **Capture** and click down arrow “▼” to select the name of the corresponding Simulink Model (now the connection between the Simulink model and ControlDesk Layout file has been established).
8. Switch to **Edit Mode** > **Stop** (small red box on the toolbar). Double click the window **dSPACE Capture Settings Control Properties** mentioned in “7” . The window comes out again. In **Capture**, change the time **Length** of the data acquisition. **Auto Repeat** means the old data obtained in the previous time **Length** will be overwritten with another new acquisition. **Downsampling** means the sampling time, for example, **Downsampling** 1 means sampling time = 0.001 s, 3 means sampling time = 0.003 s. Increasing **Downsampling** means recording the data using a slower sampling time.

If more data (such as selecting more **Plotter** in **Data-Acquisition** or increase the **Length** of time) are selected, **Downsampling** will be increased due to the limited memory of the computer. All data shown on **Plotters** are collected.

To save data, in the window **dSPACE Capture Settings Control Properties**, select **Acquisition**. Select **Autosave** and assign a file name with a root in **Acquisition**. If **OK** or **Apply** at the bottom of the window is clicked, a file name is formed in the assigned place. But now there are no data in the file. dSPACE has to be run to form them.

9. Now it is the time to add other instruments in the Layout to control the corresponding elements in Simulink Model. It is known that ControlDesk provides an environment to visually and online control the process in which the Simulink Model is executed. So each element in the Simulink Model can be controlled or manipulated through the corresponding visualized instruments in the ControlDesk file. These instruments can be found on **Visual Instruments** (on the right of the screen). Some of the frequently used ones are **Display**, **NumericInput**, **OnOffButton**, and **Slider**. Some other instruments can also be found from **Data Acquisition** (on the right of the screen) such as **CaptureSettings** and **Plotter**.
10. Connect a virtual instrument to a variable of the Simulink model. For example, if the output of ADC1gain (ADC1gain is an operator used in the Simulink model) is to be plotted. Check the small tab at the bottom of the Layout Screen, the Simulink Model file can be seen. It may need to bring the window up to reduce the size of Layout window. Model file is **Model Root** which contains all Simulink variables. From this list, find ADC1gain and select it. Now on the right screen, **Gain** and **Out1** can be seen. Drag **Out1** to **Plotter** (already placed on Layout window). Notice that, after **Out1** at **Plotter** is released, the red frame around **Plotter** disappears, which means that **Plotter** is associated with variable Out1.

It must be careful that the operation can only be completed when **Tool Window** is activated. If there is no **Tool Window** on ControlDesk, click “**Activate Tool Window** from main menu > **View > Activate Tool Window** to activate the **Tool Window**. At the bottom of the **Tool Window**, there are four choices: **Log Viewer**, **File Selector**, **Interpreter** and **Model Root**. **Model Root** is in the form such as

- 'C:\matlab\work\testsample". To plot an output, click C:\matlab\work\testsample before select the output.
11. Another example, to use **Slider** to control the gain of **ADC1gain**. Click **Slider** under **Virtual Instrument** and draw a box on **Layout** window. Then, drag **Gain** under **Variable** and release it on **Slider**.
  12. Do the same to any variable to control or to output in the Simulink model.
  13. Once the connections for all the elements have been established, run the program: run (green triangle) > **Animation Mode**.
  14. After the program runs a period, stop it. The data are saved in the root directory assigned in "8" with the same name. Then load the data file under Matlab environment using command: load the filename. Note the data file is in Matlab mat format. When the data file is loaded, it is a Matlab structure. The size of the structure is decided by the number of **Plotter**, the **Length** of time and **Downsampling** number. Consult Matlab manual for the instruction of how to access Matlab structures.

## Part II. Sample of dSPACE operation

1. Turn on Computer.
2. First open Matlab, then open Simulink.
3. Open the simulink model: C:\Matlab\ work\November1\nov.mdl.
4. Open DSpace Controldesk to get into the ControlDesk environment.
5. Go back to Simulink model opened in step 3. Build Simulink model: Tools > Real-Time Workshop > Build Model.
6. Go to ControlDesk. Open the dSPACE model from C:\Matlab\ work\ November1\Nov1test.lay.
7. In this window **dSPACE Capture Settings Control Properties**, select **Capture** and click down arrow "▼" to select the name of the corresponding Simulink Model (now the connection between the Simulink model and ControlDesk Layout file has been established. If there is no connection, choose 'DPS\_nov\_position capture').  
In **Interval**, **Length**, change to 5 (second).

To save data, in the window **dSPACE Capture Settings Control Properties**, select **Acquisition**. Select **Autosave** and assign a file name 'datasample' in a directory. Click **OK** or **Apply** at the bottom of the window, a file name is formed in the directory 'C:\Matlab\ work\ November1'. But now there are no data in the file. The user has to run dSPACE to form them.

8. Click the start button in dSPACE. Run it for more than 5 seconds. Then stop. Now the data are saved.

Postprocessing the data:

Typical operation example for data saving and data processing:

- a. Following "8": To save data, from **Acquisition** select **Autosave** and assign **C:\matlab\work\datasample**. The file name is **datasample** and the root directory is **C:\matlab\work**. Click **OK** or **Apply** at the bottom of the window, a file name "datasample" is formed in **C:\matlab\work**.
- b. Run the program for a full period of time, the data are saved. Load the file under Matlab environment using command:

Load **datasample**.

```
datafile=datasample
```

```
data1=double(datafile.Y(:,1).Data);
```

```
data2=double(datafile.Y(:,2).Data);
```

```
figure(1)
```

```
plot(data1)
```

```
figure (2)
```

```
plot(data2)
```

Note the data file structure is decided by the number of the plotters. The sample uses only two plotters.